5-2011

Modeling gamma-ray bursts

Amanda Maxham
University of Nevada, Las Vegas

MODELING GAMMA-RAY BURSTS

by

Amanda Maxham

Masters of Science
University of Illinois, Urbana-Champaign
2003

Bachelor of Science
University of Wisconsin, Madison
2001

A thesis submitted in partial fulfillment
of the requirements for the

Doctor of Philosophy Degree in Physics
Department of Physics and Astronomy
College of Sciences

Graduate College
University of Nevada, Las Vegas
May 2011

UNIVERSITY OF NEVADA LAS VEGAS

THE GRADUATE COLLEGE

We recommend the dissertation prepared under our supervision by

Amanda Maxham

entitled

Modeling Gamma-Ray Bursts

be accepted in partial fulfillment of the requirements for the degree of

Doctor of Philosophy in Physics

Bing Zhang, Committee Chair

Stephen Lepp, Committee Member

Tao Pang, Committee Member

Daniel Proga, Committee Member

Matthew Lachniet, Graduate Faculty Representative

Ronald Smith, Ph. D., Vice President for Research and Graduate Studies
and Dean of the Graduate College

May 2011

ABSTRACT

MODELING GAMMA-RAY BURSTS

by

Amanda Maxham

Dr. Bing Zhang, Examination Committee Chair
Professor of Physics
University of Nevada, Las Vegas

Discovered serendipitously in the late 1960s, gamma-ray bursts (GRBs) are huge explosions of energy that happen at cosmological distances. They provide a grand physical playground to those who study them, from relativistic effects such as beaming, jets, shocks and blastwaves to radiation mechanisms such as synchrotron radiation to galatic and stellar populations and history. Through the Swift and Fermi space telescopes dedicated to observing GRBs over a wide range of energies(from keV to GeV), combined with accurate pinpointing that allows ground based follow-up observations in the optical, infrared and radio, a rich tapestry of GRB observations has emerged. The general picture is of a mysterious central engine (CE) probably composed of a black hole or neutron star that ejects relativistic shells of matter into intense magnetic fields. These shells collide and combine, releasing energy in "internal shocks" accounting for the prompt emission and flaring we see and the "external shock" or plowing of the first blastwave into the ambient surrounding medium has well-explained the afterglow radiation.

We have developed a shell model code to address the question of how X-ray flares are produced within the framework of the internal shock model. The shell model creates randomized GRB explosions from a central engine with multiple shells and follows those shells as they collide, merge and spread, producing prompt emission and X-ray flares. We have also included a blastwave model,

which can constrain X-ray flares and explain the origin of high energy (GeV) emission seen by the Fermi telescope.

Evidence suggests that gamma-ray prompt emission and X-ray flares share a common origin and that at least some flares can only be explained by long-lasting central engine activity. We pay special attention to the time history of central engine activity, internal shocks, and observed flares. We calculate the gamma-ray (Swift/BAT band) and X-ray (Swift/XRT band) lightcurves for arbitrary central engine activity and compare the model results with the observational data. We show that the observed X-ray flare phenomenology can be explained within the internal shock model. The number, width and occurring time of flares are then used to diagnose the central engine activity, putting constraints on the energy, ejection time, width and number of ejected shells. We find that the observed X-ray flare time history generally reflects the time history of the central engine, which reactivates multiple times after the prompt emission phase with progressively reduced energy.

This shell model code can be used to constrain broadband observations of GRB 090926A, which showed two flares in both the Swift UVOT and XRT bands. Using the prompt emission fluence to constrain the total energy contained in the blastwave, the internal shock model requires that Lorentz factors of the shells causing flares must be less than the Lorentz factor of the blastwave when the shells are ejected.

Recent observations of Gamma-Ray Bursts (GRBs) by the Fermi Large Area Telescope (LAT) revealed a power law decay feature of the high energy emission (above 100 MeV), which led to the suggestion that it originates from an external shock. We analyze four GRBs (080916C, 090510, 090902B and 090926A) jointly detected by Fermi LAT and Gamma-ray Burst Monitor (GBM), which have high qual-

ity lightcurves in both instrument energy bands. Using the MeV prompt emission (GBM) data, we can record the energy output from the central engine as a function of time. Assuming a constant radiative efficiency, we are able to track energy accumulation in the external shock using our internal/external shell model code and show that the late time lightcurves fit well within the external shock model, but the early time lightcurves are dominated by the internal shock component which has a shallow decay phase due to the initial pile-up of shells onto the blast wave.

TABLE OF CONTENTS

LIST OF FIGURES

ACKNOWLEDGMENTS

There are so many individuals to whom I owe a debt of gratitude and I thank them here in this particular order.

To Dr. Bing Zhang, for being a patient teacher, a role model and my hero; you showed me the meaning of dedication, hard work and your love for GRBs has been an inspiration. I can only hope that a small fraction of your unique mind has rubbed off on me. When will I get to see your karaoke machine? To Dr. Stephen Lepp, for showing me the joy of classical mechanics, all over again. To Dr. Tao Pang, for your leadership and all the random discussions in the breakroom. To Dr. Proga, your grilling really did make me a better thinker and a more confident speaker; thank you. To Dr. Matthew Lachniet, for agreeing to be on my committee without knowing me much at all. To Dr. Lon Spight, for helping me through the thick of it.

To Bin-Bin Zhang, who showed me that not only do I only use 10% of my brain, I only use 10% of my computer as well. To Francisco, my friend and support system, I am so proud of you, even though I don't know that I have any right to be (also thanks for the scarf). I can't imagine two better academic siblings. To Tesla, thanks for the Yamazaki reference and for being a superstar. To Xue-Feng, for always being willing to help; how do you always know when I am missing a factor of $1 + z$? To all the new GRB groupies, I look forward to your promising research; if I can make your life easier, please let me know. To Matt, for fixing this Latex template and to Sandip for writing it. To Vivian, for loving Thomas Edison,

inventor of the light bulb.

To Khurram, for being my very best friend; you were the supergenius who always remembered napkins. To Jeremy, for showing me the meaning of generosity and integrity. To JW for always knowing how to make me feel better with math. To Benjamin Bayer, for teaching me philosophy. To Dr. Margaret Meixner, for opening your home to me and taking a chance on me-all because I pointed out that the axis was mislabeled on the qual. To Dr. Bruce Conway, for all things lunar and basset hound. To Dr. Jay Gallagher for telling me how great my ideas were, even though I am pretty sure they were originally yours and for lending me your office that one day.

To my Aunt Joan, for being carefree and always proud of me; the birthday is only the beginning. To my Aunt Carol, for your constant love, support and advice. To my grandma, Eleanor, for listening to me. To my grandpa, John, I didn't know you much at all, but I bet you could have made me laugh. To my grandma, LaVee, who started stories for me to finish. To my grandpa, Jerry, you can no longer tell me your war stories but I will celebrate Christmas on July 13, for the day in 1944 when it wasn't you. I hope you smile when I read this to you. To Dr. Douglas Peterson, for your love of music and for allowing me to know these great masterworks. To Cynthia, for always thinking that I am so much cooler than I actually am. To my best friend Brooke, for always knowing exactly what I am talking about; I'm pretty sure you were Nixon and I was LBJ; Mergels!!

To my brother, Jason, for being the translator between me and the outside

world; for taking me flying and always sharing your adventures with me. Please wash out your glass before you switch drinks. To my mom, Cindy, who showed me that sometimes you can get exactly what you didn't even know you wanted (and I'm not only talking about Hubey-Raccy-Snorty-Cooney-Fluffy either); I hope I showed you the same. You can hang this on the fridge. To my dad, Jack, who gave me my first HP calculator when I was 13, the sign that I was becoming a woman; I always wanted to be just like you. And last, but never least, to JD, for being the rock from which I could jump into the sea of stars. Thank you. < 3

This work is partially supported by NSF AST-0908362 and NASA under grants NNX08AN24G, NNX08AE57A, AR9-0006X, NNX09AT66G, NNX10AD48G.

PART I

WHAT ARE GAMMA-RAY BURSTS?

CHAPTER 1

DISCOVERY

After the signing of The Nuclear Test Ban Treaty, in 1963, The United States launched a series of satellites to monitor the globe with the purpose of uncovering any clandestine nuclear explosions. These satellites, called "Vela" from the Spanish "velar" meaning "to watch" were put in geocentric orbits with each pair of satellites at near opposite ends of a circular orbit (r $\simeq$ 1.2 x 10^5 km) so that no part of the Earth would ever be hidden from view (see Fig. 1). The satellites each had 6 Caesium iodide scintillation detectors that could measure radiation of energies 0.2 to 1.5 MeV and would look for an increase in the gamma-ray photon count that could signify another nation secretly conducting nuclear bomb tests [20]. A nuclear explosion would cause a tell-tale X-ray flash, followed by neutrons emitted from the source. The gamma-ray detector was chosen, in addition to an X-ray and neutron detector since gamma-rays would be radiated from an expanding debris cloud and could be detected even if the explosion was conducted behind a shield of some sort or on the far side of the moon where X-rays and neutrons would not escape. A simultaneous signal of X-rays, gamma-rays and neutrons would be the sign of a violation of the treaty. Instead, the detectors saw unexplained bursts of gamma-rays that were not coming from anyplace on the Earth[171].

Ray Klebesadel who was working at Los Alamos, assumed responsibility for the X-ray and gamma-ray instruments aboard the Vela telescopes in 1965. The Vela 5a, 5b and 6a, 6b pairs of telescopes had sufficient timing accuracy to determine that the bursts of gamma-rays the telescopes were detecting were clearly not coming from nuclear test ban violations and filed them away for future study. In 1972, Ian Strong, also at Los Alamos, began looking at the data on these events. In

1973, Klebesadel, Strong and another Los Alamos colleague, Roy Olson, published a paper describing gamma-ray bursts (GRBs) for the first time. The discovery paper cataloged 16 GRBs from 1969 to 1972 [79].

Timing accuracy of the onset of GRBs among the Vela 5 and 6 satellite pairs, which were very nearly evenly spaced in the same circular orbit, of ± 0.05 seconds allowed direction determination to the signal, since the difference in light travel time across the orbit, or "transit delay" of satellite pairs is just under 1 second. Two satellite observations of a single event constrains the directionality to a circle on the celestial sphere. For observations that involve three satellites, the two points of intersection of two such circles constrains possible positions of the event. This crude triangulation of the source was accurate enough to determine that GRBs were not coming from the Earth or the Sun and therefore were of "cosmic origin" [171]. Later, looking through the data from the Vela 3 and 4 satellites, Klebesadel and Olson found another event that had similar timing to other GRBs, even though these older version satellites did not have accurate enough timing to determine the direction. This event, called GRB 670702 remains the first known observation of a GRB [171] [1].

[1] GRB "phone numbers" are created by combining the two digit year, month and day of discovery. GRB 670702 was detected on July 2, 1967. If more than one GRB is detected in a single day, uppercase letters follow; GRB 080916C was the third GRB detected on September 16, 2008.

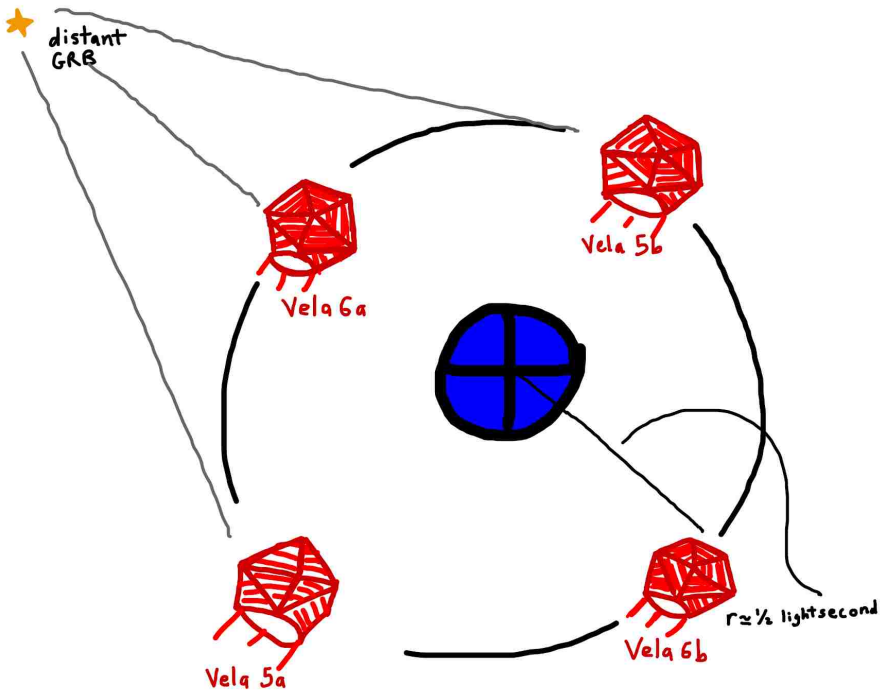

Figure 1 Not-to-scale depiction of a Vela 5 and 6 satellite pairs orbiting the Earth. Accurate timing of the signal delay allowed rough triangulation of GRB sources.

CHAPTER 2

BASIC OBSERVATIONS

Gamma-ray bursts (GRBs) are brief, intense flashes of radiation seen at cosmological distances throughout the Universe. For the short time that they occur, they outshine every other gamma-ray source in the Universe combined and appear to be one-time events; no GRB has ever been observed to repeat. Since the publishing of the discovery paper by Klebesedal, Strong and Olson in 1973, astronomers have been drawn to these fascinating events. In a conference in 1975, there were no fewer than 100 theories reviewed as to what could be causing GRBs, and none could yet be ruled out on the basis of observations [157]. The only thing that was clear was the need for *more* observations. Since that time a number of satellite telescopes have been launched dedicated to the mission of observing GRBs. In addition, ground based telescopes have observed these events in other energy ranges from radio to optical and these multi-wavelength observations have greatly enhanced our understanding of these mysterious events.

Telescopes

In the first twenty five years of the study of GRBs, there were many GRB detectors built. Focusing such high energy photons is no easy task, however, and no sharp images have ever been taken in gamma-rays. GRB detectors have come a long way, especially in the past few years, but the goal of GRB detectors have remained virtually unchanged: (i) to attain a low detection threshold so as not to obtain a bias in the sample of detected GRBs (ii)to have good energy resolution so that spectral features can more readily be seen (iii) to have accurate time resolution and (iv) to record data in as many energy bands as possible [147]. Some early GRB

detectors[147]:

- GINGA, a Japanese satellite experiment [128]
- HEAO-1, High Energy Astronomy Observatory [80]
- ISEE-3. the International Sun-Earth Explorer experiment [78]
- KONUS Russian built detectors [116]
- PVO, the Pioneer Venus Orbiter GRB Experiment [40]
- SIGMA, a French-Soviet detector onboard the Soviet GRANAT satellite [112]

For the most part, these detectors contributed modestly to the overall understanding of GRBs, but were nonetheless interesting experiments. For example, the KONUS experiment consisted of 6 scintillator detectors on both the Russian Venera 13 and 14 spacecraft at the ends of 3 perpendicular axes which could provide information on directionality of a GRB[147][116]. A copy of the KONUS device was also put aboard the American WIND satellite, launched in 1994. The ISEE-3 spacecraft was outfitted with a high resolution Ge detector and was sent into space in 1978, in a halo orbit about the L1 Earth-Sun Lagrange point. The detector aboard was shielded from the sun and radiatively cooled[147][78]. The GINGA satellite included a hard X-ray detector, which was the first observation of GRBs in this band, unfortunately, high energy X-rays give similar rough localizations[147][128]. References for these early detectors are given for interested readers.

It was not until 1991 and the launch of The Compton Gamma-Ray Observatory (CGRO) that finally some questions began to be answered (see Table 1 for a list of recent detectors). Onboard, there were four dedicated gamma-ray instruments including the Burst and Transient Source Experiment (BATSE)[47] which detected

a total of 2704 GRBs in its 9 years of operation. Since gamma-rays can not be easily focused, observations in this band always have large error circles, meaning that the precise location of the emitting culprit is not known. Within these error circles, there may be many distant galaxies which all are candidates for being the source of the GRB. These ambiguous results provided fuel for what has become known as "the great debate" over the origin of GRBs; are GRBs solar system, galactic or cosmological in origin? This debate, which went on for about 30 years, finally began to be settled by the large number of BATSE observations. The rough location estimates of BATSE bursts began to show a distribution that was uniform across the sky, showing no preferred direction or multipole moments [119]. If GRBs were of solar system or galactic origin, they should show some indication of being preferentially located along the plane of the galaxy or solar system, since that is where most of the matter in these systems lie. Instead, the fact that GRBs showed no statistically significant directionality indicated that they were most likely occurring in other galaxies which are also spread across the Universe isotropically.

In 1997, the Italian-Dutch satellite BeppoSAX [50] put the debate permanently to pasture. Named after the Italian astronomer Giuseppe "Beppo" Occhialini combined with what roughly translates to Satellite for X-ray Observing, this mission saw the first X-ray afterglows, which were theoretically proposed, allowing better localization of GRBs to several arc seconds after several hours of observation. This smaller search area and relatively short announcement time allowed ground based telescopes to find the optical and radio afterglow of some bursts. If the optical counterpart of a GRB could be detected, then the precise direction given by the optical observation could pinpoint a host galaxy whose redshift could then be found. The first X-ray afterglow ever detected was GRB 970228 [183] and the first redshift measurement of GRB 970508, at $z = 0.835$ [126] finally put the debate to

rest; GRBs were indeed of cosmological distance, making them the most energetic events since the Big Bang.

BeppoSAX had a mission expectation of 2 years, but was operational until 2002 when various systems started to fail and the orbit was decaying too rapidly to be useful; the deorbit happened in 2003. After exceeding the mission expectation of 2-5 years, the CGRO crashed into a remote area of the Pacific Ocean in a planned re-entry on June 4th, 2000. Both instruments were integral to our understanding and the HETE-2 satellite [74], launched in 2000, was able to continue their missions. The HETE-2 provided quality afterglow data and localizations good to 10 arc seconds which could quickly be sent to a network of ground based observatories for follow-up observations. It was responsible for finding the first unambiguous association of a GRB with a supernova (GRB 030329 with SN2003dh). The European Space Agency's INTEGRAL satellite, a sensitive gamma-ray detector launched in 2002 has uncovered a new class of low luminosity GRBs[174].

The Swift satellite [56], launched in 2004 was integral to multi-wavelength studies. Onboard are the Burst Alert Telescope (BAT[10]) which continually scans the sky looking to be triggered by an increase in gamma-ray flux, indicative of a GRB. The X-ray Telescope (XRT[23]) and UV/Optical Telescope (UVOT[155]) also aboard could then "swiftly" slew to view the same area of the sky as the BAT, collecting X-ray and optical lightcurves soon after the onset of the prompt emission, seen for the first time in a band other than gamma-rays. It is XRT's high angular resolution that has allowed position information for many bursts to narrow down a host galaxy. The first afterglow of a "short" burst, GRB 050509B [72] was discovered by Swift, indicating that the short and long GRBs may not be that different after all. It also allowed astronomers to break into the "dark ages" of the Universe with the first discovery of a GRB above redshift $z = 6$, the so-called "reionization

Table 1 GRB Detectors

Observatory	Instrument	Dates
CGRO	BATSE	1991-2000
BeppoSax	WFC, PDS	1996-2003
HETE-2	FREGATE, WXM, SXM	2000-2006
INTEGRAL	IBIS	2002-present
Swift	BAT, XRT, UVOT	2004-present
Fermi	GBM, LAT	2008-present

era" of the Universe with the discovery of GRB 050904 at $z = 6.29$ [75].

Most recently, the Fermi Telescope was launched with a mission to provide information about GRBs in an even higher and wider energy range than ever seen before. The Gamma-ray Burst Monitor (GBM[120]) monitors the sky for GRBs while the Large Area Telescope (LAT[27]) with a field of view of almost a quarter of the sky, waits to see GRBs as well. Together they span over 7 orders of magnitude in energy (see Fig. 2). There have so far been about 20 GRBs detected simultaneously with the GBM and LAT and about 500 detected by GBM alone. The LAT's extremely high energy range detected photons with astounding energies–up to 33 GeV and showed us that there is seemingly no limit to the energy with which a GRB can explode.

General Properties

It is estimated that 1000 GRBs reach the Earth each year, making them about 100,000 times rarer than their "distant cousins" supernovae. Of these GRBs which reach the Earth, the Swift Telescope detects an average of 1 burst every two to three days, with Fermi seeing a GRB about every other day as well. Even though

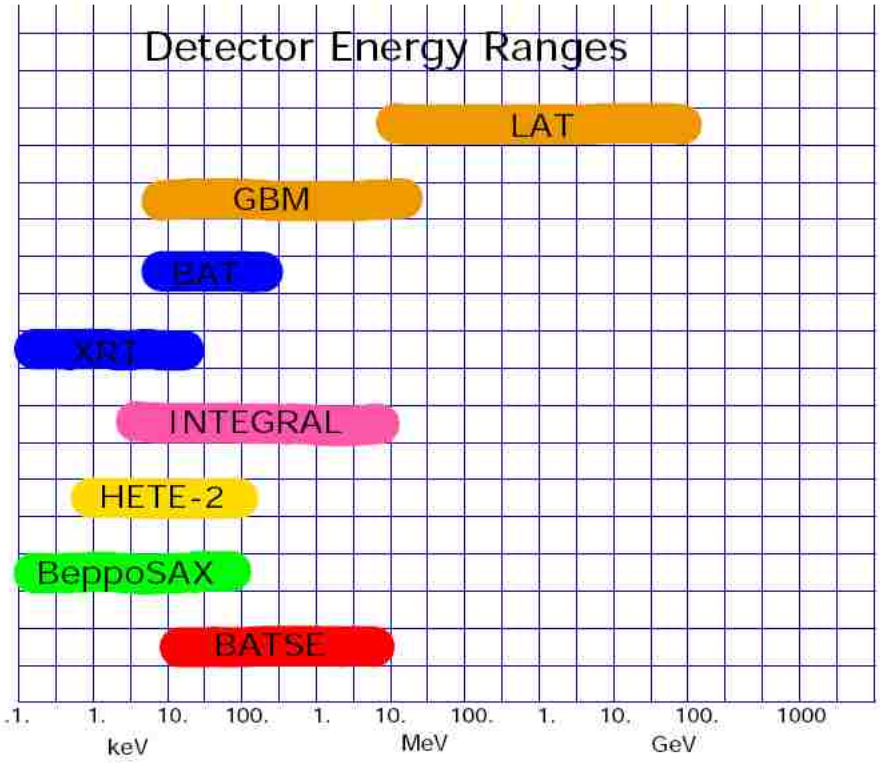

Figure 2 Energy ranges of GRB detectors.

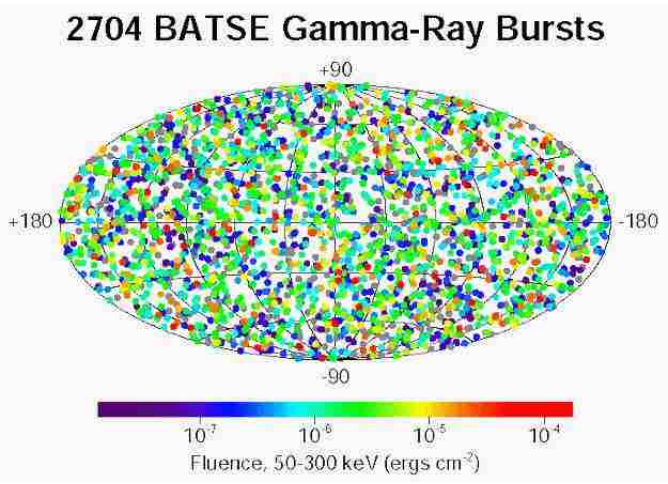

Figure 3 The isotropic nature of BATSE GRBs indicates that they are cosmological in origin. Source: [48]

the frequency of occurrence is very low in any given galaxy (typically 1 every 10^5 - 10^6 years [163]), so many galaxies spread over the sky and in the observational field of these telescopes make for a much more frequent observational rate here on the Earth. Such a low probability of occurrence has meant that even the closest GRB detected (GRB 980425) at $z = 0.0085$ [18] went off in a galaxy so distant that the light from this GRB took 0.117 Gigayears to reach us (see Table 2 for a list of notable GRBs). In the last 40 years of observation, no GRB has been detected in one of our galactic neighbors let alone the Milky Way which is both a blessing, since a GRB explosion within our own galaxy, beamed toward the Earth might mean the destruction of our atmostphere, and a curse, since a GRB occurring in a nearby galaxy would greatly enhance our understanding and perhaps allow us to pinpoint a progenitor in the same way that has been done with some supernovae.

Since their discovery, astronomers have wanted to classify GRBs with the ultimate goal of figuring out what could be causing them. It soon became clear that GRBs showed great variability from bust to burst in their lightcurves or a plot of the number of photons collected per second as a function of time (see Fig. 4). The spectrum of gamma-rays, the number of photons per unit energy $N_E = dN/dE$ is generally in the form of two smoothly connected power laws (see Fig. 5) or "Band function" [8] with mathematical form:

$$N_E(E) = \begin{cases} A\left(\frac{E}{100\mathrm{keV}}\right)^{\alpha} \exp\left(-\frac{\mathrm{E}}{\mathrm{E_b}}\right) & (\alpha-\beta)E_b \geq E \\ A\left(\frac{(\alpha-\beta)E_b}{100\mathrm{keV}}\right)^{\alpha-\beta} \exp(\beta-\alpha)\left(\frac{\mathrm{E}}{100\mathrm{keV}}\right)^{\beta} & (\alpha-\beta)E_b \leq E \end{cases} \tag{2.1}$$

where α and β are the power law photon spectral indices below and above the break energy E_b in the asymptotic regime and A is a normalization factor. The break energy can be written as $E_b = E_p/(2+\alpha)$, where E_p is the spectral peak

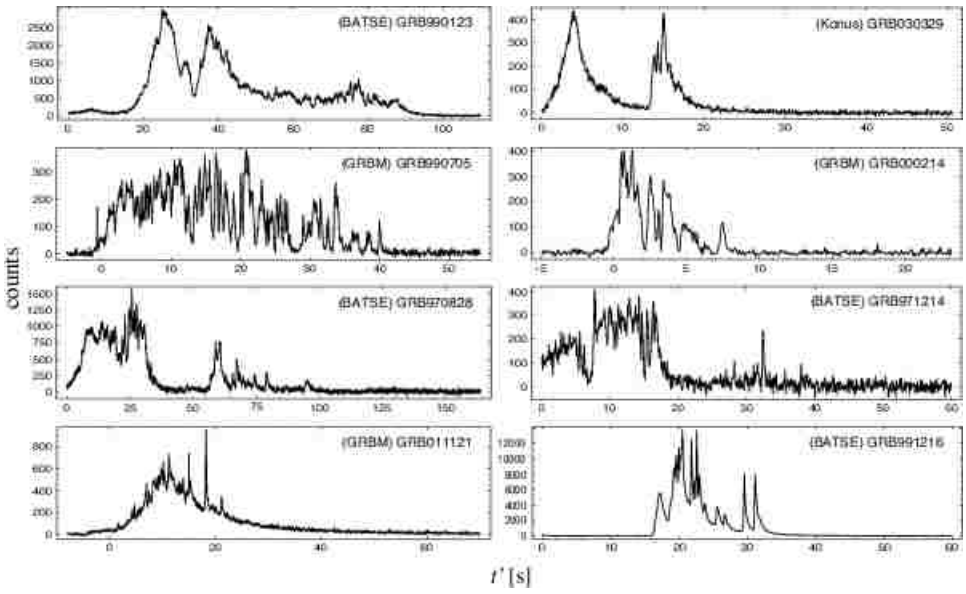

Figure 4 GRB prompt emission is highly variable and no two bursts are the same. [21]

energy in the GRB energy spectrum.

The same spectrum can be presented as the number of photons per decade of energy which is also a Band function, but with different slopes before and after the break (see bottom panel of Fig. 5). The break energy, E_b which is the transition between these two spectral components occurs in the range of $0.01 - 1$ MeV for most bursts. There are a few bursts whose spectra deviate from this shape, but in general, the spectra of GRBs is "non-thermal", meaning that they are not the result of gas or plasma which has had time for the particles to interact, coming into thermal equilibrium. Thermal spectra, like that of the sun are called "black bodies" and have a well-understood and familiar shape and are due to the distribution of speeds that the particles take on when they have had time to come into equilibrium.

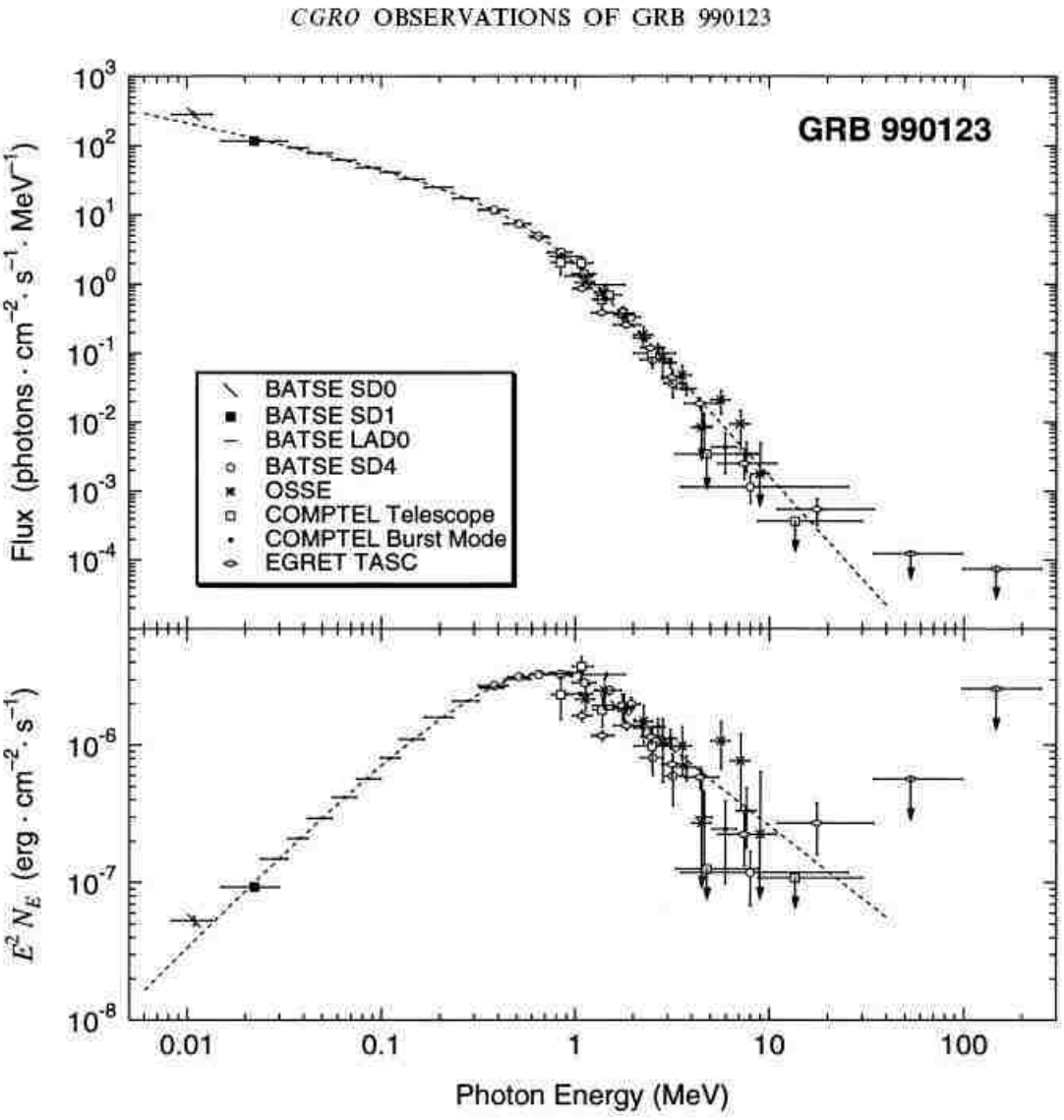

Figure 5 A typical GRB spectrum in the shape of a Band function. Source: [22]

Table 2 Firsts and Notable GRBs

Burst	Redshift	Detected by	Notes
GRB 670702		Vela 4	First GRB detected [171]
GRB 970228	0.695	Beppo-SAX	First X-ray afterglow, first optical afterglow [19][31][177]
GRB 970508	0.835	Beppo-SAX	First radio afterglow, first redshift measured [126][49]
GRB 980425	0.008	BATSE	Closest GRB and first associated with a SN (SN 1998bw) [18]
GRB 990123	1.6	BeppoSAX	First burst observed simultaneously in optical and gamma-rays [22]
GRB 030329	0.168	HETE-2	Second and more definite SN association (SN 2003dh) [65]
GRB 050509B	0.225	Swift	First short burst with detected afterglow and possible elliptical host galaxy [72]
GRB 050724	0.258	Swift	First short burst with radio, optical and X-ray afterglow and association with an elliptical galaxy [13]
GRB 060218	0.0331	Swift	First GRB with a SN which could be tracked immediately after the burst [127]
GRB 060614	0.125	Swift	Close "long" burst with no SN association [52]
GRB 080319B	0.937	Swift	Brightest optical event observed and the first and only GRB to be seen with the naked-eye to date [146]
GRB 080916C	4.35	Fermi	First bright GRB detected in wide energy range [192]
GRB 090423	8.2	Swift	Official record holder for the most distant observed object in the Universe[158]
GRB 090429B	9.36	Swift	Tenuous record holder for the most distant observed object in the Universe[33]
GRB 090510	0.903	Fermi	Short GRB detected with Fermi with highest recorded energy photon of 33 GeV [148][192]

Energetics

If the millisecond variability[16] or slower periodic signals[53] of GRBs (typically of some seconds) is due to rotation at the source a lower limit on the density of the source can be found. The centrifugal force must be greater than the gravitational force at the surface, implying a dense region of

$$\rho \geq \frac{3\pi}{GP^2} = 1.4 \times 10^{10} \left(\frac{P}{10\mathrm{ms}}\right)^{-2} \mathrm{g/cm^3} \tag{2.2}$$

where P is the rotation period of the source. Typical periodicities imply a white dwarf, neutron star or black hole [147], but there are other reasons to assume a compact object is needed. The "one-time" nature of GRBs along with the energy released strongly indicate that GRBs are related to some cataclysmic event such as the formation of a black hole.

The propensity for some astronomers to assume that GRBs were of galactic origin is clear–the flux levels (energy per second per unit area) detected at the Earth from a single GRB of $10^{-5} - 10^{-7}\mathrm{ergs/s/cm^2}$ indicate that if GRBs are of cosmological origin, the energy released must be enormous. If they were instead, closer, the total amount of energy needed to produce the flux seen would be "more reasonable".

$$E_{\gamma,iso} \simeq 4\pi D^2 F = 10^{50}\mathrm{ergs} \left(\frac{\mathrm{D}}{3000\mathrm{Mpc}}\right)^2 \left(\frac{\mathrm{F}}{10^{-7}\mathrm{erg/cm^2}}\right) \tag{2.3}$$

where F is the fluence and we have left out cosmological factors for the time being.

This huge isotropic energy makes GRBs the brightest explosions in the Universe, out-powering SN by a factor of $\simeq 1000$ with $E_{\gamma,iso} \simeq 10^{53} - 10^{55}\mathrm{ergs}$. The output in gamma-rays is comparable to the rest mass of a solar sized star or the energy that would be released by converting all of the Sun's mass into energy and emit-

ting it in a matter of seconds. Consider that an atomic bomb releases an amount of energy almost 25 orders of magnitude less ($\simeq 10^{20}\mathrm{erg}$) or about the same amount of energy contained in one gram of matter. If the energy is beamed or released in a jet of opening angle θ_j instead of a spherically released from the GRB central engine (CE), the energy budget can be reduced (and the event rate increased). Two symmetric jets would subtend a solid angle of $\Omega_j \simeq \pi\theta_j^2$ so for typical jet opening angles of a few degrees, this could reduce the amount of energy needed to create the observed flux by a factor of $\frac{4\pi}{2\Omega_j} \simeq 300 - 500$, giving a more moderate value for $E_{\gamma,jet} \simeq 10^{51}\mathrm{ergs}$.

Without knowing exactly what this "central engine" (CE) is, we can put some constraints on it. First, knowing that $10^{51}\mathrm{ergs}$ of energy is released in the form of non-thermal gamma-rays over a time scale of 10 seconds or less indicates a highly relativistic emission region. By the late 1970s, it was realized that any theory put forward would have to overcome a serious hurdle–the compactness problem [164]. The typical variability seen in GRBs of a few milliseconds told us that the central engine had to be small, restricted by the amount of time it takes photons to travel across it $R \leq c\delta t \sim 3000\mathrm{km}$. At the same time, generating photons carrying $10^{51}\mathrm{ergs}$ of energy in such a small region would lead to pair production which is the process by which two high-energy photons can combine to form an electron positron pair ($\gamma\gamma \rightarrow e^+e^-$). Even if there are no pairs in the region to begin with this pair creation would raise the optical depth to $\sim 10^{13}$ in just a few microseconds[141].

$$\tau_{\gamma\gamma} = \frac{f_p \sigma_T F D^2}{R^2 m_e c^2} \tag{2.4}$$

$$\tau_{\gamma\gamma} = 10^{13} f_p \left(\frac{F}{10^{-7}\mathrm{ergs/cm^2}}\right)\left(\frac{D}{3000\mathrm{Mpc}}\right)^2\left(\frac{\delta t}{10\mathrm{ms}}\right)^{-2} \tag{2.5}$$

where f_p is the fraction of photons with sufficient energy for pair production, σ_T is the Thompson cross-section, R is the size of the emitting region, m_e is the mass of the electron and c is the speed of light. These pairs will then Compton scatter lower energy photons. The result will be that we will not be able to observe any photons being emitted from this region. Further, any gamma-rays that we did see would be completely thermalized from reactions with these pairs. Yet we manage to see photons from this region and with a completely non-thermal spectrum; this is the compactness problem[141].

There has only been one solution to the problem found that does not involve "new physics" beyond the standard model. The solution is to use ultra-relativistic matter particles or strong magnetic fields to transport the energy from the optically thick source to a larger radius where this energy can be converted to electromagnetic radiation either through shocks, in the case of matter particles, or magnetic reconnections, in the case of strong magnetic fields. If the energy is transported via matter particles, this ejecta must be moving at relativistic speeds, with Lorentz factors, $\gamma = 1/\sqrt{1 - v^2/c^2}$ in the range of $\gamma \sim 100 - 1000$ in order to produce the gamma-rays we see[141][157].

The variability combined with the large amount of energy released indicates that the observed gamma-ray emission and afterglow must arise from a highly relativistic region. The energy emitted over this putatively small emission region ensures that the Eddington luminosity (L_{Edd}) will be exceeded. A system balancing pressure and gravity can become unstable when the accretion becomes too high. If a system has an accretion rate that is too high, the luminosity caused by this accretion can create an outward pressure greater than that of gravity, thereby stopping the accretion. Where this tipping point occurs is called the "Eddington Luminosity" or "Eddington limit" after the astronomer Sir Arthur Stanley Edding-

ton. Equating the acceleration caused by radiation pressure with the gravitational force per unit kg gives this limit:

$$\frac{L_{Edd}}{4\pi r^2}\frac{\sigma_T}{m_p c^2} = \frac{GM_{CE}}{r^2} \tag{2.6}$$

$$L \leq L_{edd} = \frac{4\pi G M_{CE} m_p c^2}{\sigma_T} = 1.25 \times 10^{38} \mathrm{erg/s} \left(\frac{\mathrm{M_{CE}}}{\mathrm{M_\odot}}\right) \tag{2.7}$$

where M_{CE} is the mass of the central engine (presumably a black hole), $M_\odot$ is the mass of the sun and m_p is the proton mass. The luminosity in GRBs exceeds L_{Edd} by $\sim 10^{12}$ times, causing the CE to violently fling matter outward at relativistic speeds. This outward pressure will create a "fireball" heating electrons, protons and even neutrons as they travel away from the CE[122]. If an amount of energy E is injected into the fireball, it will accelerate until given bulk Lorentz factor $\gamma = (E+Mc^2)/Mc^2$ where M is the rest mass in the accelerated protons[122]. The fireball will then continue to move outward into the ambient medium, this first explosion (the CE may eject many "shells" of matter before it is finished) is called the blastwave. We have observed single photons from GRBs with very high energies, with the record of 33 GeV from GRB 090510[192]. These highest energy photons can constrain the Lorentz factor of the blastwave.

Relativistic effects can fool us and lead us to wrong conclusions when not taken into account. We can use them to explain how we are able to see >30 GeV photons from a GRB. In a plasma, photons randomly cross paths at various angles and photons with energy $> 511\mathrm{keV} = \mathrm{m_e c^2}$ (the rest mass of an e^+ or e^-) can annihilate with other target photons whose energy is $E_{target} \geq m_e c^2 - E_{e^+e^-}$ so that this target photon will have enough energy, when added to that of the incoming photon to produce an e^+e^- pair. When a photon with energy E interacts with another target

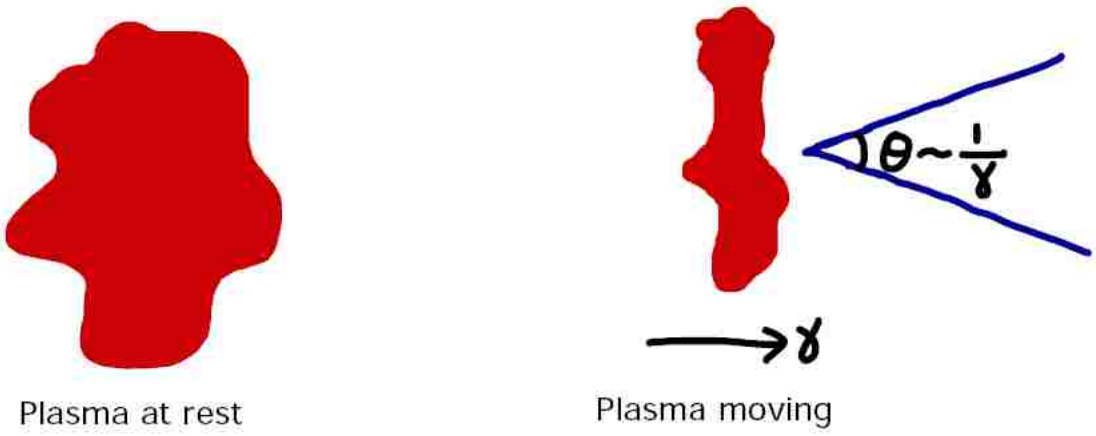

Figure 6 The photons emitted from a plasma moving at relativistic speed γ are beamed into a cone of angle $1/\gamma$.

photon, the energy in the center of mass frame is $2\sqrt{EE_{target}}$. So two photons with energy roughly $= 511\mathrm{keV}$ can annihilate to produce pairs since $\sqrt{EE_{target}} \leq m_e c^2$ is sufficient energy to produce a pair. The observed spectrum contains many photons with energy $\sim 511\mathrm{keV}$ which could interact with each other and even a few percent of gamma-ray photons with very high energy which could interact with lower energy photons to produce pairs as well[122]. If the plasma moves at relativistic speed, the photons we see are collimated into a narrow cone of opening angle $1/\gamma$ radians along the jet axis. This relativistic jet motion causes the photons to appear beamed into the jet direction in the observer frame (see Fig. 6), just like an missiles dropped from an airplane appear to move obliquely with respect to the ground, even though they are dropped perpendicular to the airplane's motion[122]. So beamed photons do not in fact meet in all random directions, but instead meet at only shallow angles of incidence. It is these "grazing angle collisions" that allow high energy photons to escape instead of being annihilated to form pairs. Just as

a collision between two race cars is much less likely to be fatal if the cars collide in a grazing manner, photons that meet at grazing angles need to have much more energy in order to annihilate. The threshold condition can now be re-written taking the angle of incidence, θ of the two photons into account[122].

$$EE_{target} > \frac{(m_e c^2)^2}{1 - cos\theta} \sim \frac{4 m_e c^2}{\theta^2} \tag{2.8}$$

Knowing that the majority of photons are near E_b in the photon spectrum (see Fig. 5), which is typically at an energy of $\sim 1\mathrm{MeV}$, a high energy photon, such as a $30\mathrm{GeV}$ photon interacting with a typical photon implies[122]

$$\gamma \geq 200 \sqrt{\left(\frac{E}{30\mathrm{GeV}}\right)\left(\frac{E_{target}}{1\mathrm{MeV}}\right)} \tag{2.9}$$

Empirical Relationships

The prompt lightcurves of GRBs are diverse (see Fig. 4). Long and short bursts can have a few or many pulses with periods of quiescence in between, with highly structured pulses. Prompt emission has been characterized using a number of parameters such as burst duration, variability, lag, pulse rise/fall time, fluence, E_{iso} and E_{peak}. Within this parameter space, astronomers have searched for correlations and have found a few. The most widely discussed correlations are shown in Fig. 7 which are based on statistical analysis and so often are not accompanied by physical explanations[55].

The most discussed relation is the so-called Amati relation [5] which is a correlation between the peak energy of a burst and the isotropic energy.

$$E_p = 100 \text{ keV} \left(\frac{E_{iso}}{10^{52} \text{ erg}}\right)^{1/2} \tag{2.10}$$

Although there is a large scatter within this relationship, there seems to be a strong correlation, although some authors have discussed that this might be an instrument or observational effect[129][9]. The Yonetoku relation is a similar correlation between peak energy and luminosity, $E_p \propto L_{iso}^{1/2}$ [187] which shows less scatter (see Fig. 8). Excellent temporal resolution of some bursts has allowed the measurement of E_p in different time slices which can vary erratically over the course of a burst[143]. Using an average value for E_p may therefore not be representative of any physical process at the burst sight although it seems that the Yonetoku relation may be satisfied in each time slice (see Fig. 9)[60]. The Liang-Zhang relation [105] shows a strong correlation between the isotropic gamma-ray energy $E_{\gamma,iso}$, the peak energy of the spectrum in the rest frame, E'_p and the rest-frame break time of the optical afterglow light curves, t'_b

$$\frac{E_{\gamma,iso}}{10^{52}\mathrm{ergs}} = (0.85 \pm 0.21) \left(\frac{E'_p}{100\mathrm{keV}}\right)^{1.94\pm0.17} \left(\frac{t'_b}{1\mathrm{day}}\right)^{-1.24\pm0.23} . \tag{2.11}$$

Cosmological Uses of GRBs

GRBs are the highest redshift objects ever discovered and with the population growing, the question arises as to whether it is possible to use them to constrain cosmology in the same way Type Ia supernovae are used. Type Ia SN happen when a white dwarf star accumulates mass from a companion, reaching its limit and exploding. These supernovae are special because they are what is known as "standard candles". Since the amount of mass a white dwarf can collect before exploding is as set value, every time a Type Ia SN explodes, it always releases the same

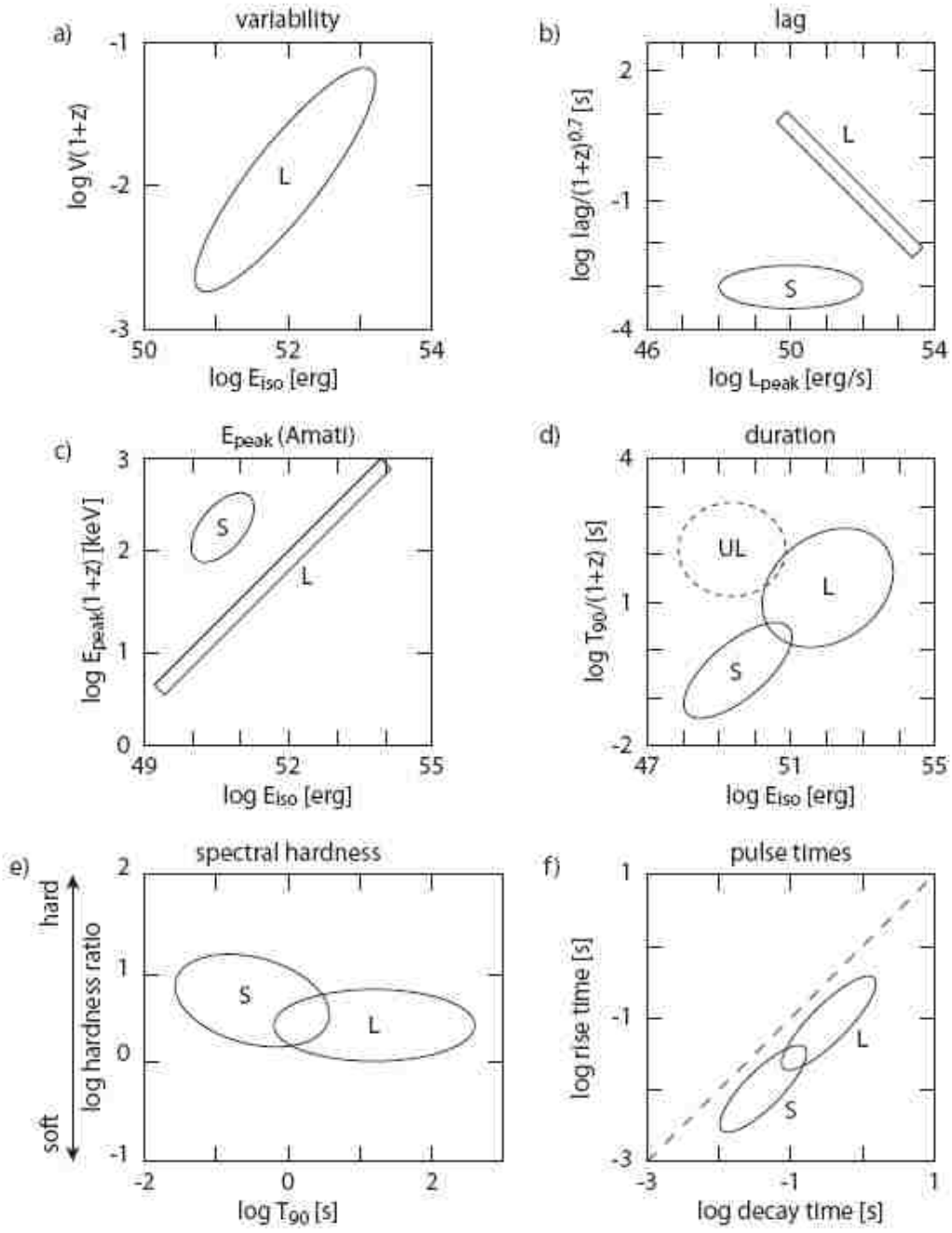

Figure 7 The most widely discussed correlations between various prompt emission properties for GRBs. Source:[55]

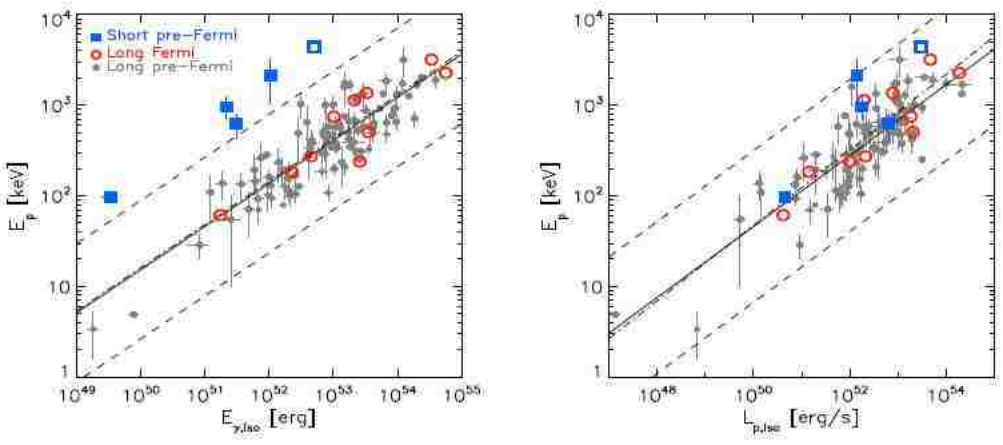

Figure 8 Rest frame peak energy versus isotropic energy (left) and luminosity (right) of 95 long GRBs detected before Fermi (filled grey circles). Ten Fermi long GRBs with measured redshift are shown by the open (red) circles. GRB 090510 is shown by the open (blue) square. The filled (blue) squares are 4 other short GRBs. The solid line is the best fit to the pre-Fermi sample, while the dashed lines represent its 3 σ scatter. Source:[60]

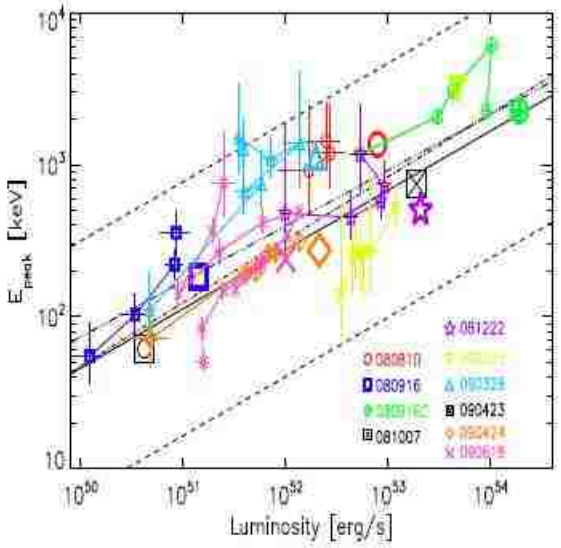

Figure 9 Where time resolved properties of ten long Fermi GRBs lie with respect to the Yonetoku relation. Source:[60]

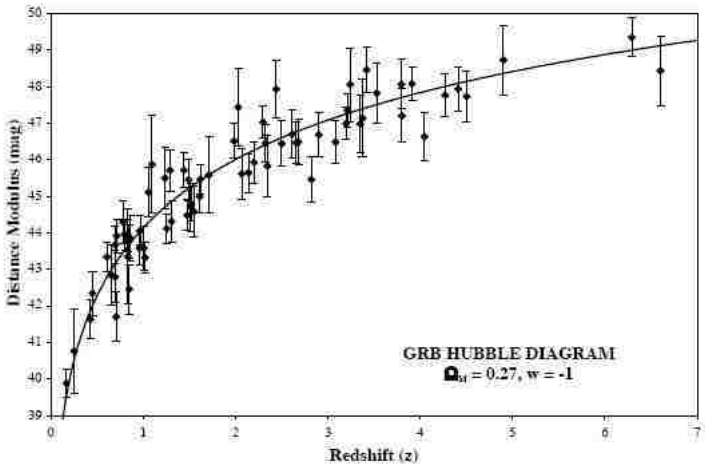

Figure 10 The GRB Hubble Diagram for 69 bursts with $0.17 < z < 6.2$. Source:[162].

amount of energy and therefore allows us to measure the distance to this event, just like measuring the brightness of thousands of identical light bulbs spread out over a field allows us to calculate the distance to each one. The great amount of energy released in a GRB allows us to probe the Universe to much greater distances than Type Ia SN, but are all GRB "light bulbs" the same? The large amount of scatter in the relations above ensures that no single relation could be used to put constraints on cosmic expansion or whether the fine structure constant has changed in the past, but perhaps using many of the relationships simultaneously can give a rough constraint. Spectral lag, variability, spectral peak photon energy, time of the jet break, and the minimum rise time all have correlations to GRB luminosity with varying quality. Using all of these properties to derive independent distances and combining these as a weighted average gives a rough constraint on the far-z end of the Hubble Diagram (see Fig. 10)[162].

The Afterglow

On February 28th, 1997, near the tenth anniversary of SN 1987A, BeppoSAX detected soft X-ray emission from the same place where GRB 970228 had gone off just seconds before[31]. Accurate pinpointing of the location allowed optical ground based telescopes to observe the "afterglow" for the first time[177]. The afterglow had been predicted for at least four years, but it had never been observationally verified. Not long after, GRB 970508 showed astronomers the first afterglow ever measured with a radio telescope[49]. It is these afterglows that have allowed the accurate pinpointing of host galaxies, making redshift measurements of GRBs possible. Since they were first discovered, afterglows have been collected for hundreds of bursts and show a much more regular pattern than the prompt emission. In fact, the afterglow flux seems to follow a regular decaying powerlaw or broken powerlaw. The powerlaw decay is expected if the afterglow is due to synchrotron radiation of a relativistically expanding blastwave and that theory seems to well-explain the observations. Even though it was BeppoSAX that first discovered the afterglow, it was Swift with its multi-band detectors onboard dedicated to studying GRBs that opened a brand new era in the study of afterglows. See Fig. 11 for two examples of broadband afterglow detection.

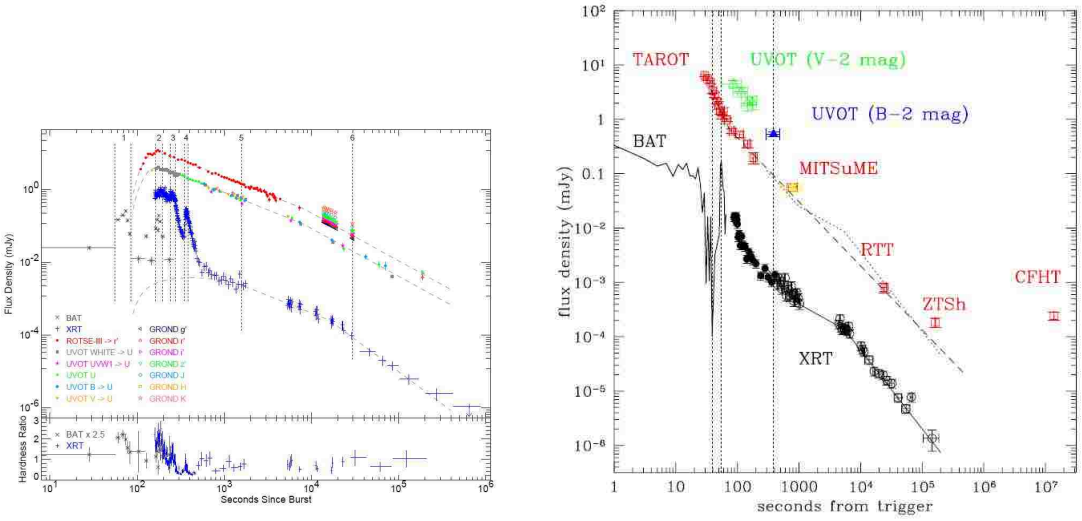

Figure 11 Multi-wavelength observations of the afterglow for GRBs 081008(left) and 060111B (right). Source:[190][170].

CHAPTER 3

PROGENITORS AND HOST GALAXY OBSERVATIONS

The typical nomenclature when talking about GRB progenitors has been to divide them into categories of "long" and "short" bursts. Although the duration seems to be an important feature in the classification of bursts, the ultimate goal is to determine the progenitor of these bursts, rather than just continuing to classify them phenomenologically. In that vein, here we will divide progenitors into Type I (merger events) and Type II (collapsar events) (see Fig.12). These classifications arise from the observational evidence, but attempt to integrate that evidence into a theory; rather than treating observations as a show pony, we treat them as a workhorse which will bring us to our destination. It soon became clear, even in the observation of the very first bursts with the Vela satellite [79], that there were two distinct types of bursts. The less typical, less often observed was a short burst lasting only a few milliseconds up to a few seconds. BATSE with its large GRB sample was able to detect many of these "short" bursts, with about 1 in every 3 GRBs detected fitting into this category. From the BATSE catalog came the statistical evidence to supplement the anecdotal evidence that short and long GRBs were indeed different populations (see Fig. 13). Bursts were classified by duration or T_{90}, the amount of time for 90% of the burst fluence to be observed. A histogram plotting the distribution of T_{90} values shows a clear bimodal signature, suggesting two distinct populations. Short bursts have durations of 0.2 milliseconds up to 2 seconds whereas long bursts can last anywhere from 2 seconds to 200 seconds or longer. Further classification of bursts in terms of spectral "hardness" shows a separation of the same two classes [145]. The "hardness" of a burst is determined by taking the ratio of burst energy measured in two different detector channels. The

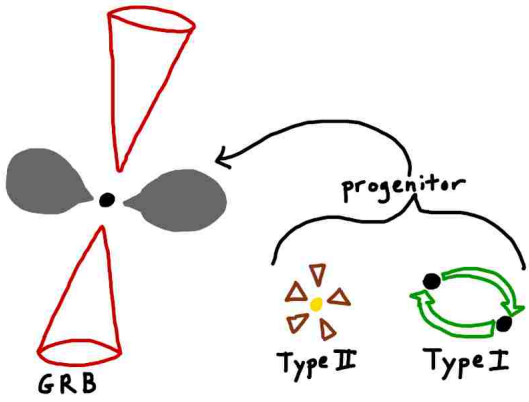

Figure 12 Type I (merger) and Type II (collapsar) progenitors.

separation of bursts in these two spaces suggests that there may be two different types of GRBs, but doesn't explain whether those two types are different manifestations of the same progenitor event or due to different progenitors entirely. The evidence for two different progenitors is fair and comes from observation, since merger progenitors and collapsar progenitors should live (statistically) in different types of galaxies or in different parts of the same types of galaxies.

Type II/Long

Observed more often than short ones, GRBs in the long class have a number of properties that distinguish them short GRBs and indicate that they are of collapsar origin; in other words, due to the death of a massive star[184]. In the first years after the discovery of GRBs, the collapsar model seemed unattractive as there was already a class of objects that are caused by the collapse of massive stars: supernovae (SN).

Already in the Vela era, astronomers searched for the connection between GRBs and SN, searching for any coincidence of a GRB with an optically detected SN.

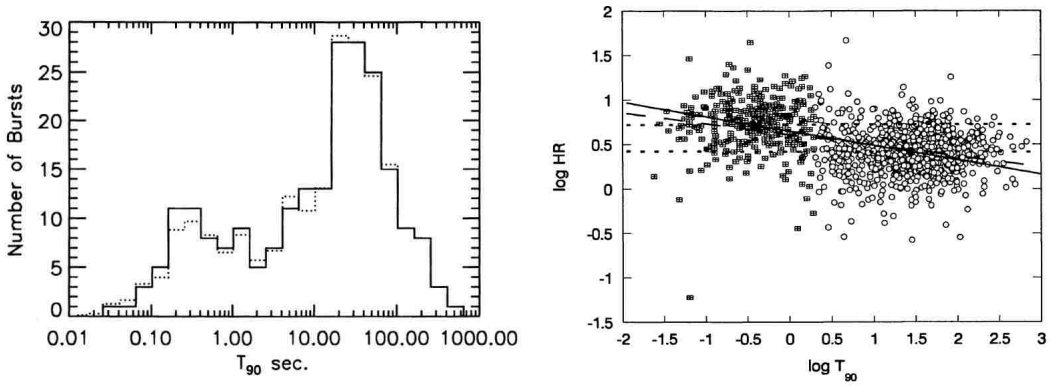

Figure 13 Left: Histogram of T_{90} for 222 GRBs in the BATSE sample shows a bimodal distribution of times. Source:[84]. Right: The hardness ratio of 1174 BATSE bursts divided into 304 short (squares) and 875 long (circles) bursts also suggest two distinct populations. Source: [145].

Colgate (1968) had predicted that SN might emit gamma-ray radiation[30], but even though searched for, a GRB/SN association was not found until 1998. The long burst 980425 was the first GRB associated with a SN (SN 1998bw) detected in a close ($z = 0.168$) spiral galaxy[18]. It would be a long wait until the next association of GRB 030329 and SN 2003dh in 2003, confirming that the first association wasn't a chance coincidence[65]. In 2006, GRB 060218 was discovered and associated with SN 2006aj, and detailed measurements of this GRB showed that GRBs associated with a SN can be fairly weak in terms of energy radiation and the associated SN was comparatively weak indicating the explosion of a smaller star[117]. Two facts emerged from these observations: (1) It seemed that any GRB that went off close enough to us to make a SN detectable, a SN would always be found and (2) that GRBs are always associated with a certain type of SN: Type Ic. Type Ic are a special, rare class of SN that have no hydrogen lines and no helium lines in their emission spectra. The spectra of the Type Ic SN associated with GRBs show that they are

also broad-lined, indicating high velocity ejecta of $\geq 30,000$ km/s at the source[76]. These SN are caused by stars that have apparently been stripped of, or lost their outer hydrogen and helium envelopes.

Long GRBs are most likely to be associated with spiral or star forming (SF) galaxies, and a look into where within these galaxies long GRBs occur reveals that they prefer the brightest parts of these galaxies. Taking a photo of a GRB host galaxy and counting the fraction of pixels fainter than the pixel in which the GRB has occurred, one can create a so-called "Fruchter Diagram"(see Fig. 14). Comparing the fraction of a galaxy that is fainter than core collapse SN reveals that these two data sets are inconsistent with having come from the same population. Fortunately, studies of the subset of SN of Type Ic have shown that these SN are also found within the brightest part of their host galaxies and are consistent with coming from the same population as GRBs (see Fig. 14)[51][76].

Coming from the other end, studying SN of type Ic shows that of these, those that are associated with a GRB are also of a special type. GRB SN (i.e. those detected because a GRB went off in that location) typically have very high level of radio emission compared to Type Ic SN detected in a traditional SN search (see Fig. 15). Turing the problem on its head, in 2009, a Type Ic SN was detected with an unusually high level of radio emission, comparable to that of a GRB SN. SN 2009bb looked like a typical SN associated with a GRB, yet no GRB could be found after an extensive search through archival data in the Swift and Fermi telescopes [167]. Perhaps there was no GRB associated with this SN, but more likely this observation opens a door to another way of finding a GRB SN association coming from the search for these types of SN and then pointing GRB telescopes to look for an associated GRB. Adding to the GRB SN association puzzle, GRB 060614 whose optical afterglow indicated its close distance ($z = 0.125$) was never associated with

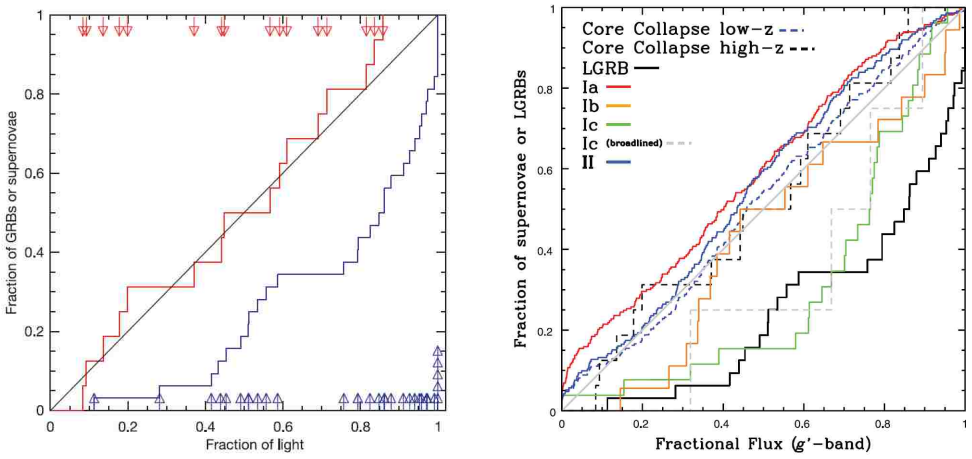

Figure 14 Where are GRBs located in terms of the light of the host galaxy? Left: Cummulative histogram of GRBs (blue) and core collapse SN (red) show that long GRBs are located in the brightest parts of their host galaxies and GRBs and SNs seem to be from different populations. Source:[51]. Right: The distribution of Type Ic SN and long GRBs appear to be of the same population. Source: [76].

a SN, even with the deep searches performed[191].

Type I/Short

Swift, with XRT providing relatively small error circles, slewed to GRB 050509B, which was the first short burst detected with an afterglow. The hunt was on to try to find the host galaxy of this burst as it might provide evidence for the progenitors of short bursts. The XRT error circle, of size 9.3" showed a large elliptical galaxy peeking in (see Fig. 16)[57]. Although the optical afterglow was searched for, it was never found and besides the obvious elliptical galaxy, a handful of fainter galaxies were found within the error circle. The association of a short GRB with an elliptical galaxy would remain tenuous, but not for long. GRB 050724 was the first short burst detected with radio, optical and x-ray afterglows and the first unambiguous association with an elliptical galaxy [13]. This was an important association

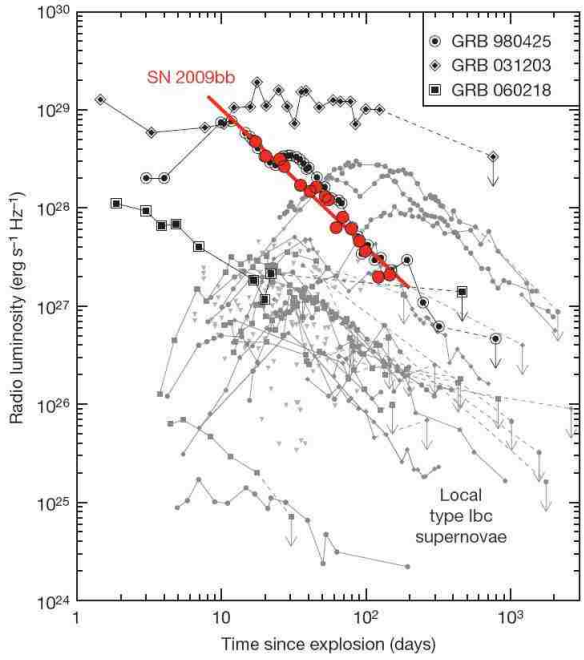

Figure 15 Gamma-ray burst SN appear to have more energetic radio emission than other Type Ic SN. SN 2009bb is shown in red, a SN with radio emission similar to GRB SN, but an associated GRB was never found. Source: [167].

in solidifying that claim that short GRBs were of merger origin. Elliptical galaxies contain little if any recent star formation and are composed mainly of older stellar populations. Although star forming galaxies may contain regions with older stellar populations, elliptical galaxies by contrast contain virtually no new stars. Since a compact object such as a NS takes at least 1 Myr to form, they are likely to be associated with these "older" galaxies and an association with an elliptical galaxy indicates that there is virtually no chance that short GRBs are associated with stellar collapse. Furthermore, there was no SN associated with this burst. At a redshift of $z = 0.257$, it would be presumably easy to detect a SN within this galaxy if one existed. Although absence of evidence is not evidence of absence, this extra little piece of the puzzle leads us to think that short GRBs may indeed be of Type I (or merger type).

Since that time, the picture has become a little less clear as short GRBs have been associated with star forming (SF) galaxies as well as ellipticals, in fact the majority of short GRBs with detected afterglows have been found in SF galaxies. At first this may seem like a contradiction to the short-Type I association, but luckily more detailed observations have regained some of the lost ground. When short GRBs are found within SF galaxies, these galaxies have a lower specific star formation rate and have a higher metallicity than those of long GRB hosts (see Fig. 17) [14]. Lower star formation rate suggests older star populations within the galaxy and higher metallicity suggests this as well, since many SN need to have had time to go off, polluting the galaxy with metal-rich material [14][100]. Further it has been suggested that even the short GRB which occur in SF galaxies occur in a "faint" position within these galaxies. Faint regions of a galaxy are associated with old stellar populations. Short GRBs seem to lie in the outermost regions of their star forming host galaxies. It is in the outer regions of a galaxy such as the Milky Way

where the older stellar populations can be found[14].

Of 20 short GRBs with optical afterglow, 5 have no coincident host galaxies down to $>$ 26th magnitude [15]. meaning that either the host galaxies of these bursts are either very faint or the GRB was far outside of a host when it went off. This suggests that whatever the progenitor of short bursts is, it could have a higher propensity to experience large gravitational "kicks" causing it to be ejected from its host galaxy. Looking at the galaxies within the the near field of the GRB localization shows a statistical overabundance of galaxies with a low probability to exist there suggesting that short GRBs could indeed be associated with a host galaxy but very far from it[15].

Type I events are thought to be due to compact objects, either the merger of a pair of neutron stars (NS-NS), a neutron star and a black hole (NS-BH) or perhaps even a merger involving a NS or BH and a white dwarf (WD). The event rate of short GRBs, estimated to be $0.4 - 1.2\mathrm{Myr}^{-1}$ is consistent with the rate of formation of these types of compact object systems [100], further solidifying the case for short GRBs being of Type I (merger) origin.

Unclear Classifications

Back to the puzzle of the "missing supernova", it seems that the $T_{90} \sim 100$ second duration of GRB 060614 would put it firmly into the long category, but a detailed look at the lightcurve reveals a short spectral lag and a few initial short hard spikes followed by a softer emission tail – all characteristics more consistent with short bursts [58]. Deep searches have put stringent limits on a SN association, making the non-detection of one evidence that this burst is more likely of Type I origin [52].Bursts detected at high redshift pose another problem. The high redshift bursts GRB 080913 at $z = 6.7$ [66] and GRB 090423 at $z = 8.2$ [158] each have

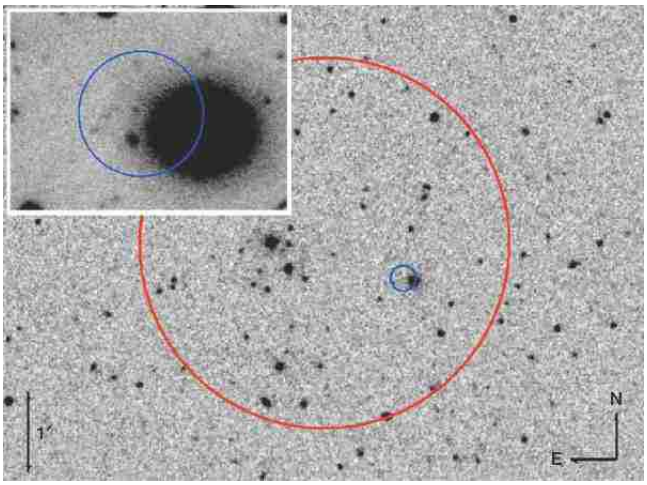

Figure 16 Observations of GRB 050509B. The large red circle is the BAT position error circle, and the smaller blue circle is the XRT position error circle. The inset shows a blow-up of the region of the XRT error circle from 8.2-m VLT-Antu telescope at the European Southern Observatory. Source: [57].

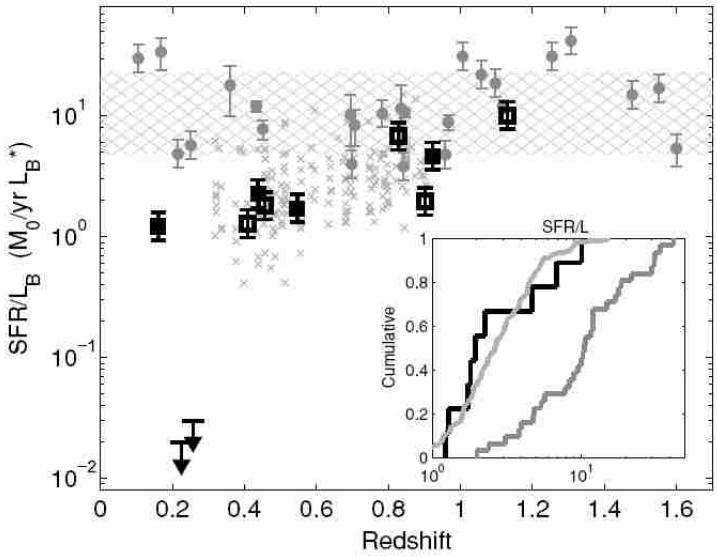

Figure 17 Observations of short GRB host galaxies reveal a lower star formation rate. Gray points are long GRB hosts and black points are for short hosts. The inset shows the cumulative distribution function of the two GRB populations as distinct. Source:[14]

a redshift-corrected duration $T_{90}/(1+z)$ shorter than 2 s, with a hard spectrum typical for short/hard GRBs[66]. This raises a question as to the progenitor of these two bursts.

An experiment performed by Zhang et al.(2007)[191] showed that producing a "pseudo" bursts similar to GRB 080913 and 090423 could determine how those bursts would appear if they exploded at $z = 1$ (see Fig. 18)[203]. They found that these bursts would appear closer to bright short/hard bursts rather than typical long bursts, complicating the classification scheme further. In the end, classifying any particular burst as Type I or Type II is no easy task (see Fig. 19). One must not only consider burst duration and hardness, but also host galaxy properties, SN association (or lack thereof) as well as the medium the burst may be surrounded by. Until a more robust separator of bursts is found, integrating all of the observational evidence is what is needed to make a classification determination or to determine that a classification can not be made.

According to the work of Virgili et al. 2011[178], who sought to use Monte Carlo simulations to try to reproduce the observed population of GRBs, the merger scenario is not sufficient to explain the observed population of short GRBs. Using different cosmological models of NS-NS progenitors populations (e.g. how long it takes NS-NS pairs to merge, assuming that they may have more than one channel for merging) and combining that with what a detector with limited capability of seeing different energy ranges, folded with how these bursts would appear and how many would happen as a function of redshift, this group found that it was impossible to reproduce the observed Log N-Log P distribution of short bursts without introducing "mixing"[178]. Log-N-Log P plots are made by summing the number of bursts with peak energy above a certain value, creating a cumulative distribution plot. Mixing means that the population of short bursts that we are ob-

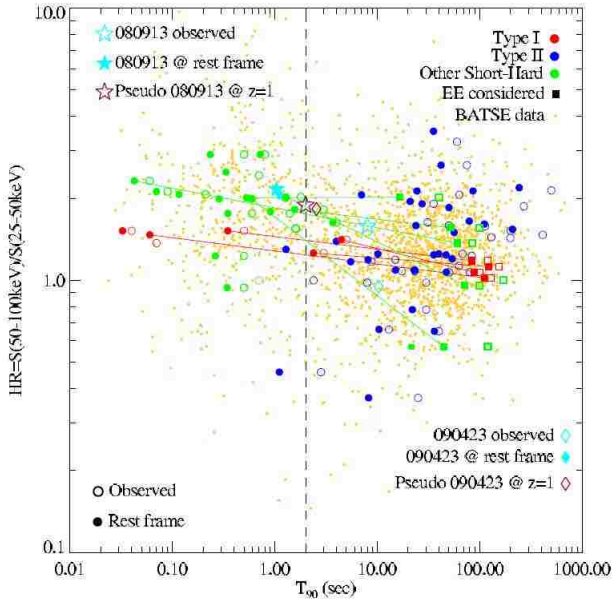

Figure 18 Pseudobursts obtained by placing GRB 080913 (star) and GRB 090423 (diamond) at $z = 1$ show they may be difficult to classify as typical long bursts if seen at a closer redshift. Source:[203].

serving seems to be polluted by up to a large percentage by bursts that are actually of Type II origin but appear to be "short" [178].

In general, it is not easy to try to go from the observed properties of a burst back to what the progenitor must be. In order to properly account for all the evidence, it is necessary to follow a long chain of logic, including properties of the burst such as redshift, host galaxy, burst environment added to the original parameters of duration and hardness ratio before one can come to a tenuous conclusion about the progenitor of the burst.

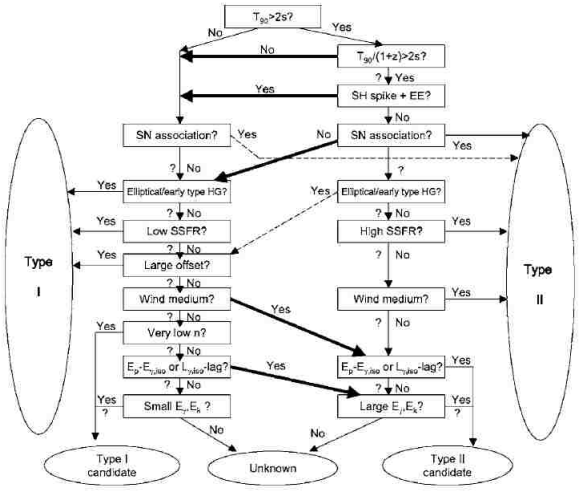

Figure 19 A flowchart recommending how to classify any particular GRB based on its observed properties. Source:[203].

PART II

THEORETICAL FRAMEWORK

CHAPTER 4

RELATIVISTIC EFFECTS

We have seen that relativistic effects were used to find a way out of the compactness problem. The challenge of GRB physics is that, because of the relativistic speeds involved, one must be careful to take the effects of relativity (especially special relativity) into account.

Beaming and Jets

The radiation from an source expanding at relativistic speeds is beamed in the sense that we an only see radiation from within the "light-cone" or from within an angle of $1/\Gamma$ of the line of sight (see Fig. 6). If the source has radius R, the observer will see only a region of size R/Γ. The Lorentz factor of GRB ejecta is presumed to be large, indicating that we are only seeing a very small fraction of the emitting region. If this region is inhomogeneous, we may not be seeing a representative sample of it. As the GRB ejecta plows into the ambient medium, it will slow down like a snow plow collecting snow. As the region expands and the ejecta slows, a larger and larger portion of it will be available to the observer and therefore a more averaged sample of the emitting region will be seen as time goes by. This implies that two observers of the same GRB may observe the initial or prompt radiation differently depending upon their viewing angles. What appears to be an energetic burst at one viewing angle may look like a weak burst at another angle[142]. If GRBs are indeed similar events, then this implies that fluctuations among bursts should be large at early times (i.e. during the prompt phase), but may be more uniform later (i.e. during the afterglow). Further, since brighter or more energetic events are more likely to be detected, if GRBs are inhomogeneous, we may be led

to believe that these events are more representative of the population than they actually are[93][142].

Further, a spherically expanding shell of radiating matter will not appear spherical to a distant observer. The photons from a shell expanding with Lorentz factor Γ that will arrive at the observer at the same time come from an equal-arrival time surface which is an ellipsoid (see Fig.20)[123]. Photons that arrive from the line of sight were released at a larger radius than those arriving from some elevation angle with respect to the line of sight. These photons were generated at a larger radius and therefore within weaker magnetic field (magnetic field should decrease with distance from the CE) and lower density region. Radiation along the line of sight will therefore be softer and less intense than radiation near the edge of the the $1/\Gamma$ cone. Thus the radiation the observer sees appears as a hard ring surrounding a softer core; the effect is called limb-brightening [180].

If the ejecta is not spherically expanding, but instead beamed into a jet of opening angle θ_j and solid angle $\Omega_j \simeq \pi\theta_j^2$, the above prescription still applies provided the observer can not see outside of the jet, i.e. the line of sight to the observer is still within θ_j and $\Gamma \geq \Omega_j^{-1/2}$ which ensures that the light cone is within the jet boundary[121]. As the ejecta slows down to $\Gamma \approx 1/\theta_j$ an observer that is on-axis will see a "jet-break" due to the edge of the jet finally being detected[152][153][160]. On the other hand, observers who were not on axis may see an "orphan afterglow" or an afterglow without preceding GRB emission[64]. It has been suggested that looking through the Sloan Digital Sky Survey data may uncover some of these afterglows[130] but none have yet been found.

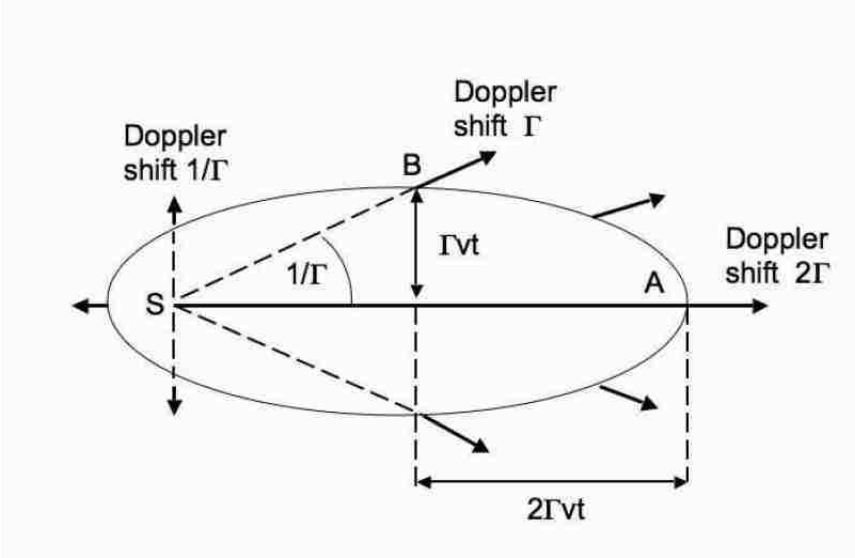

Figure 20 A distant observer will observe a relativistically expanding spherical shell as a ellipsoid of light with equal arrival times. Source:[123]

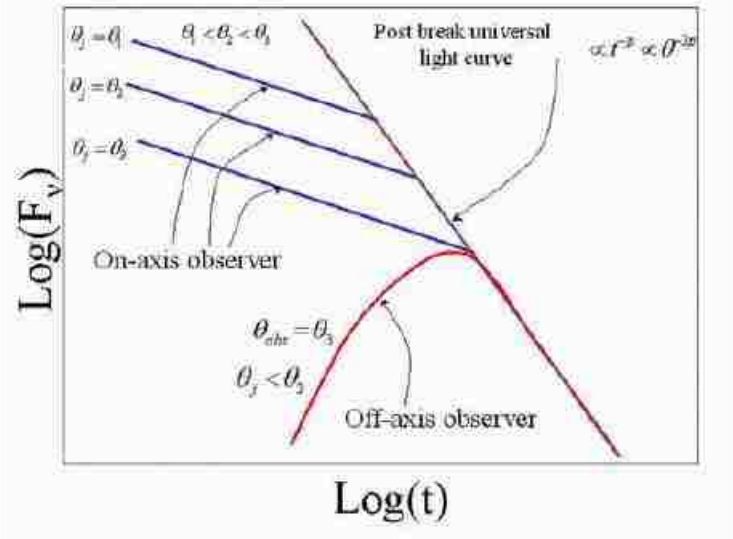

Figure 21 For different viewing angles, an observer sees different amounts of the lightcurve. Source:[142]

Frames

A GRB event has three frames of reference, the CE frame, the observer frame and the frame moving along with the relativistic ejecta (comoving frame). The CE frame and observer frame need only cosmological factors between them. Quantities in the comoving frame and the CE or observer frame, such as length and time will be different and are related to each other through the physics of special relativity. For example, lengths in the comoving frame L' are shortened in the observer frame by a factor of Γ, the Lorentz factor of the ejecta so that $\hat{L} = L'/\Gamma$. Similarly, time intervals are dilated by a factor of Γ between the two frames $\hat{dt} = \Gamma dt'$. In Fig. 22, the geometric configuration of the CE, observer and comoving ejecta are shown, which sets up yet another effect–the propagation effect[199]. Consider the time difference between two photons ejected at the two points in this figure at times $\hat{t_1}$ and $\hat{t_2}$ in the comoving frame. The time interval in the comoving frame will simply be $\hat{dt} = \hat{t_2} - \hat{t_1}$. As the emitting shell expands outward at speed $c\beta$, the first photon, emitted at $\hat{t_1}$, travels a distance ℓ to get to the observer and arrives at time $t_1 = \hat{t_1} + \ell/c$. The emitting region then moves through a distance $\beta c\hat{dt}$ before the second photon is emitted at time $\hat{t_2}$. This photon travels a distance $\ell - \beta c\hat{dt}\cos\theta$ to get to the observer (a shorter distance to the observer than the first photon) so that it arrives at time $t_2 = \hat{t_2} + \ell/c - \beta\cos\theta\hat{dt}$[199]. So in the observer frame:

$$dt = \hat{dt}\,(1 + \beta\cos\theta) \simeq \frac{\hat{dt}}{2\Gamma^2} \tag{4.1}$$

since

$$\Gamma^2 = \frac{1}{1-\beta^2} = \frac{1}{(1+\beta)(1-\beta)} \simeq \frac{1}{2(1-\beta)}. \tag{4.2}$$

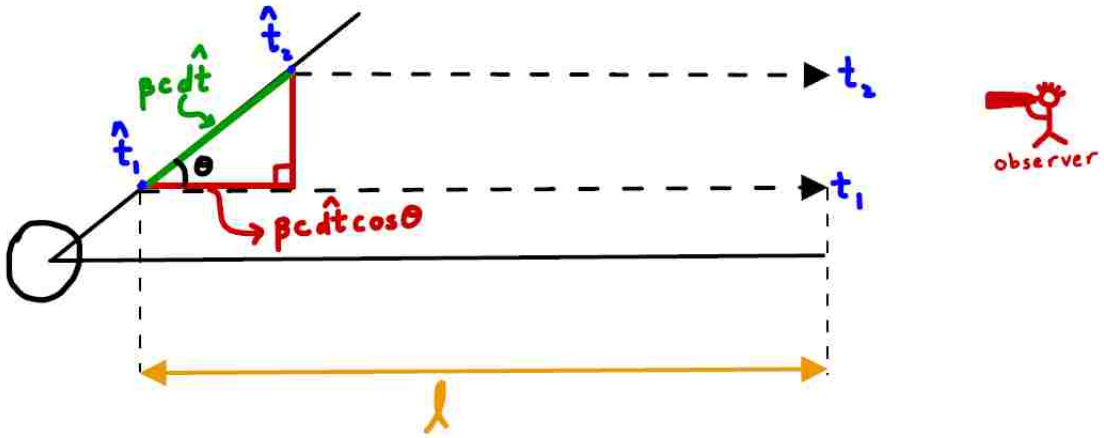

Figure 22 Geometric configuration of the CE, moving ejecta and the observer[199].

The propagation effect is not due to a relativistic effect and would be written the same for a shell moving at Newtonian speeds, however, the effect would be small since $\hat{dt} \simeq dt$[199]. Let us consider again the compactness problem, which was above claimed to be solved by relativistic effects, but in more detail. There are two ways in which relativistic effects help this problem. First, the photons that the observer sees will be blue-shifted since the radiating region is moving towards the observer. After one photon wavefront has arrived at the observer, the next crest is one wavelength $\lambda = c/f'$ away. A photon emitted at the source moves towards the observer with velocity $v = \beta c$ so that the time until the next crest is

$$t' = \frac{\lambda}{c - v} = \frac{c}{(c - v)f'} = \frac{1}{(1 - \beta)f'} \tag{4.3}$$

since the photon moves towards the observer with speed c, but the source moves toward the observer with speed v. Due to time dilation, the observed time is $\hat{t} =$

t'/Γ so

$$\hat{f} = \frac{1}{\hat{t}} = \Gamma(1-\beta)f' \simeq \frac{1}{2\Gamma}f' \tag{4.4}$$

again using the approximation of Eqn. 4.2 above. So that the gamma-rays observed on the Earth may have only been emitted X-rays in the comoving frame. The number of pair producing photons above the threshold would therefore be greatly reduced. A further effect involves the observed variability timescale (δt) which is reduced by a factor of Γ^2 as described above. Altogether, the pair production optical depth can drop significantly[199].

CHAPTER 5

PHYSICAL PROCESSES

Shocks

GRB emission is thought to be the product of both internal and external shocks (see Fig. 23). Internal shocks are the collisions between shells of matter with different Lorentz factors and can happen when when a faster shell released from the CE later catches up to a slower shell, colliding and combining with it and releasing energy in the process. Internal shocks from the collision of many randomized shells are thought to be responsible for both the prompt emission and for X-ray flares, which are wide spikes of emission superimposed on the regular decaying lightcurve (see next part for a thorough description). On the other hand, external shocks are the interaction of a relativistic shell of matter with the ambient medium or ISM. As a shell plows into the cold ISM, regular decaying lightcurves are predicted with flux varying from gamma-rays to X-rays to optical to radio.

The kinetic energy of a relativistically moving shell could be turned into the radiation we see via shocks which are expected in GRBs considering we see a similar phenomenon when looking at SN remnants[149]. Consider a cold shell of matter overtaking another cold shell or the inter-stellar medium (ISM) ("cold" simply means that the internal energy of the shell is small compared to the rest mass energy of the shell). This problem is divided into four regions of interest (see Fig. 24):

- 4. Unshocked relativistic shell of matter moving with Lorentz factor Γ with respect to the ISM.
- 3. Shocked shell material which has passed through the reverse shock.
- 2. Shocked ISM material that has passed through the forward shock.

- 1. The ISM region at rest.

The quantites Γ, and $f \equiv n_4/n_1$ or the fraction of number density of particles in the ISM to that in the shell are the physical quantities which determine the strength of the shocks. Initially this density contrast is large as at first the shell is dense so that $n_4/n_1 > \Gamma^2$. In the beginning stage, the reverse shock is "Newtonian" or only mildly relativistic and the energy conversion is concentrated in the forward shock[159][142][141]. If Γ_2 is the Lorentz factor of the shocked fluid relative to the rest frame of the ISM and $\bar{\Gamma}_3$ be the Lorentz factor of the the shocked fluid relative to the rest frame of the relativistic shell in region 4, then $\Gamma_2 \approx \Gamma$ and $\bar{\Gamma}_3 \approx 1$. The shock equations between regions 1 and 2 yield[142]:

$$n_2 \approx 4\Gamma n_1 \tag{5.1}$$

$$e \equiv e_2 = 4\Gamma^2 n_1 m_p c^2 \tag{5.2}$$

$$n_3 = 7n_4 \tag{5.3}$$

$$e_3 = e. \tag{5.4}$$

Where e_i represents the energy density in region "i". After the shell expands and the density decreases (as $1/R^2$ for a spherically expanding shell or $1/R^3$ if shell spreading is included), eventually the reverse shock can move into the relativistic regime (so $n_4/n_1 < \Gamma^2$ now but $n_4/n_1 > 1$). The forward shock is still relativistic and the shock equations combined with equating pressure and velocity at the contact discontinuity yield[142]:

$$\Gamma_2 = \left(\frac{n_4}{n_1}\right)^{1/4} \frac{\Gamma^{1/2}}{\sqrt{2}} \tag{5.5}$$

$$n_2 = 4\Gamma_2 n_1 \tag{5.6}$$

$$e \equiv e_2 = 4\Gamma_2^2 n_1 m_p c^2 \tag{5.7}$$

and for the reverse shock:

$$\Gamma_3 = \left(\frac{n_4}{n_1}\right)^{-1/4} \frac{\Gamma^{1/2}}{\sqrt{2}} \tag{5.8}$$

$$n_3 = 4\bar{\Gamma}_3 n_4 \tag{5.9}$$

$$e_3 = e \tag{5.10}$$

$$\bar{\Gamma}_3 \approx \left(\frac{\Gamma}{\Gamma_2} + \frac{\Gamma_2}{\Gamma}\right)/2. \tag{5.11}$$

The forward and reverse shock release comparable amounts of energy when both are relativistic and the kinetic energy released is thought to be converted to the radiation we see via synchrotron radiation mechanisms.

Synchrotron Radiation

Synchrotron emission is caused by relativistic electrons gyrating (and hence changing velocity) in a magnetic field. Synchrotron emission produces a non-thermal power-law spectrum and so is a particularly attractive candidate for emission from GRBs. In order to calculate the flux radiated via synchrotron radiation, a few source parameters must be assumed. First, only some (typically assumed small)fraction of the total number electrons present in the ejected plasma will be Fermi accelerated in the shock wave. These electrons carry a total amount of energy that is a fraction, ϵ_e of the total energy contained in the shocked region. These accelerated electrons are assumed to have a power-law distribution of energies with index p or $N(E)dNE/dE \propto E^{-p}$. Second, the energy density of the magnetic field in this region $B^2/(8\pi)$ is also some fraction of the total energy contained in

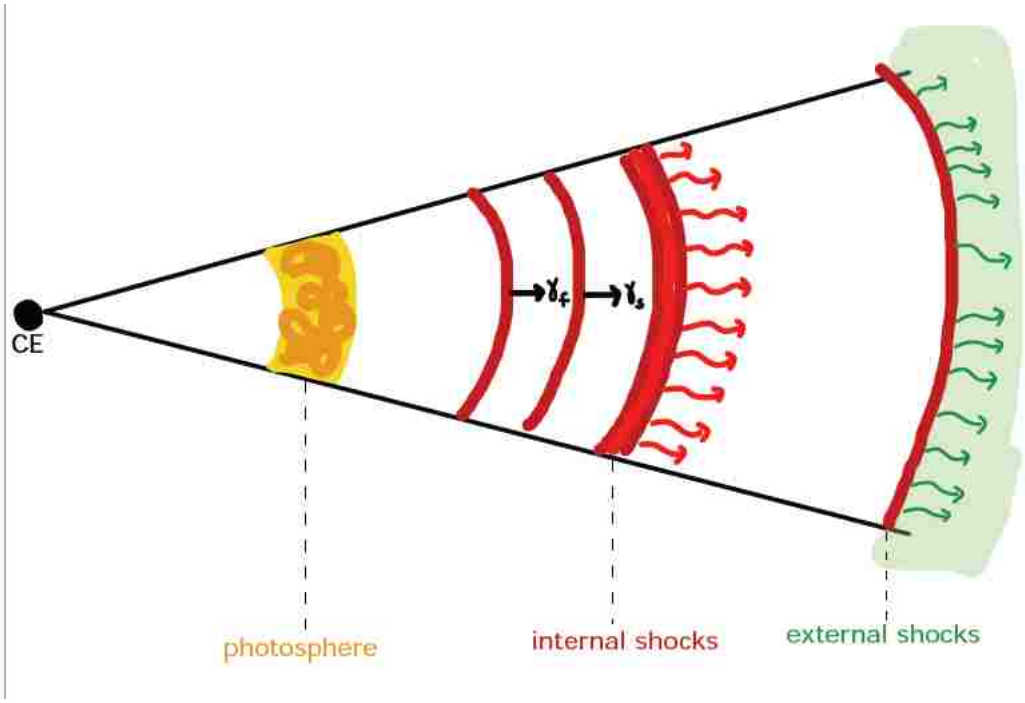

Figure 23 Cartoon Model of a GRB[199].

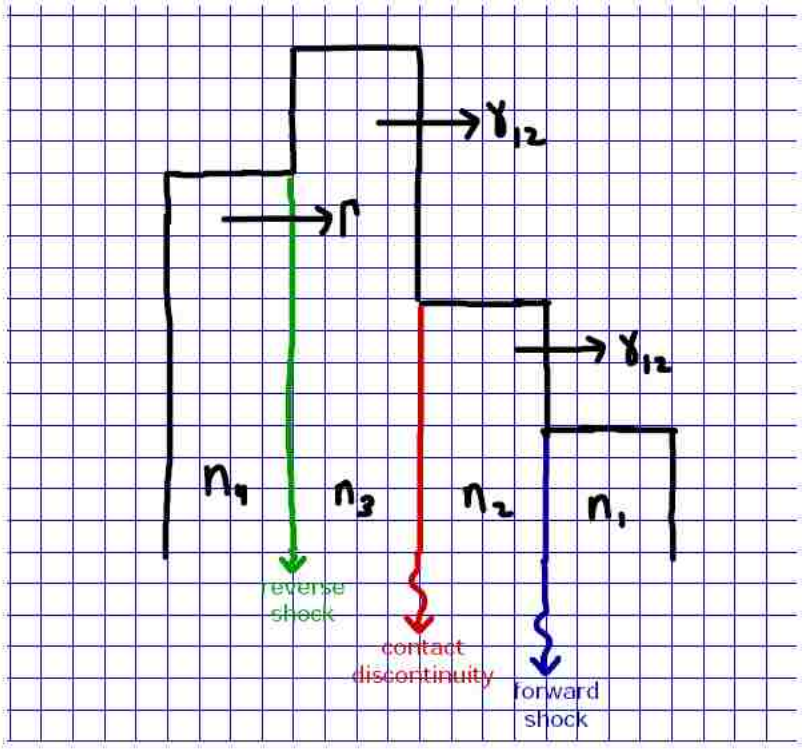

Figure 24 The regions of a shock [141][142].

the shocked region, ϵ_B [199][136].

The radiation power of synchrotron radiation for electrons moving with speed γ_e in a shock front moving with speed γ is [161]:

$$P(\gamma_e) = \frac{4}{3}\sigma_T c\gamma^2\gamma_e^2\frac{B^2}{8\pi} \tag{5.12}$$

The electrons move with a characteristic frequency of [161]

$$\nu(\gamma_e) = \gamma\gamma_e^2\frac{q_e B}{2\pi m_e c} \tag{5.13}$$

The peak spectral power is independent of γ_e and is given by[161]:

$$P_{\nu,max} \approx \frac{m_e c^2\sigma_T}{3q_e}\gamma B \tag{5.14}$$

where t is the time in the observer frame. This power is only valid if the electrons have not lost a significant amount of energy to radiation or when γ_e is less than some critical value γ_c given by $\gamma\gamma_c m_e c^2 = P(\gamma_c)t$. Electrons with Lorentz factor above the critical value will cool to the critical value in time t. There will be two different types of cooling, depending upon whether the minimum Lorentz factor of the electrons γ_m is above or below the critical Lorentz factor γ_c. In the first case, $\gamma_m > \gamma_c$ allowing all of the electrons to cool down to γ_c; this is the fast cooling case. The flux is given by:

$$F_\nu = \begin{cases} (\nu/\nu_c)^{1/3} F_{\nu,max} & \nu_c \geq \nu \\ (\nu/\nu_c)^{-1/2} F_{\nu,max} & \nu_m \geq \nu \geq \nu_c \\ (\nu_m/\nu_c)^{-1/2} (\nu/\nu_m)^{-p/2} F_{\nu,max} & \nu \geq \nu_m \end{cases} \tag{5.15}$$

On the other hand, if $\gamma_m < \gamma_c$, only the electrons with Lorentz factors above γ_c can cool. This is called the slow cooling case

$$F_\nu = \begin{cases} (\nu/\nu_m)^{1/3} F_{\nu,max} & \nu_m \geq \nu \\ (\nu/\nu_m)^{-(p-1)/2} F_{\nu,max} & \nu_c \geq \nu \geq \nu_m \\ (\nu_c/\nu_m)^{-(p-1)/2} (\nu/\nu_c)^{-p/2} F_{\nu,max} & \nu \geq \nu_c \end{cases} \tag{5.16}$$

using the minimum Lorentz factor of the electrons

$$\gamma_m = \epsilon_e \left(\frac{p-2}{p-1}\right) \frac{m_p}{m_e} \gamma, \tag{5.17}$$

the comoving magnetic field strength

$$B = (32\pi m_p \epsilon_B n)^{1/2} \gamma c, \tag{5.18}$$

and the cooling Lorentz factor of electrons

$$\gamma_c = \frac{6\pi m_e c}{\sigma_T B^2 \gamma t} \simeq \frac{6\pi m_e \gamma c^2}{\sigma_T B^2 R}, \tag{5.19}$$

one can calculate the critical synchrotron frequencies ν_m and ν_c using

$$\nu(\gamma_e) = \gamma \gamma_e^2 \frac{q_e B}{2\pi m_e c}, \tag{5.20}$$

where m_p, m_e, σ_T and q_e are the proton mass, electron mass, fundamental charge and Thompson cross-section, respectively. Combining this with

$$F_{\nu,max} = \frac{m_e c^2 \sigma_T}{3 q_e} \gamma n B R^3 \frac{\nu}{4\pi D^2}, \tag{5.21}$$

where D is the distance from the observer,ν is the frequency in the band you are observing.[161]. Standard values for $p = 2.4$, $\epsilon_e = 0.1$, $\epsilon_B = 0.01$, $n = 1$ ([136]) can be used to calculate the flux. Typical fast and slow cooling flux curves are shown in Fig. 25.

Canonical X-Ray Lightcurve

As the number of lightcurves detected in the X-ray band increased to over 400 due to the Swift telescope, a general picture began to emerge of the canonical X-ray afterglow behavior (see Fig. 26))[132][194]. Although not all pieces of this curve are seen in all GRBs, many of the pieces have theoretical models to describe them.

- 0: *The prompt emission.* Probably produced by internal shocks as the CE released many randomizes shells of matter which can collide, producing the spiky prompt emission.

- I: *The steep decay phase.* The generally assumed picture of this phase is that of "tail emission" due the curvature effect[46][91][194]. If the CE was to turn off suddenly, then radiation seen from this last ejected radiating spherical shell would be seem to decay sharply as the observer saw radiation from higher and higher latitudes which take slightly longer to reach us (similar geometry to the propagation effect). This effect gives a simple prediction, that $\alpha = 2+\beta$, or the powerlaw slopes connecting this decay phase to the one before should be related. Being careful to reset the CE clock to the proper t_0 so as not to introduce artificial plotting effects in log space, this prediction is satisfied for many bursts[107].

- II: *Shallow decay phase.* This phase is still a mystery, but what is sure that the spectral index across the break does not change from the shallow to nor-

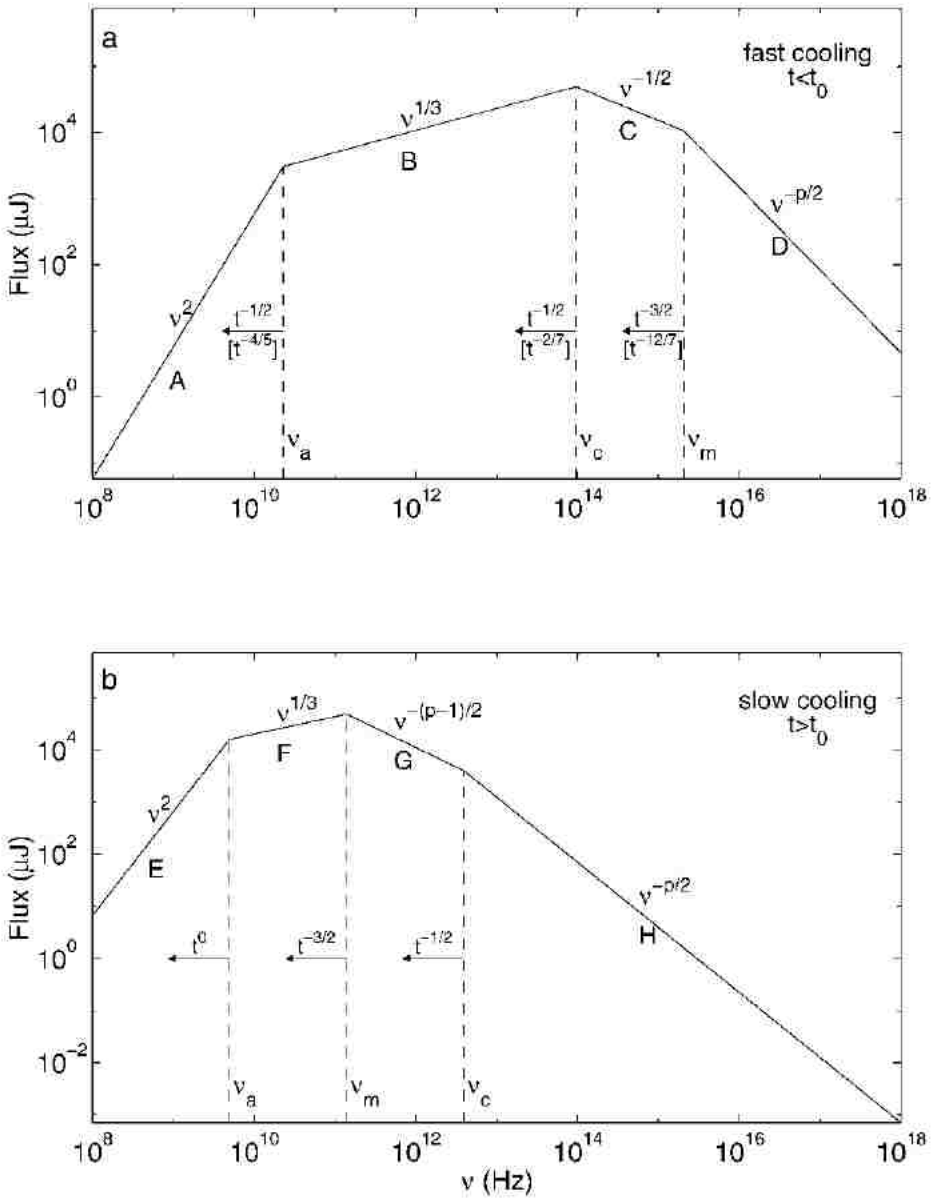

Figure 25 Synchrotron spectrum a relativistic shock for the fast and slow cooling cases Source:[161].

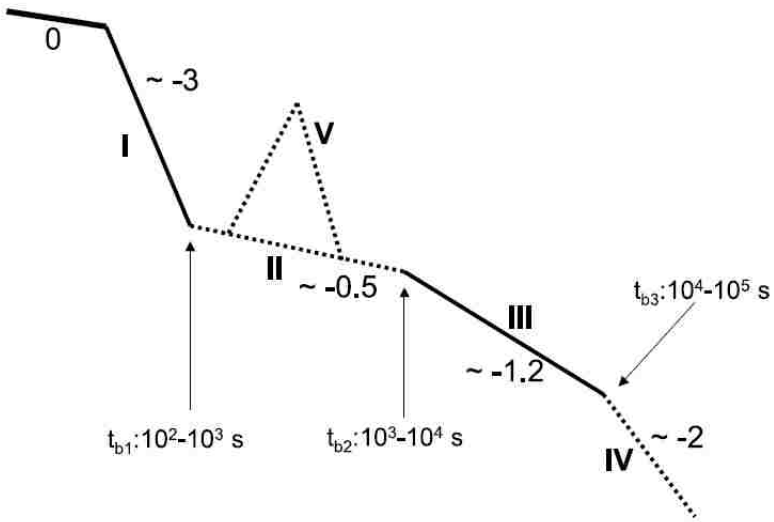

Figure 26 Canonical X-ray light curve. Source:[194].

mal decay phase, so any theory that explains this phase can not be based on models that have a spectral break. One interpretation is that the energy in the external shock is increasing with time producing a shallower than normal decay phase. This energy injection could be due to a long lasting central engine[194][132] or due to the spin-down of a CE pulsar [35][196]

- III: *Normal decay phase.*This phase was expected in the pre-Swift era and is explained by the synchrotron emission of a relativistic blastwave plowing into the ISM.

- IV: *Post jet break phase.*The break between the normal decay phase and the post jet break phase is thought to be due to the so-called "jet break". This break is required if we believe that GRBs are indeed beamed. Any observer can initially only see the radiation beamed into the angle $1/\Gamma$. This beam-

ing angle is physically unrelated to the angle of opening of the jet θ_j but as the beaming angle grows as the ejecta slows, $1/\Gamma \approx \theta_j$ this means that areas of the jet that were outside of the beaming will come into causal contact with the jet, causing sideways expansion and a sudden decline in afterglow emission[153][160].

- V: *X-ray flares.* X-ray flares appear in nearly half of GRBs and the number seen in any particular burst varies from one to several[29]. Superimposed on the regular afterglow decay, they can appear on top of any of the phases I,II, III or IV. They are thought to represent internal shocks due to late CE activity[114] (see then next part for a discussion of X-ray flares in detail).

Blastwave Solutions

[1] As the first shell moves outward into the ambient medium, it slows down due to an external shock mechanism as it sweeps up the ambient medium. As time goes by, more and more trailing shells collide onto the leading decelerating shell. The motion of this decelerating ejecta along with the medium collected along the way, known as the "blastwave", is governed by the following differential equations[28][71]:

$$\frac{dR}{dt} = \beta c = \frac{\sqrt{\gamma^2 - 1}}{\gamma} c, \tag{5.22}$$

$$\frac{d\gamma}{dm} = \frac{-(\gamma^2 - 1)}{M}, \tag{5.23}$$

$$\frac{dm}{dR} = 4\pi R^2 \rho. \tag{5.24}$$

[1]The content of this section is drawn from Maxham & Zhang (2009)[114] and Maxham, Zhang & Zhang (2011)[115]

Here t is the time in the rest frame of the central engine, R is the distance from the central engine, ρ is the density of the ambient medium, γ is the Lorentz factor of the shell, m is the swept-up mass, and $M = M_0 + \gamma m$ is the total mass including internal energy of the blast wave, where M_0 is the initial mass of the ejecta. As a result, one has another differential equation,

$$\frac{dm}{dM} = \frac{1}{(1-\epsilon)\gamma + \epsilon}\,, \tag{5.25}$$

where the value of $0 \leq \epsilon \leq 1$ determines the efficiency of the radiation, with 0 representing the purely adiabatic case and 1 representing the fully radiative condition. Equation (5.22) simply states how radius changes as a function of time for an object moving with constant velocity. Equation (5.23) is a statement of conservation of energy and momentum across the blast wave[12]. Although these expressions are valid only when the blast wave is in the relativistic regime, they are adequate for our calculation, since X-ray flares usually happen early before the blast wave enters the trans-relativistic regime. The amount of swept up mass in shell of surface area $4\pi R^2$ is described by equation (5.24)[2]. The solution of this system is found to be

$$\gamma = \sqrt{\frac{16\pi^2\rho R^6 + 24\pi\rho(M_0\gamma_0)R^3 + 9(M_0\gamma_0)^2}{16\pi^2\rho R^6 + 24\pi\rho(M_0\gamma_0)R^3 + 9M_0^2}}. \tag{5.26}$$

for the fully adiabatic case ($\epsilon = 0$) and was first presented in Maxham & Zhang (2009)[114]. The solution for the fully radiative case ($\epsilon = 1$) is found to be:

$$\gamma = \frac{9(M_0\gamma_0)^2 + 12\pi\rho M_0 R^3(1+\gamma_0) + 8\pi^2\rho^2 R^6(1+\gamma_0)}{9M_0^2 + 12\pi\rho M_0 R^3(1+\gamma_0) + 8\pi^2\rho^2 R^6(1+\gamma_0)}. \tag{5.27}$$

[2]The treatment here is based on the assumption of an isotropic ejecta. The treatment is valid before the "jet break" time, which is usually the case for X-ray flare observations. After the jet break time, the dynamics may be altered by sideways expansion of the ejecta. However, numerical simulations suggest that such an expansion is not important [90][26][195]. For simplicity, we take the isotropic assumption throughout the blast wave evolution.

and was first presented in Maxham, Zhang & Zhang (2011)[115].

The leading shell initially expands freely until the momentum of the swept up matter is about equal to the initial mass of the shell, M_0. The radius of deceleration, R_d, is found from $\gamma_0 \frac{4}{3}\pi R_d^3 \rho \approx M_0$, where the subscript "0" represents initial values[149]. For typical values of $\gamma_0 \sim 100$, $M_0 \sim 10^{28}$g and $\rho \sim 2 \times 10^{-24} \mathrm{g\ cm^{-3}}$, one has $R_d \sim 2 \times 10^{16}$cm.

The relativistic blast wave decays as $\gamma \propto R^{-3/2}$, until reaching the Sedov radius, at which the rest mass of the ambient medium becomes as large as the rest mass of the blast wave, i.e. $R_{Sedov} = (3M_0/4\pi\rho)^{1/3}$. After this point, the expansion enters the non-relativistic regime with dimensionless velocity $\beta \propto R^{-3/5}$[165].

PART III

SIMULATIONS

CHAPTER 6

SHELL MODEL CODE

[1] We have developed a shell model code to address various problems in GRB physics. Written in Mathematica 6.0 and upgraded to 7.0. Our model represents the GRB central engine as a variable source that ejects many randomized shells of matter over some period of time. Shells ejected later with higher Lorentz factors catch up with slower shells, colliding and creating "internal shocks"[150]. As the modeled shells move outward from the central engine, the energy released from each collision is calculated, allowing the two colliding shells to combine and continue to move outward to collide with other shells. The code generates N shells and each shell is given four parameters: Lorentz factor (γ), mass (m), width (Δ) and ejection time (t_{ej}). The user can choose N and define the parameters for each sell created, either by randomly generating them (using any distribution and range) or by inputting the values for each shell by hand. The first shell that is ejected is the blastwave and this shell plows into the ambient medium, following the motion prescribed in the previous chapter. As the blastwave moves outward, later ejected shells may pile onto it, increasing its energy. Before these shells combine with the blastwave, they may experience "internal shocks", or the collision between two of these matter shells. Since these shells move into a relative void, they move with a constant relativistic velocity ($r = vt$)so the radius and time of any given collision (in the CE frame) is a matter of geometry–or the intersection of two straight lines. The goal of the code is to address issues of GRB prompt emission and X-ray flares within the internal shock model, mainly the energy released, efficiency and timing of pulses.

[1]The content of this chapter is drawn from Maxham & Zhang (2009)[114]

Two-Shell Interaction

We assume that shell collisions are inelastic, so that a fast shell (f) and a slow shell (s) merge to form a merged shell (m) (see Fig. 27). Using conservation of momentum and energy, the Lorentz factor of the combined shell can be written

$$\gamma_m \simeq \sqrt{\frac{\gamma_f m_f + \gamma_s m_s}{\frac{m_f}{\gamma_f} + \frac{m_s}{\gamma_s}}}. \tag{6.1}$$

Each collision then releases an internal energy given by (Kobayashi et al. 1997)

$$E_{int} = (\gamma_f - \gamma_m) m_f c^2 + (\gamma_s - \gamma_m) m_s c^2. \tag{6.2}$$

The efficiency of each collision can be defined as

$$\eta = \frac{E_{int}}{(\gamma_s m_s c^2 + \gamma_f m_f c^2)} \, . \tag{6.3}$$

It has been known that this efficiency is usually low ([87][137]) although depending on input parameters, it can vary in a wide range. To test this, we simulated 100 shells that are randomly injected during 0-100 s. We allow the mass of each shell to be randomly drawn in the range of $10^{29} - 10^{31}$ g in log space, and investigate how Lorentz factor contrast affects the distribution of the efficiency. We randomly generate shell Lorentz factors in log space within a range of $(\gamma_{min}, \gamma_{max})$. Table 3 shows the mean efficiency of η and its standard deviation σ for varying $\gamma_{max}/\gamma_{min}$. It is evident that the mean value of η rises steadily with $\gamma_{max}/\gamma_{min}$. However, even for a very high Lorentz factor contrast $\gamma_{max}/\gamma_{min}$ = 1000, the mean efficiency still only reaches a level of $\sim$ 26%. Values of σ are on the order of η, which means that very low and very high η can be expected for extreme parameters of the two

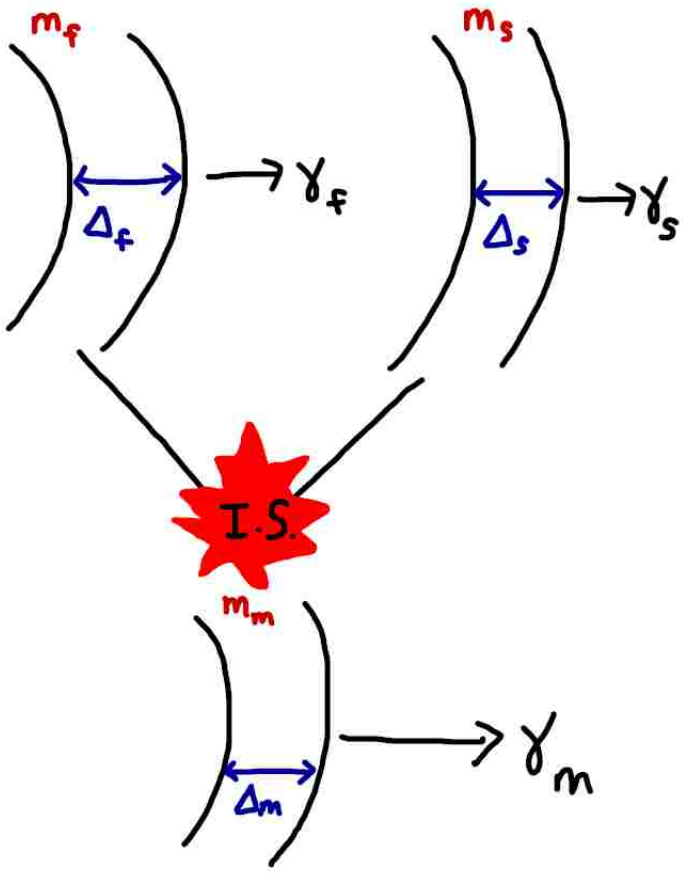

Figure 27 Two shells collide and combine, releasing energy.

Table 3 Efficiency and standard deviation for energy conversion in the internal shock model.

$\gamma_{max}/\gamma_{min}$	η	σ	$\gamma_{max}/\gamma_{min}$	η	σ
variable masses			even masses		
1000	26%	26%	1000	28%	27%
100	14%	17%	100	19%	20%
10	5%	7%	10	7%	8%
5	0.5%	0.7%	5	0.6%	0.9%

shells. The right pane of Table 3 shows the efficiency for the same simulation, but with shell masses standardized to all be 10^{30} g. These results are on order with the efficiency study with varying shell masses. For our model, we do not follow the internal shock physics in detail. This has been done by Yu & Dai (2009) [189], who showed that for reasonable parameters, the emission from internal shocks can well reproduce the X-ray flare phenomenology. Our goal is to model many collisions and to investigate the time history of central engine activity, collision, and GRB emission. Like many other previous work in this direction (e.g. [81] [137]), we adopt an empirical approach to calculate the spectrum and lightcurve of each collision event.

Spectral Model

The spectrum of GRBs is typically a smoothly-joint-broken-power-law spectrum, or "Band"-function[8]

$$N_E(E) = \begin{cases} A\left(\frac{E}{100\mathrm{keV}}\right)^{\alpha}\exp\left(-\frac{\mathrm{E}}{\mathrm{E_0}}\right) & (\alpha-\beta)E_0 \geq E \\ A\left(\frac{(\alpha-\beta)E_0}{100\mathrm{keV}}\right)^{\alpha-\beta}\exp(\beta-\alpha)\left(\frac{\mathrm{E}}{100\mathrm{keV}}\right)^{\beta} & (\alpha-\beta)E_0 \leq E \end{cases} \tag{6.4}$$

where α and β are the power law photon spectral indices below and above the break energy E_0 in the asymptotic regime, A is a normalization factor. The break energy can be written as $E_0 = E_p/(2+\alpha)$, where E_p is the spectral peak energy in the GRB energy spectrum. Since evidence strongly suggests that GRB prompt emission and X-ray flares originate from similar physical events (e.g. [25][29][42][85]), we assume that the spectrum of X-ray flares is also a Band-function.

The Band-function parameters of X-ray flares are determined in the following way in our calculations: The typical values for the spectral indices are taken as $\alpha = -1$, and $\beta = -2.3$. For E_p, we calculate it through an empirical relation between the isotropic emission energy E_{iso} and E_p, which is generally valid among GRBs ([5][86]) and within a burst[102][60]. We assume the validity of this correlation

$$E_p = 100 \text{ keV} \left(\frac{E_{iso}}{10^{52} \text{ erg}} \right)^{1/2} \tag{6.5}$$

and apply $E_{iso} = E_{int}$ to estimate E_p. This is because electrons in the shock are in the "fast-cooling" regime, and lose their energy rapidly. As long as the electron equipartition parameter ϵ_e is close to unity, essentially all the internal energy can be radiated away. For $\epsilon_e \ll 1$, this estimate gives an upper limit on the brightness of X-ray flares. We require that the spectrum-integrated bolometric energy $\int_0^\infty EN_E(E)dE$ equals E_{int} and then solve for the normalization factor A. Then reinserting this constant, we can calculate the energy of each pulse $\int_{E_1}^{E_2} EN_E(E)dE$ within each band (E_1, E_2), e.g. 15 to 150 keV for BAT, 0.1 to 10 keV for XRT.

Temporal Model

The total energy released in a particular band for a particular pulse is distributed in time throughout the X-ray flare temporal profile. Different functions

of GRB pulses and X-ray flares have been adopted in the literature [81][29], but for the purpose of our study, the shape of the flare profile is not crucial. For simplicity, we adopt the following temporal profile

$$L(t) = L(t_p)e^{\frac{-(t-t_p)^2}{2(\delta t)^2}} \tag{6.6}$$

where the temporal width $\delta t = \Delta/c$ scales as the physical width of the shell, Δ. For a shell with initial width Δ_0 moving outward from the central engine, spreading will occur after the sound wave travels across the shell at $R_s \sim \gamma^2\Delta_0$). So in general, the shell width can be expressed as [121][82])

$$\Delta = \begin{cases} \Delta_0, & R < R_s \\ \frac{R}{\gamma^2}, & R > R_s. \end{cases} \tag{6.7}$$

We require that the temporal integral of the profile $\int_0^\infty L(t)dt$ equals the internal energy in the specified energy band (BAT or XRT). When shells collide, the duration of the X-ray flare pulse is defined by the width of the faster shell. This is because the reverse shock is typically the one that dominates the X-ray flare emission[189]. After the collision, which occurs at R_{col}, the width of the the combined shell is taken to be R_{col}/γ_m^2, i.e. the width in the spreading regime. The width of the shell keeps spreading as R/γ_m^2 thereafter.

In the central engine frame, the shells collide at $t_{col} \simeq R_{col}/c$. The relevant observation time is[2]

$$t_{\oplus,col} = t_{ej} + \frac{(t_{col} - t_{ej})}{2\gamma^2}\,, \tag{6.8}$$

[2]Usually this is called observer frame time. However, the central engine and the observer is in the same inertial frame (with cosmological time dilation correction). The difference between the two times is due to a propagation effect, not Lorentz transformation [199].

where t_{ej} and γ can be taken as the ejection time and Lorentz factor of either of the two colliding shells. The peak time of a flare is defined as the observed collision time plus the observed shock crossing time, which is roughly estimated as

$$t_p \simeq t_{\oplus,col} + \frac{\Delta}{c}. \tag{6.9}$$

CHAPTER 7

MODELING X-RAY FLARES

[1] X-ray afterglow light curves have been collected for over 400 Swift gamma-ray bursts with nearly half of them having X-ray flares superimposed on the regular afterglow decay. Evidence suggests that gamma-ray prompt emission and X-ray flares share a common origin and that at least some flares can only be explained by long-lasting central engine activity. We have developed a shell model code to address the question of how X-ray flares are produced within the framework of the internal shock model. The shell model creates randomized GRB explosions from a central engine with multiple shells and follows those shells as they collide, merge and spread, producing prompt emission and X-ray flares. We pay special attention to the time history of central engine activity, internal shocks, and observed flares, but do not calculate the shock dynamics and radiation processes in detail. Using the empirical $E_p - E_{iso}$ (Amati) relation with an assumed Band function spectrum for each collision and an empirical flare temporal profile, we calculate the gamma-ray (Swift/BAT band) and X-ray (Swift/XRT band) lightcurves for arbitrary central engine activity and compare the model results with the observational data. We show that the observed X-ray flare phenomenology can be explained within the internal shock model. The number, width and occurring time of flares are then used to diagnose the central engine activity, putting constraints on the energy, ejection time, width and number of ejected shells. We find that the observed X-ray flare time history generally reflects the time history of the central engine, which reactivates multiple times after the prompt emission phase with progressively reduced energy. The same shell model predicts an external shock X-ray afterglow component, which has a shallow decay phase due to the initial pile-up of shells onto the

[1] The content of this chapter is drawn from Maxham & Zhang (2009)[114]

blast wave. However, the predicted X-ray afterglow is too bright as compared with the observed flux level, unless ϵ_e is as low as 10^{-3}.

Introduction

The study of gamma-ray bursts (GRBs) has been greatly advanced following the launch of the Swift Gamma-Ray Explorer[56] on November 20, 2004. Thanks to its rapid slewing capability, multi-wavelength observations of GRB afterglows, usually as soon as < 100 seconds after the burst trigger, have been performed regularly for many bursts. The X-ray telescope (XRT, [23]) aboard this satellite has given us unprecedented access to early afterglows in the X-ray band. For most GRBs, XRT has observed smoothly decaying power-law or broken power-law afterglows [132][134][202][106][104][39]. In about half of GRBs, superimposed on the background X-ray afterglow, one or more X-ray flares are seen [24][154][41][42][29].

Flares among the bursts share some common properties, which include the following (see Fig. 28):

- The morphology of flares is similar: they all show a smooth, rapid rise and a rapid fall[154].

- They are superimposed on a background power-law decay afterglow component with the slope before the flaring equal to that after the flare [25].

- The width of flares is typically narrow, with $\delta t/t \sim 1/10$ on average, where t is the emission time of the flare. However, flares can become wider ($\delta t/t$ becomes larger) as the time of their emission increases, and no sharp flares are seen at late times [29][83].

- Similar flaring activity has been detected in both types of GRBs: those be-

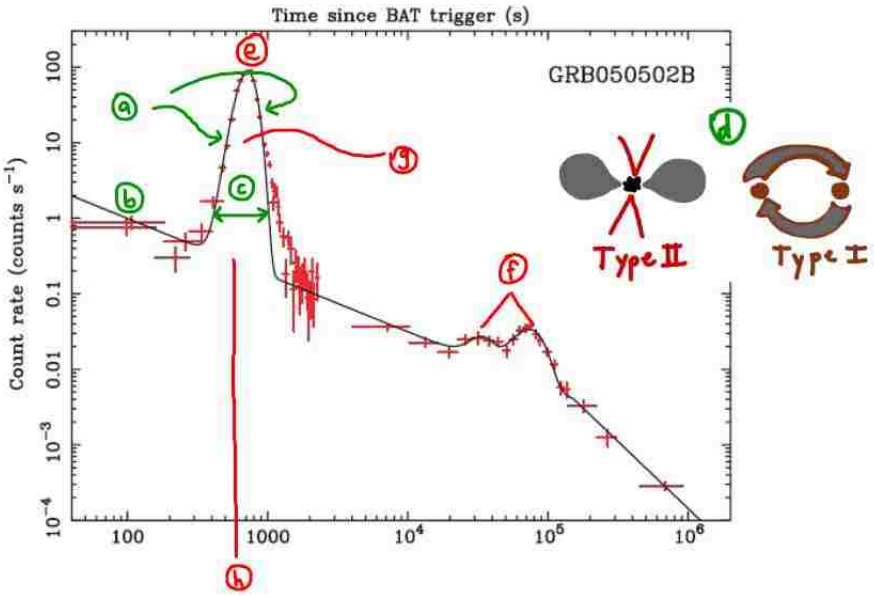

Figure 28 Properties of an X-ray flares are highlighted including similar among flares (in green) (a) Flares show a smooth rapid rise and decay (b)they are superimposed on the background flux (c)the width is $\delta t/t \sim 1/10$ on average and (d)can come from either Type I or Type II bursts. Different among flares (in red) (e)the shape can take on many profiles (f)the number of flares per burst varies (g)the fluence contained in flares varies and (h)the emission time of flares varies.

lieved to be of massive star origin (Type II, typically long duration) and those believed to be of compact star merger origin (Type I, typically short, e.g. in GRB 050724[10] [2]. This suggests that the phenomenon is insensitive to the progenitor type [140].

- Flares are spectrally harder than the underlying afterglow[24][154][41].
- For a small sample of bright flares whose time-dependent spectral analysis can be performed, flares are found to soften as they decay[24][25][41][42], reminiscent of GRB prompt emission.
- Average X-ray flare luminosity decays with time as a power-law with slope $\sim$ -1.5 for a sample of flares from many GRB's. This temporal relationship also seems to hold among flares from a single multi-flared burst [98].

Flares also vary from burst to burst, from flare to flare, in the following ways:

- The shape of flares can be best fit with a number of different profiles: gaussian, log-normal distributions, exponential or power-law rise or decay with differing slopes for both the rising and falling portion of the flare[29].
- The number of flares seen per burst varies from modal value of 1, mean value of $\sim$ 2.5 and maximum value of 8 [29].
- The fluence seen in flares can vary from a few percent of the burst fluence to larger than the burst itself (e.g. for GRB050502B [24][25][41]).
- The emission time of flares varies from perhaps before the slew of XRT (e.g. GRB060607) to late flares at 10^4 seconds (e.g. GRB050904[34]) to 10^5 seconds (for the Type I GRB050724 [10]). Some flares are superimposed on other flares

[2]For a full discussion of the two physically distinct types of GRBs, see [204].

(e.g. GRB050916 [24][25][29]). Although most flares happen early, from 100 to 1000 seconds, the distribution of t tails off to 10^6 seconds[29].

A few properties of X-ray flares suggest that they are connected to internal emission processes due to a restarting of the central engine at late times[24][41][154][191]. The arguments in favor of such a "late internal" model (in contrast to the external shock model) are the following: First, the rapid rise and fall of flares with $\delta t/t \sim 1/10$ strongly disfavors external shock models that involve a large angular area over which radiation would be emitted[194] (see also [73][43][97]. Second, the connected, underlying continuum which has the same slope both before and after the flare suggests that flares are not related to the canonical afterglow and are instead superimposed on top of this regular afterglow decay[29]. Third, given the same observed X-ray flare amplitude, the internal model requires a much smaller energy budget than the external shock model [194]. While the internal model can produce significant X-ray flares with energy much less than that during the prompt emission, the external shock model requires an energy budget at least comparable to that of the initial blast wave in order to make a noticeable change in flux [197]. Internal models are much more "economical" as far as energy budget is concerned. Next, Liang et al. (2006) [107] have shown that as long as the central engine clock is reset to zero at the beginning of each flaring episode, the curvature effect can naturally explain the spectral index and the temporal decay index of the decay phase of flares. Finally, although there is no correlation between the number of prompt emission burst pulses and X-ray flares in any given burst[29], X-ray flares do exhibit the same spectral softening as GRB prompt emission [24][25][41][42]. This suggests that the properties of X-ray flares make them likely to be caused by the same mechanism as prompt emission seen in gamma-rays.

Any X-ray flare model must be able to explain the bulk similarities and differ-

ences among flares enumerated above. The leading "internal" model is the internal shock model [150], which invokes internal collisions of shells within an unsteady central engine wind. Previous internal shock models have focused on interpreting prompt gamma-ray emission properties (e.g. [81][137][168][68]). Kobayashi et al. (1997)[81] have shown that internal shocks can explain the highly variable profiles seen in GRBs. In their model, shells of matter with varying Lorentz factors ejected from the central engine produce about as many collisions as the number of shells, and the time of ejection of the shell is highly correlated to the time of collision of the shells, indicating that there is essentially no delay between energy ejection by central engine emission and the time when that emission is seen. Recently, using a model where collisions are not perfectly inelastic, Li & Waxman (2008)[101] studied the effect of residual collisions in optical emission which would be slightly delayed from gamma-ray prompt emission.

Within the context of X-ray flares, the internal shock model has been discussed by a number of authors. Zhang et al. (2006)[194] and Fan & Wei (2005)[43] discussed how a late internal shock may produce a softer flare than prompt gamma-ray emission. Wu et al. (2005)[185] discussed both late internal and external shock models to study X-ray flares and concluded that at least some flares have to be produced by late internal shocks. Lazzati & Perna (2007)[97] (see also [191]) proved the suggestions of Burrows et al. (2005b)[24] and Zhang et al. (2006)[194] that late flares must require late injection of shells and cannot be produced by late collisions of shells ejected during the prompt phase. Yu & Dai (2009)[189] studied the shock physics and radiation processes of late internal shocks that may be responsible for X-ray flares.

In this paper, we focus on another aspect of the internal shock model for X-ray flares. Extending the work of Kobayashi et al. (1997)[81] to concentrate on X-ray

flares, we have created a GRB fireball model with a central engine that can eject multiple episodes of matter shells with any Lorentz factor, thickness and mass distributions. This code is used to address the question of what kind of central engine activities are demanded in order to reproduce the observed properties of X-ray flares. The conclusion drawn from this study may be taken as the requirements of some central engine models on X-ray flares (e.g. [77][140][144][194][36][99])[3].

Blastwave Evolution

In our model, trailing shells collide amongst themselves and later land onto the blast wave as the it slows down, altering the blast wave dynamics. The dynamics of such a collision is very complicated, invoking three shocks and several distinct dynamical stages[197]. For the purpose of this study (tracking the location of the blast wave), we adopt the following simple treatment: If a trailing fast shell with mass m_f and Lorentz factor γ_f collide on to the blast wave with Lorentz factor of γ before the blast wave has begun decelerating, the collision is treated as an internal shock and the merged Lorentz factor are calculated as prescribed by Eq.(6.1). If the collision of a fast shell onto the blast wave occurs after the blast wave has begun to decelerate, we first assume that there is no blast wave, and calculate the post-collision product the same way as the internal shock calculations, record the new effective initial mass and Lorentz factor, and re-solve the blast wave for the new parameters. We then jump the blast wave solution from the old (low) γ value to the new (high) γ-value at the same R. The code then tracks this new solution until next collision happens. With each new collision onto the blast wave, we then calculate the new solution by changing the effective mass and initial γ factor. By

[3]Other internal dissipation models for X-ray flares (e.g. [135]) may not subject to these requirements.

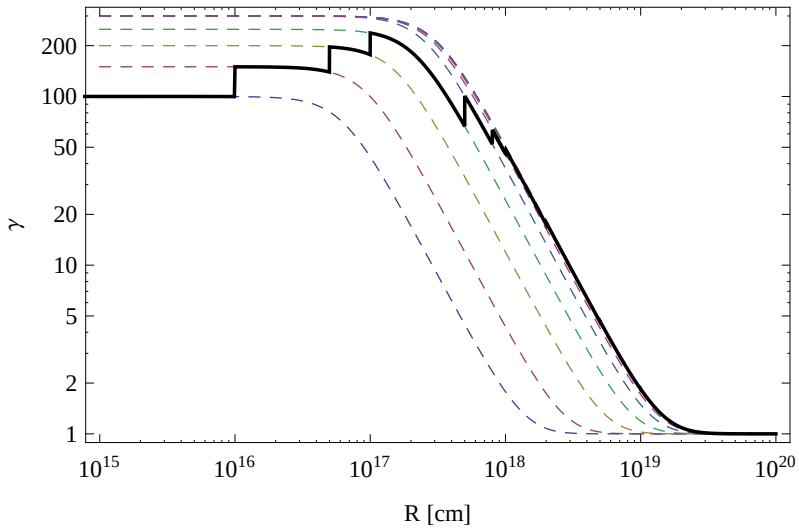

Figure 29 The blast wave shows several glitches as more and more shells pile onto it. Successive solutions are shown as dashed lines and the blast wave is shown as a solid line. Jumps in the solution become less important as the added energy from a single collision becomes less of a fraction of the total energy.

doing so, the blast wave evolution shows several "glitches" with decreasing amplitude, since the ratio between the trailing shell energy and the blast wave energy drops with time as the energy of the blast wave grows (see Fig. 42). The location R and Lorentz factor γ of the blast wave are traced at any instant t. This information is used to screen out the collisions that are not "internal". Without such a blast wave screening, shells injected from the central engine can collide at any location at any time. If the relative Lorentz factor of two shells is small, they can in principle collide at a much larger radius than the blast wave radius. Should these collisions have happened, both shells have already entered the "spreading" regime, so that the width of the shells can become very large. This would introduce some "fat" X-ray flares which are not observed. The blast wave essentially restricts such collisions, ensuring that they would never happen. Instead, both shells collide onto

the blast wave and boost up the blast wave energy. The inclusion of the blast wave dynamics is therefore essential, screening out many "fat" flares. This also explains the lack of very "fat" flares in the X-ray afterglow data.

In order to reproduce the data, we adopt a typical afterglow template according to the data [132][134][106] to denote the underlying X-ray afterglow. This is a broken power law with decay indices -1/2 and -1.25, with a break time $t_b = 6 \times 10^3$s and a break flux $\mathrm{Flux}(t_b) = 1.3 \times 10^{-11}\ \mathrm{erg\,s^{-1}\,cm^{-2}}$. The origin of the X-ray afterglow, especially the shallow decay phase, still remains a mystery. A number of very different physical mechanisms have been proposed to explain its origin (see [193] for a review). Although the refreshed shock model is mostly discussed [194][132][63], some optical afterglows do not show a similar temporal break around the X-ray break time [138][106] suggesting that this model cannot interpret all the X-ray afterglow data. Other ideas/models include a central engine powered afterglow [62][94], a long-lasting reverse-shock-dominated afterglow [59][175], two-component external shock [146][37], dust scattering [166], upscattering of blast wave photons by a trailing lepton-rich ejecta [135] and an emission component prior to the GRB trigger [186][103]. Since none of the scenarios have been robustly proven, we do not demand our model to interpret the power law X-ray afterglow segments self-consistently.

On the other hand, the expected external shock X-ray afterglow flux can be calculated from our model. Applying the standard afterglow model [161], we can calculate the X-ray lightcurve for a particular simulation. Calculating the flux for

either the fast cooling case

$$F_\nu = \begin{cases} (\nu/\nu_c)^{1/3} F_{\nu,max} & \nu_c \geq \nu \\ (\nu/\nu_c)^{-1/2} F_{\nu,max} & \nu_m \geq \nu \geq \nu_c \\ (\nu_m/\nu_c)^{-1/2} (\nu/\nu_m)^{-p/2} F_{\nu,max} & \nu \geq \nu_m \end{cases} \tag{7.1}$$

or slow cooling case

$$F_\nu = \begin{cases} (\nu/\nu_m)^{1/3} F_{\nu,max} & \nu_m \geq \nu \\ (\nu/\nu_m)^{-(p-1)/2} F_{\nu,max} & \nu_c \geq \nu \geq \nu_m \\ (\nu_c/\nu_m)^{-(p-1)/2} (\nu/\nu_c)^{-p/2} F_{\nu,max} & \nu \geq \nu_c \end{cases} \tag{7.2}$$

using the minimum Lorentz factor of the electrons $\gamma_m = \epsilon_e \left(\frac{p-2}{p-1}\right) \frac{m_p}{m_e}\gamma$, the comoving magnetic field strength $B = (32\pi m_p \epsilon_B n)^{1/2}\gamma c$, and the cooling Lorentz factor of electrons $\gamma_c = \frac{6\pi m_e c}{\sigma_T B^2 \gamma t} \simeq \frac{6\pi m_e \gamma c^2}{\sigma_T B^2 R}$,one can calculate the critical synchrotron frequencies ν_m and ν_c using $\nu(\gamma_e) = \gamma\gamma_e^2 \frac{q_e B}{2\pi m_e c}$. Standard values are taken for $p = 2.4$, $\epsilon_e = 0.1$, $\epsilon_B = 0.01$, $n = 1$ [136] and m_p, m_e, σ_T and q_e are the proton mass, electron mass, fundamental charge and Thompson cross-section, respectively. Combining this with

$$F_{\nu,max} = \frac{m_e c^2 \sigma_T}{3q_e} \gamma n B R^3 \frac{\nu}{4\pi D^2}, \tag{7.3}$$

where D is the distance from the observer, here taken to be 10^{28} cm, ν is the frequency in the X-ray band, taken to be 10^{18} Hz, one can calculate the X-ray flux density, F_ν as a function of radius taking care to switch between fast and slow cooling cases where appropriate [161].

Shells colliding onto the blast wave will produce "glitches" in the regular afterglow flux decay. Successive solutions, shown as dotted lines in Fig.7, depend upon the energy contained in the blast wave and therefore on both the Lorentz factor, γ_0,

and M_0, the effective mass of the blast wave.

We use the calculated γ-evolution to calculate the evolution of the X-ray flux. In order to plot the flux as a function of time instead of radius, points are plotted as abscissa $t = R/(2c\gamma^2)$ and ordinate flux where both flux and gamma are calculated by matching radius. Since the blast wave is accelerating in the rising part of Fig.7, here points appear to move back in time as the next solution is taken. In this part of the plot, blast wave solutions have simply been connected vertically. In the falling part of Fig.7, solutions appear to move forward in time as collisions occur. In general, all these abrupt jumps are artificial. In reality, one needs to consider the effect of equal arrival times, which smear out all the abrupt jumps so that the lightcurve would appear smoothed without noticeable individual glitches.

Also shown in Fig.7 are another blast wave solution for $\epsilon_e = 10^{-3}$, and the afterglow template adopted in other calculations throughout the paper. As evident from the figure, for the standard value $\epsilon_e = 0.1$ as derived from broad band afterglow modeling (e.g. [182][136][188]), the X-ray flux predicted by the external shock model out-shines the template flux level (which is based on observations) by about three orders of magnitude.

This is also emphasized in Fig.31 which compares the simulated lightcurve (including the contributions from the prompt emission and X-ray flares superimposed on the template) and the calculated external shock lightcurve. It is evident that no steep decay phase and X-ray flares are observable if $\epsilon_e = 0.1$ is adopted to calculate the afterglow level. This issue is carried over from the low efficiency problem of the internal shock model. If the observations are to be reproduced, there are two possibilities. The first is that the blast wave radiation efficiency is much lower. We test this possibility by lowering ϵ_e, and found that the predicted afterglow level can be roughly reproduced if ϵ_e is as low as 10^{-3} (Figs.7 and 31).

The pile-up effect of shells onto the blast wave naturally produces a shallow decay phase (after smoothing the abrupt jump features), which is an attractive feature of this internal-external-shock model. However, the anomalously small ϵ_e is inconsistent with the values derived from the previous broadband afterglow modeling, suggesting that this is likely not the correct approach to solve the problem. The second possibility is that the radiative efficiency of the prompt gamma-ray emission is very high (e.g. [202]). This requires a more efficient mechanism to generate the prompt emission. The data of the recent GRB 080916C [1] suggests that the outflow is very likely Poynting flux dominated (Zhang & Pe'er 2009). Within such a picture, Zhang & Yan (2009)[201] proposed an Internal Collision-induced MAgnetic Reconnection and Turbulence (ICMART) model, which retains the merits of the internal shock model but significantly increases the prompt emission efficiency.

The time history analysis of our shell model is also applicable to the ICMART model. The prompt emission and X-ray flare features can be retained, but the radiation efficiency is increased. Within such a scenario, the external shock level can be lowered to satisfy the observational constraint.

One can estimate the amplitude of "glitches" in the X-ray light curves. In general, collisions onto the blast wave are not energetic enough to produce a prominent signature on the afterglow light curve, unless the injection energy is comparable to that already in the blast wave [197]. In any case, small glitches from arriving shells, although not individually seen, could effectively bump up the normal decay phase, making it appear shallower. Postcollisions of shells sorted by decreasing Lorentz factor by internal collisions could produce an observable signature in early afterglow lightcurves and may be seen as temporal variability or a deviation from power-law decay[92]. The amplitude of glitches produced by postcollisions can be calculated knowing the initial mass and Lorentz factor of both the

blast wave and colliding shell and will essentially represent how far in the vertical direction successive solutions are separated. For the first few postcollisions, the amplitudes of the glitches are rather large as the added shells have both Lorentz factor and mass comparable to that of the blast wave itself. In this first stage, there is no simple approximation for calculating the jump in solution. The percent increases ($(F_f - F_i)/F_i$) are 3000%, 1000%, 500% and 150% for the presented simulation. During the deceleration phase, the X-ray flux density $F_\nu(X) \propto E^{(p+2)/4}$ for $\nu_x > \min(\nu_m, \nu_c)$ and $F_\nu(X) \propto E^{(p+3)/4}$ for $\nu_m < \nu_x < \nu_c$, where E is the total energy in the blast wave. The glitch amplitude is simply determined by the increase of the blast wave energy during each collision. During the collision, there is a reverse shock propagating to the trailing shell. However, this reverse shock usually does not contribute significantly into the X-ray band, since its density is higher, and hence, the typical electron Lorentz factor is much lower. Its dominant output is in the optical band [125][160][197]. It has been argued that for GRBs with large peaks followed by deep troughs could be used to put an upper limit on the value of γ_0 [205]. The external shock component will be superimposed on the internal shock prompt pulses and if this external shock does not rise above the level of the trough and/or threshold sensitivity of the detector at that point, this could be used to put an upper limit on the Lorentz factor of this first blast wave shell by knowing how high successive blast wave solutions will rise in flux. We find that this method, in principle, is a feasible method of putting a upper limit on γ_0 with a few caveats in mind. Figure 31 shows the blast wave solutions and blast wave (external shock component) plotted with the internal shock component lightcurve for one simulation. In general, the first shell of the external shock component will not be energetic enough to rise to the level of the prompt emission. As more and more shells pile onto the blast wave, the flux level rises and so looking for a solu-

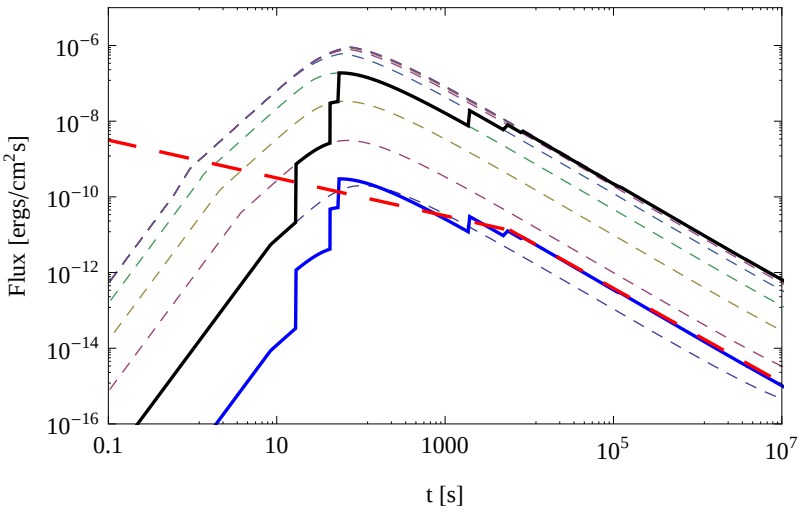

Figure 30 The flux lightcurves are shown for the same blast wave used in Fig.42, calculated based on the external shock model. The calculation of $\epsilon_e = 0.1$ is displayed in detail: the light dashed lines are the successive blast wave solutions, and the upper solid line is the corresponding blast wave lightcurve, which jumps between solutions. These glitches occur as shells pile onto the blast wave and decrease in magnitude as the energy of added shells becomes less significant. The lower solid line is the lightcurve for $\epsilon_e = 10^{-3}$, which matches the template adopted in the rest of the calculations (thick dashed line).

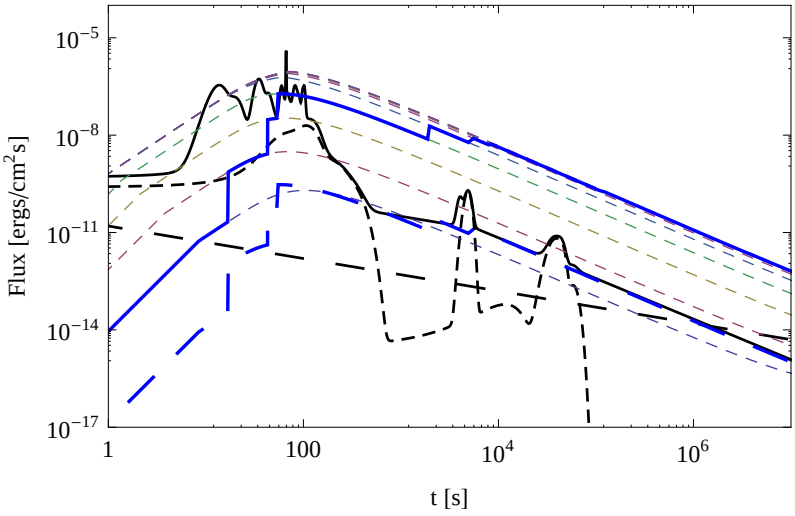

Figure 31 The calculated X-ray lightcurve including prompt emission, X-ray flares and a broken power law template (solid black line), as compared with the lightcurves calculated from the external shock blast wave model (two colored lines: $\epsilon_e = 0.1$ for the upper solid one and $\epsilon_e = 10^{-3}$ for the lower dashed one).

tion that could be extrapolated backwards to find the initial γ_0 is problematic since the external shock component, especially early on, will not be a smooth function of time. Another complication is that the flux level of the blast wave emission sensitively depends on the unknown ϵ_e parameter, making the derived upper limit of γ_0 subject to large uncertainty.

Multiple Shell Simulations

Single Injection Episode

We first model collisions of a group a shells that are injected in a single emission episode. This is relevant to GRBs that have prompt emission without distinct gaps between pulses. Allowing the central engine to eject multiple randomized shells which go on to collide, we track the information of individual shells. An example

is shown in Figs.32a and 33a. In this simulation, 100 shells are ejected where shell initial thickness, Lorentz factor and mass are chosen from random distributions in log space: Lorentz factors: $50 < \gamma < 500$, mass: $10^{29} < m < 10^{31}$, initial thickness: $10^{10} < \Delta_0 < 2 \times 10^{10}$, all in cgs units. Ejection times from the central engine are chosen from a linear random distribution $0 < t_{ej} < 100$ seconds in the rest frame of the GRB central engine. When two shells collide, we let them merge, drop one shell, and adopt the merged shell parameters (m, γ, Δ) as the new values of the remaining shell. In order to keep track of future collisions, we also need to re-set the "effective" ejection time of this new shell, which is taken as $t_{ej,m} = R_{col}/c\beta_m$, where $\beta_m = (1 - 1/\gamma_m^2)^{1/2}$. The code then runs again with one shell reduced. The same procedure is applied when each collision happens, so that the code can track all the collision/merging processes for any arbitrarily designed central engine activity. Figure 32a displays the "tree-plot" of this simulation. The upper panel displays how shells with different Lorentz factors are ejected, collide and merge at various distances. The time information is not displayed, but the collision times t_{col} (again in the rest frame of the central engine) can be read off from the lower panel. This time is translated into the observed time according to Eq.(6.8) to calculate the lightcurve (Fig.33a). The evolution of the blast wave is also marked in the upper panel as a thick red line. Collisions are "disallowed" if the shells collide with the blast wave (i.e. they would have collided at a radius greater than that of the blast wave, had the blast wave not existed.). These shells are included to boost the blast wave energy and become part of the blast wave after the collision and are therefore no longer traced in the later simulation. Our results suggest that a single episode can reproduce prompt emission of some GRBs. Even for simulations with a large number of shells, the ejection time in the frame of the central engine (t_{ej}) is correlated to the observed time of the collision ($t_{\oplus,col}$) with little scatter (Fig. 34,

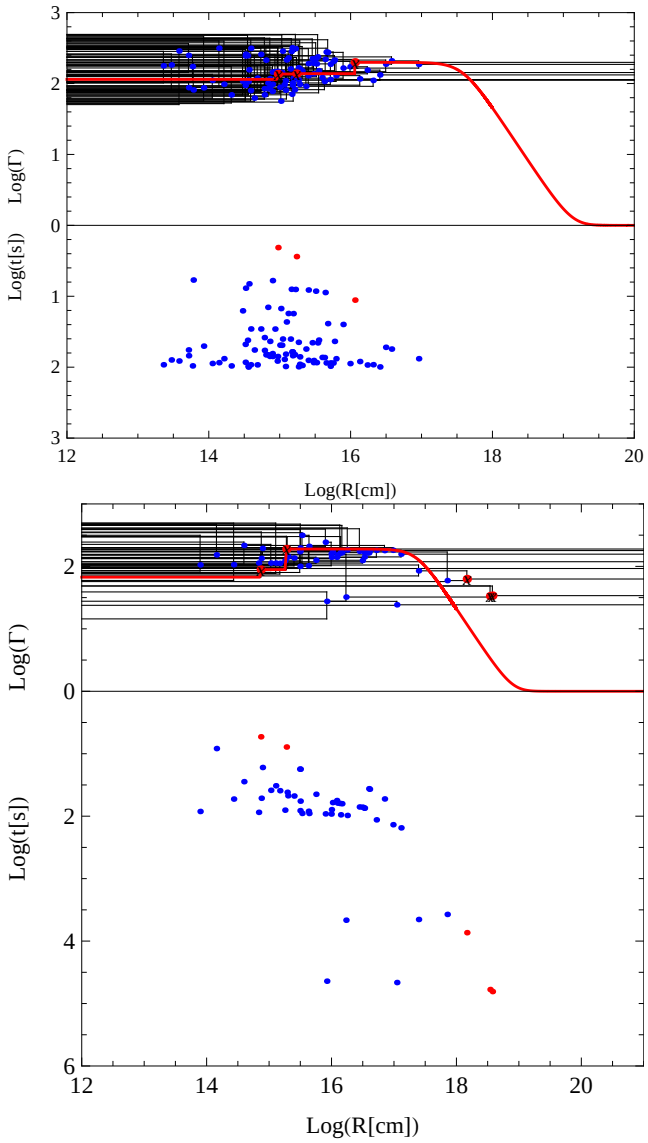

Figure 32 Tree plots showing simulated collisions as both Lorentz factor versus radius (top panes) and time of collisions versus radius of collisions (bottom panes). Lorentz factors are read up the y-axis starting at zero, time of collision is read down the y-axis, also starting at zero. The top pane shows shells as black lines, collisions are marked with dots. The time of collision can be found by dropping down vertically to the bottom pane of the graph, matching radius. The blast wave is shown in the top panels as a thick red line. Allowed collisions are blue dots, excluded collisions are red dots. For the top pane, 100 shells are ejected between 0 and 100 seconds with Lorentz factors between $50 - 500$. For the bottom pane, 50 A shells are ejected between $0 < t_{ej} < 100$ seconds, 5 B shells $3000 < t_{ej} < 5000$ and 5 C shells $30000 < t_{ej} < 50000$ seconds.

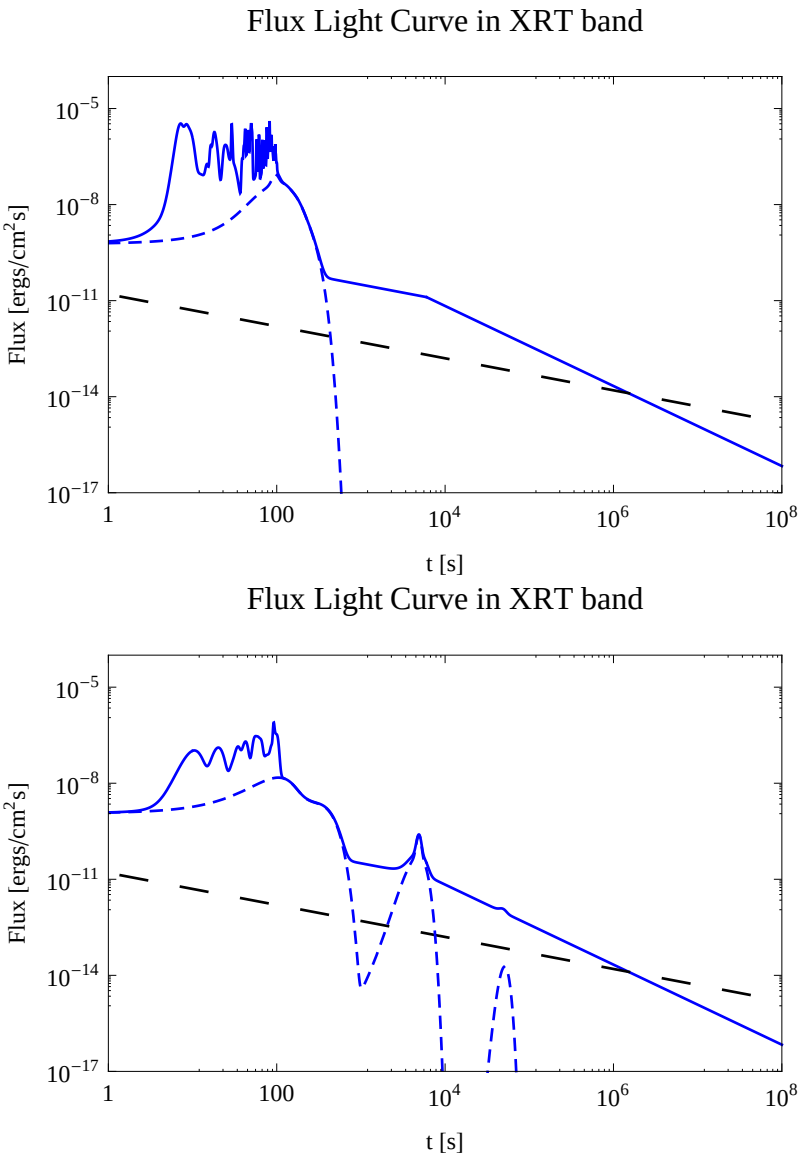

Figure 33 A simulation with many shells in a single short episode will produce prompt emission only and no late collisions which could be responsible for X-ray flares. Top panel is a single ejection episode N = 100, $0 < t_{ej} < 100$ seconds. Bottom panel a simulation of N = 50 A shells, $0 < t_{ej} < 100$ seconds, 5 B shells $3 \times 10^3 < t_{ej} < 5 \times 10^3$ seconds and 5 C shells $3 \times 10^4 < t_{ej} < 5 \times 10^4$ seconds. Dashed lines show the position of flares underneath the superimposed afterglow.

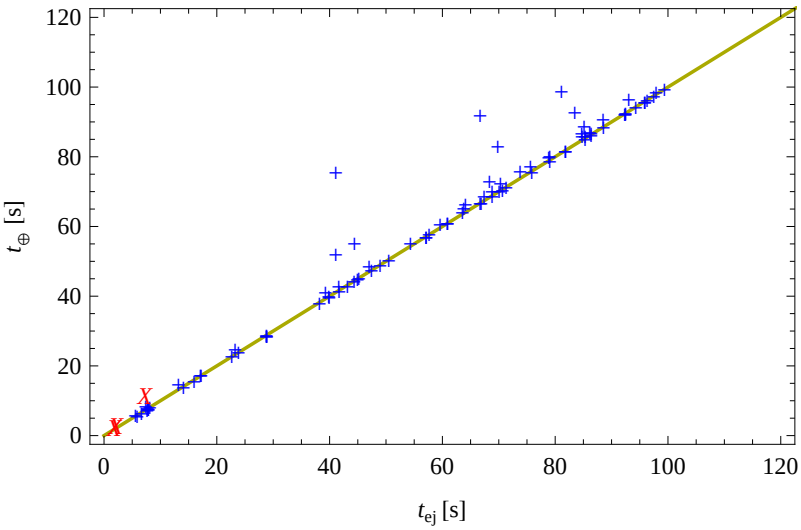

Figure 34 The ejection time of a shell in the GRB central engine rest frame (t_{ej}) versus the collision time in the observer frame $t_{\oplus,col}$. Allowed collisions are pluses, crosses are excluded. Even for a large number of shells (N = 100, ejected in 100 seconds), there is little scatter around a line of unity.

see also [81]). There are indeed collisions with much larger collision times (red crosses), but they are "excluded" by the blast wave constraint. If prompt emission and X-ray flares are indeed produced by the same mechanism, late flares are unlikely to be produced by shells that are ejected early. As discussed in the following, they demand re-activation of the central engine. Lightcurves are produced by considering the spectral model and temporal model as discussed in §2. The XRT band lightcurve of this particular simulation is shown in Fig.33a. The relevant detector threshold (thick, dotted line) is also added. (D. N. Burrows, 2008, private communication). It is evident that without late central engine activity, no X-ray flares can be detected.

Multiple Injection Episodes

In order to reproduce the observed X-ray flares that occur in distinct emission episodes from the prompt emission, we are obliged to simulate multiple ejection episodes from the central engine. The results are displayed in Figs. 35, 32b, 33b and 43. In these simulations, three groups of shells ("*A*", "*B*" and "*C*") are released. The *A* group consisting of 50 shells is released in the first 100 seconds. The majority of these shells merge with each other producing *AA* type collisions. The energy released in each collision is shown as "AA" in Fig.35. Similar to the previous simulation , most *AA* type collisions occur before 100 seconds. After 3000 seconds, we release a set of 5 *B* group shells with energies reduced by ~ 20 times on average. These shells can have two types of collisions: *BB* type collisions or *AB* type collisions (see Fig.35). Both the *AB* and *BB* type collisions could produce X-ray flares, as long as they are bright enough to stick out above the power law afterglow level (the broken power law template). For late X-ray flares, the energy of these collisions is of the "goldilocks type": high enough to be above the background decay, but small enough to peak in the X-ray band and therefore remain undetectable by BAT. After 30,000 seconds, a third batch of *C* shells are released with energy lower than that of the *B* shells by ~ 20 times again. This can in principle produce *CC*,*AC* or *BC* collisions, but for this particular simulation, *AC* and *BC* collisions are lacking (Fig.35). These cross collisions are disfavored since their collision radii tend to be large (due to the large ejection gap between the shells), so that the leading shells likely have collided onto the blast wave before the trailing shell catches up. Progressively less energy in *A*, *B* and *C* shells allows progressively degrading energetics of the X-ray flares, as is commonly observed. This is also generally consistent with various central engine models, where the accretion

or magnetic power of the engine tends to die off with time.

Another interesting topic is to investigate how the observed widths of X-ray flares can be reproduced. In particular, the observed $\delta t/t \sim 0.1$ trend suggests that the later flares (larger t) are wider (larger δt). This requires that the shell width Δ broadens with time. A natural broadening mechanism is shell spreading (Eq.[6.7]). After a shell enters the spreading regime, the width of the shell is proportional to the radius, so that resultant X-ray flare width can be wide if the collision radius is large. Without placing the blast wave constraint, one indeed expects many "fat" flares, corresponding to very large radius collisions. With the blast wave constraint, the number of "fat" flares reduces significantly. Figure 37a displays the model-predicted flare width as a function of their occurrences for a narrow distribution of the initial width Δ_0 (between $10^{10} - 2 \times 10^{10}$ cm, with the $\delta t/t = 0.1$ line over plotted. The blue pluses are allowed but the red crosses are disallowed. The result suggests that although the predicted values are around the $\delta t/t = 0.1$ line, the scatter is broader than what is observed. In particular, many narrow flares are predicted (those without significant spreading). The lightcurve for this simulation is presented in Fig.38a, which shows narrow late time flares that are not observed by the Swift/XRT data. In order to reproduce the observations, one is required to increase the initial shell width Δ_0 for late ejection episodes. Figures 37b and 38b show an example of late injection of "fat" shells. Generally, $\Delta_0 \propto t_{ej}$ is needed to reproduce the observed data. This is consistent with the expectations of some central engine models. For example, in the fragmented disk model proposed by Perna et al. (2006)[140], the clumps at larger radii have lower densities and tend to be more spread out so that the accretion time scale is longer. The ejected shells correspondingly also have longer durations.

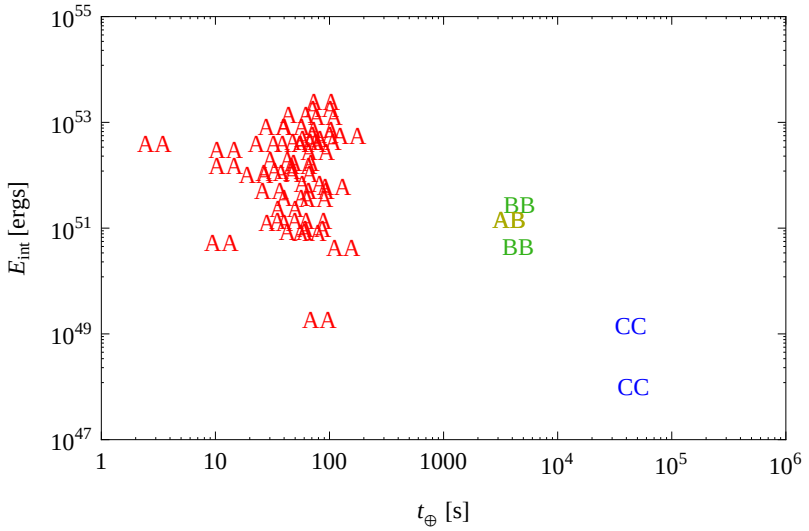

Figure 35 A bolometric light curve for 50 A shells ejected within the first 100 seconds, followed by 5 B shells after 3000 seconds and 5 C shells after 30,000 seconds representing a restarting of the central engine. Collision energies are shown by type; "AA" represents collisions between to A shells, "AB" between an A shell and a B shell etc.

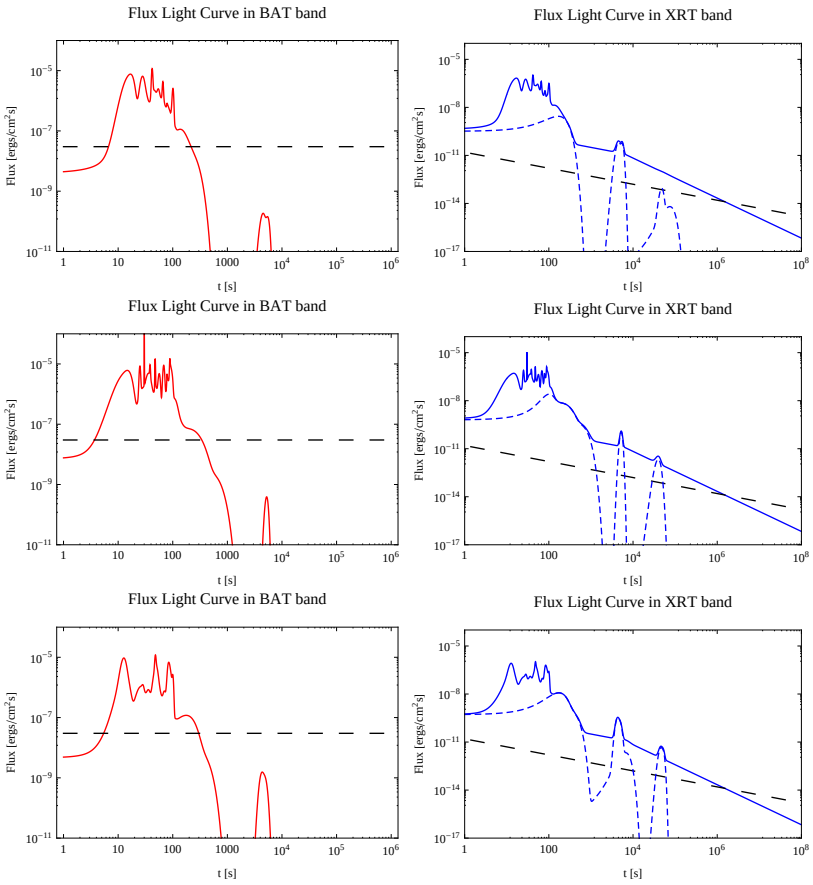

Figure 36 BAT (left) and XRT (right) light curves for three typical simulations of 50 A, 5 B shells and 5 C shells of decreasing energy. Long dashed lines are the detector thresholds and short dashed lines in XRT lightcurves represent the positions of the flares underneath the afterglow.

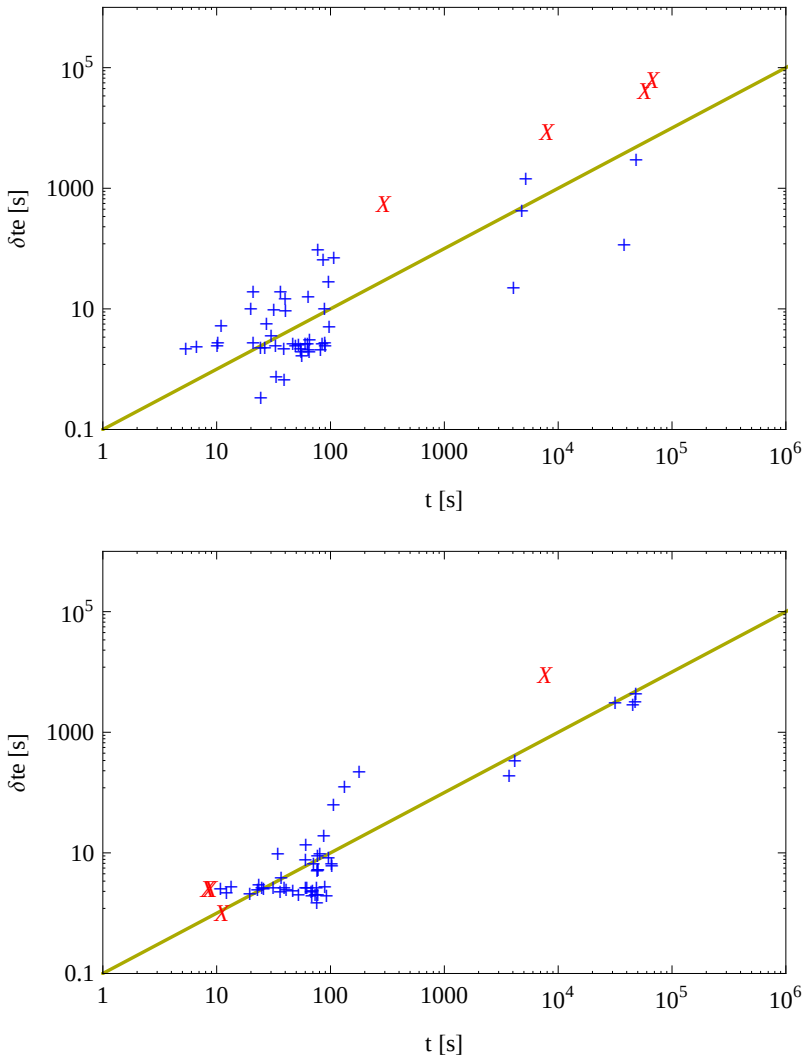

Figure 37 How fat are the flares compared to the time of their occurrence? By the time most shells have spread, creating a broad flare, these shells have already collided with the blast wave or are not energetic enough to be seen. Observed flares are, on average, 1/10 of their occurrence times in width, this line is shown. Excluded collisions are shown as crosses, allowed collisions are pluses. The top panel is for shells of the same width, the bottom for shells which are wider for later ejection episodes.

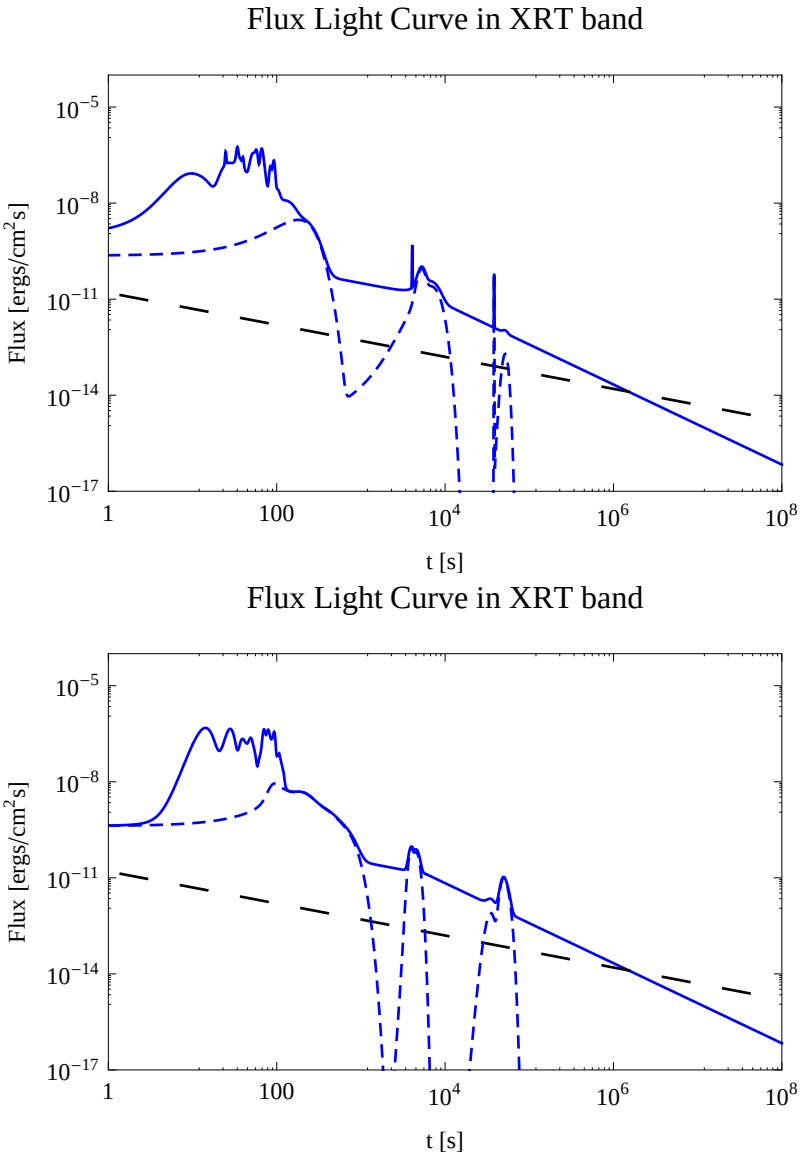

Figure 38 Simulations with uniform shell widths (top) produce flares which are more narrow on average than observed flares. In order to reproduce observed wide flares, shells must be ejected with widths scaling as their ejection time (bottom panel). Notations are the same as for Fig. 43

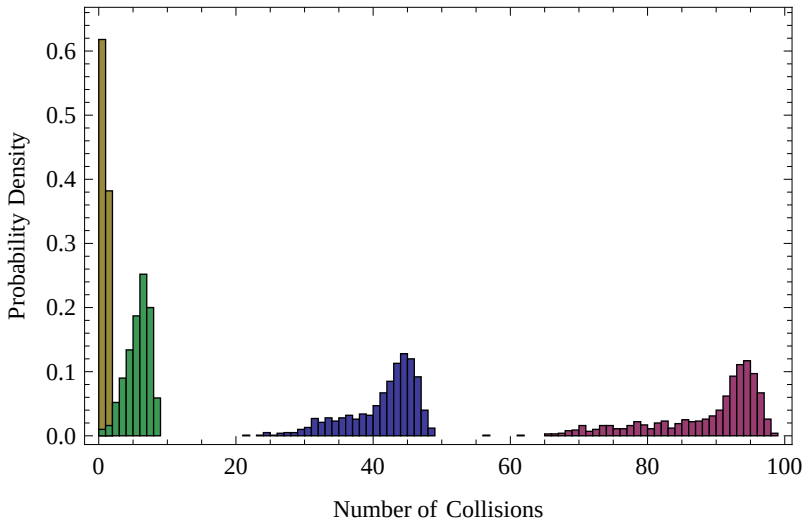

Figure 39 The most likely number of allowed collisions for simulations with 4, 10, 50 and 100 shells. 1000 simulations were run for each.

Conclusion

We have developed a numerical code to model the internal collisions of an unsteady wind with arbitrary central engine activities. This is an extension of the internal shock models previously developed to model GRB prompt emission (e.g. [81]), with a focus on X-ray flares that are commonly observed in GRB X-ray afterglows (e.g. [29]). Our motivation is to diagnose the required central engine activities based on the observational properties of X-ray flares as summarized in above. The following conclusions can be reached:

- The internal shock model with multiple ejection episodes can generally reproduce the properties of X-ray flares. Our shell model naturally explains both prompt emission and X-ray flares, suggesting that they originate from very similar mechanisms.

- We find that the number of pulses/flares is directly related to the number

of shells released from the central engine. More shells means more flares. In general, we find that the number of collisions is slightly smaller than the number of the shells ejected (e.g. the most probable values are: 5% less for 100 simulated shells, 10% less for 50 simulated shells, 8 collisions for 10 simulated shells and 1 collision for 4 simulated shells, see Fig.39 for distributions). For a modal number of observed flares of 1, between 2 and 5 shells need to be released on average.

- The correlation between t_{ej} and $t_{\oplus,col}$ ensures that the shells that are responsible for creating flares must be ejected just prior to being seen. This is because the second term in the right hand side of Eq.(6.8) is typically much shorter than the first term. This means that not only the central engine activity must be prolonged, but it must also be episodic. Steady energy injection cannot produce flare-like features. In other words, early flares are created by shells ejected early, while late flares by shells ejected late. Since flares are seen as late as 10^6 seconds, this means that the central engine can be active for a long time after the prompt emission. These conclusions are consistent with Zhang et al. (2006)[194], Liang et al. (2006)[107] and Lazzati & Perna (2007)[97].

- The large variance of fluences seen in flares can be explained by the different energies ($E \sim \gamma mc^2$) of the ejected shells. The peak luminosity of a flare also depends on the width of the pulse, which is either related to shell spreading or intrinsically different durations of shell ejection.

- This study seems to rule out uniform (or narrow distribution) thickness shells. The observed widths of flares cannot be reproduced solely by spreading effects. One requires that later ejection episodes eject shells with larger widths to explain the typical flare width of $\delta t_e/t \sim 1/10$. Since most shells collide

before spreading, typical late collisions would be too narrow if later ejected shells had the same width as the initial prompt ejection episodes. Sharp flares where the width is near $1/10$ of the emission time of the flare are common, but "fat" flares are seen occasionally as well. For example, the giant flare of GRB050502B has a $\delta t_e/t \sim 1$ [29] implying that shells may either have spread before colliding or may simply have had a large width when ejected. Shells which have spread significantly before colliding will have energies spread over a large log-Gaussian shape and may be too dim to reach above the afterglow decay.

- For goldilocks type shells, flares are seen in the XRT band only. The gamma-ray component of the X-ray flare (Band-function extension) is below the BAT detector threshold. Figure 43 shows light curves from a few typical simulations and these features can be seen.

- Flares superimposed on other flares are simply shells that collide near the same time with different widths and fluences. The observed X-ray afterglow is a superposition of flares due to prolonged central engine activity and a background afterglow radiation, whose origin is not addressed in our paper.

- The decrease in average flare luminosity as a function of time indicates shells released at later times must create less energetic collisions [98]. In order to produce the results seen, late released shells must be wider, less dense, slower or a combination of the above in order to create less energetic collisions seen.

- The same shell model can give a prediction on the X-ray afterglow emission from the blast wave. Due to the continuous piling up of late-ejection shells

onto the blast wave, the lightcurve can show a shallow decay phase that is commonly observed. However, if a standard value $\epsilon_e = 0.1$ is adopted, the predicted X-ray lightcurve is much brighter than what is seen, by about three orders of magnitudes. In order to reproduce the observed data, either a much lower ϵ_e (as low as 10^{-3}) needs to be introduced, or the internal emission that powers the prompt emission and X-ray flares has to be much more efficient than internal shock predictions.

Recently there has been interest in optical flares [95][118]. These flares can be naturally interpreted in our model by invoking collisions between low energy shells or wide shells. Such collisions could be seen in optical bands but may be missed in higher energy bands. A direct expectation from this model is that optical flares should on average have lower energies and broader profiles than X-ray flares. An internal shock origin of optical flares was also proposed by Wei (2007)[181].

Finally, we want to emphasize that observationally flares have been seen in both Type I (e.g. GRB 050724) and type II GRBs. This requires that both types of progenitor have a similar central engine, which can eject an episodic wind to power late central engine activities which is a requirement of any central engine models for X-ray flares.

CHAPTER 8

FLARES IN GRB 090926A

Introduction

[1] GRB 090926A was detected by both the GBM[120] and LAT[7] instruments on-board the Fermi Gamma- Ray Space Telescope. Swift follow-up observations began $\sim$ 13 hours after the initial trigger. The optical afterglow was detected for nearly 23 days post trigger, placing it in the long lived category. The afterglow is of particular interest due to its brightness at late times, as well as the presence of optical ares at $T_0 + 10^5$ s and later, which may indicate late-time central engine activity. The LAT has detected a total of 16 GRBs; 9 of these bursts, including GRB 090926A, also have been observed by Swift. Of the 9 Swift observed LAT bursts, 6 were detected by UVOT, with 5 of the bursts having bright, long-lived optical afterglows.

The Fermi Gamma-ray Space Telescope has opened a new era of gamma-ray burst (GRB) observations. Used in conjunction with Swift[56], GRB afterglows can be studied across a nearly continuous band from GeV energies to optical wavelengths. As of April 1, 2010 the Fermi GBM has triggered on nearly 450 GRBs, 16 of which have also been seen by the LAT. Of the 16 LAT-detected GRBs, one was simultaneously localized by the Swift Burst Alert Telescope (BAT; [10]), and 8 others had Swift follow-up observations at late times. The Swift X-ray Telescope (XRT; [23]) detected the X-ray afterglow from 7 of the 9 LAT bursts; 6 of the 7 with X-ray afterglows detected by the Swift UV/Optical Telescope (UVOT; [155]). All but one of the UVOT afterglows stand out due to their brightness and length of detectability.

GRB 090926A is a LAT-detected burst with a bright, long-lived UVOT after-

[1] The content of this chapter is drawn from Maxham & Zhang (2009)[173]

glow. In this chapter, the multiwavelength study of GRB 090926A is presented, examining the X-ray and UV/optical wavelengths as observed by Swift.

Observations and Data Reduction

Fermi Data

At 04:20:26.99 UT on 2009 September 26, the GBM triggered on GRB 090926A[17]. The GBM light curve, Fig. 1, consisted of a single pulse with T_{90} of 20 ± 2 s (8-1000 keV). The time-averaged, combined GBM/LAT spectrum from T_0 to $T_0 + 20.7$ s, where T_0 is the trigger time, is best fit by a Band function[8], with $E_p = 268 \pm 4\mathrm{keV}$, $\alpha = -0.693 \pm 0.009$ and $\beta = -2.342 \pm 0.011$. The fluence (10 keV - 10 GeV) during this interval is $(2.47 \pm 0.03) \times 10^4 \mathrm{ergscm}^{-2}$, bright enough to result in a Fermi repointing. In the first 300 s, LAT observed 150 and 20 photons above 100 MeV and 1 GeV, respectively. Possible extended emission continued out to a few kilo-seconds. The highest energy photon, 19.6 GeV, was observed 26 s after the trigger. The LAT light curve, Fig. 40, is fit by a power-law of $\alpha = -2.17 \pm 0.14$. We fit the LAT spectrum, from 100 - 1000 s, with a power-law of $\beta = -1.26^{+0.24}_{-0.22}$.

XRT Data

XRT began observing GRB 090926A ∼46.6 ks after the Fermi trigger, in Photon Counting (PC) mode. The light curve, Fig. 41 (taken from the XRT light curve repository[38][39]), shows a decaying behavior with some evidence of variability, and is fit with a single power-law, decaying with $\alpha = -1.40 \pm 0.05$ (90% confidence level). The average spectrum from 46.6 ks - 149 ks is best fit by an absorbed power-law model with $\beta = -1.6^{+0.3}_{-0.2}$ and an absorption column density of $1.0^{+0.5}_{-0.3} \times 10^{21}\mathrm{cm}^{-2}$ in excess of the Galactic value of $2.7 \times 10^{20}\mathrm{cm}^{-2}$ (Kalberla et

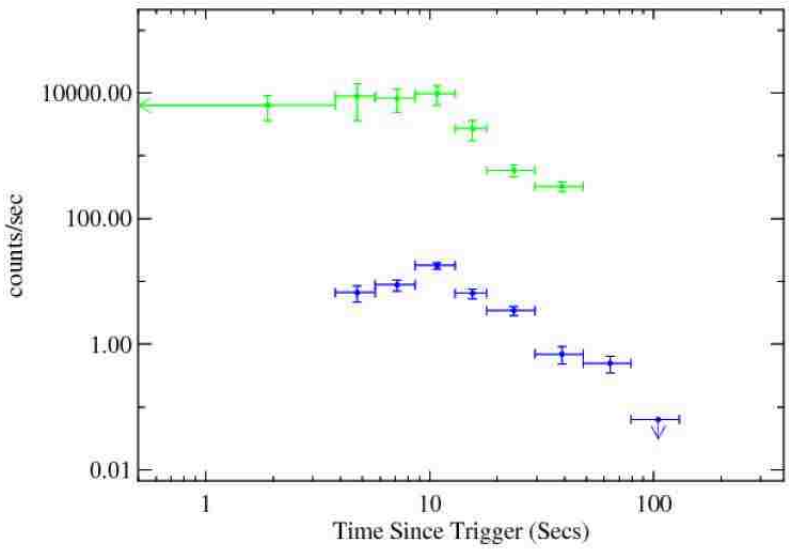

Figure 40 Fermi GBM (green) and LAT (blue) lightcurves of GRB 090926A.

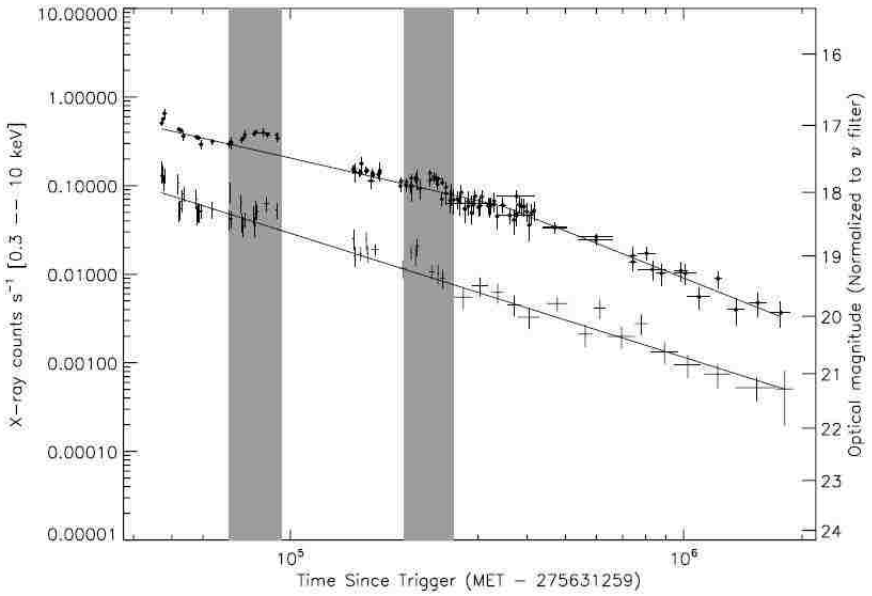

Figure 41 Swift XRT (bottom) and UVOT (top) lightcurves of GRB 090926A. Shaded regions indicate periods of flaring.

al. 2005). The counts to observed flux conversion factor deduced from this spectrum is $3.5 \times 10^{-11}\mathrm{ergscm^{-2}count^{-1}}$. The average observed (unabsorbed) fluxes are $1.3(1.9) \times 10^{12}\mathrm{ergscm^{-2}s^{-1}}$.

UVOT Data

UVOT began settled observations of GRB 090926A at $T_0+ \sim 47\mathrm{ks}$, and the optical afterglow was immediately detected[67]. The resulting optical afterglow light curve is shown in Fig. 41. Removing these ares, the underlying optical light curve is well fit ($\chi^2_{red} = 0.92/82\mathrm{d.o.f.}$) by a broken powerlaw. The best fit parameters are: $\alpha_{Opt,1} = -1.01^{+0.07}_{-.0.03}$, $t_{break} = 351^{+70.2}_{-141.9}\mathrm{ks}$, $\alpha_{Opt,2} = -1.77^{+0.21}_{-0.26}$. X-shooter, mounted on the Very Large Telescope UT2, found a spectroscopic redshift of $z = 2.1062$ [111].

Flaring Activity

The variability in the X-ray is not statistically strong (peaking $\sim 2.8\sigma$ above the underlying fit) but is temporally coincident with stronger flaring in the UVOT. The first flare, at $\sim 70\mathrm{ks}$ - $95\mathrm{ks}$, is well defined in the UVOT lightcurve with $\delta t/t \approx 0.35$, but is only seen in the X-ray as minor variability, with individual points varying from the underlying fit. The second are, at $195\mathrm{ks}$ -$260\mathrm{ks}$, is better defined in the X-ray (though only peaking at $\sim 1\sigma$) but is matched by a similarly shaped, stronger feature in the UVOT ($\delta t/t \approx 0.28$). Due to an observing gap, we may not have observed the peak of the UVOT feature, but it appears to lag the peak of the X-ray feature by at least $6\mathrm{ks}$, which is consistent with lower energy emission from flares lagging the higher energy [113].

GRB 090926A late time ares X-ray ares at late times have been attributed to two different sources[185]: central engine powered internal emission, or features of the external shock. There is evidence suggesting that the GRB prompt emission and X-ray ares originate from similar physical processes (see [24][194][29][85]), including a lower energy budget and 'spiky' flares more like those actually seen in X-ray light curves. If the central engine is the source of GRB flares, the X-ray flare spectrum should be similar to that of the prompt spectrum. In the case of GRB 090926A, the prompt emission was seen to have a Band function spectrum. Assuming the optical behaves similarly to the X-ray and that the flares are caused by central engine activity, we would expect a Band function spectrum during the flares. A Band function spectrum is not observed during the X-ray variability or optical flares.

The flares are both well fit by a power-law, with no indication of a break in the spectrum or sign of spectral evolution in the X-ray. It should be stated, however, that the statistics of the X-ray light curve are low enough that detecting a Band spectrum may not be possible, even if it exists. Combining the poor statistics with the dominate underlying continuum, it is not surprising that a power-law is the best fit. We also find no evidence of change in the spectral shape after creating a spectral energy distribution using optical/UV photometry before and during the first flare.

A non Band-like spectrum for the flares does not expressly prohibit central engine activity from being the source of the flares, but it does allow for alternate explanations. Code for modeling X-ray flares in GRBs developed by Maxham and Zhang (2009)[114] can produce optical flares through the collision of low energy

shells or wide shells.

If the two flares are indeed due to internal shocks, then this code can put constraints on the time of ejection and maximum energy (Lorentz factor) of the matter shells that could produce such flares. Since ejection time in the GRB rest frame is highly correlated to the collision time of shells in the observer frame, this means that the central engine is active around 70 ks and 197 ks. Using the prompt emission fluence to constrain the total energy contained in the blastwave, the internal shock model requires that Lorentz factors of the shells causing flares must be less than the Lorentz factor of the blastwave when the shells are ejected. Fast moving shells will simply collide onto the blastwave giving small, undetectable glitches, whereas slow moving shells will be allowed to collide internally, releasing the energy required to detect a flare. Specifically, we find maximum Lorentz factors of 8.2 $(\frac{E_{52.3}}{n})^{1/8}$ and 5.5 $(\frac{E_{52.3}}{n})^{1/8}$ for the first and second flare, respectively and in terms of the energy in the prompt emission in units of $10^{52.3}$ ergs and number density of the ambient medium.

Collisions between these relatively low energy shells are expected to be seen in lower energy bands such as UVOT. In the synchrotron emission model, $E_p = 2\Gamma\gamma_e 2\frac{\hbar e B}{m_e c} \propto L^{1/2}$ for electrons moving with a bulk Lorentz factor Γ with typical energy $\gamma_e m_e c^2$, since the comoving magnetic field $B \propto L^{1/2}$ [197]. This is consistent with the empirical Yonetoku relation $E_p \propto L_{iso}^{1/2}$ [187] for prompt GRB emission. Applying this relation to the two flares, one predicts E_p of 0.8 and 0.5 eV for each flare, respectively. This is consistent with the observation that both flares are more prominent in the optical band than in the X-ray band. Finding E_p using the Amati relation, $E_p \propto E_{iso}^{1/2}$[5], gives E_p values for both flares around 1 keV, which are inconsistent with the observation. Unlike for individual burst pulses (whose durations do not vary significantly), which seem to follow an Amati relation [86], the

Yonetoku relation may be more relevant for flares because it is consistent with the more generic synchrotron emission physics. Since the duration of a flare depends on the epoch of the flare (the time it is seen), the Amati relation is not expected to hold. An $E_p - E_{iso}$ correlation may be obtained if one takes the luminosity relation (Yonetoku relation) and another relation between the epoch of flare and the flare luminosity, and calculates E_{iso} by multiplying mean luminosity by the flare duration (which scales with the epoch of flare). The slope of the $E_p - E_{iso}$ relation (if any) would therefore be different from the $1/2$ power of the Amati relation.

GRB 090926A was a long burst with more than 20 photons in the GeV range, that was also easily detected by the Swift XRT and UVOT nearly 13 hrs after the initial trigger and has late time ares in the UVOT afterglow. The overall brightness and behavior of the optical afterglow are more reminiscent of afterglows observed immediately after the trigger, as opposed to observations starting at 47 ks after the trigger[133][156]. The late time light curve could be due to late time energy injection, supported by the presence of ares in the lightcurve, or could be a LAT selection effect.

CHAPTER 9

GEV EMISSION FROM GAMMA-RAY BURSTS

[1] Recent observations of Gamma-Ray Bursts (GRBs) by the Fermi Large Area Telescope (LAT) revealed a power law decay feature of the high energy emission (above 100 MeV), which led to the suggestion that it originates from an external shock. We analyze four GRBs (080916C, 090510, 090902B and 090926A) jointly detected by Fermi LAT and Gamma-ray Burst Monitor (GBM), which have high quality lightcurves in both instrument energy bands. Using the MeV prompt emission (GBM) data, we can record the energy output from the central engine as a function of time. Assuming a constant radiative efficiency, we are able to track energy accumulation in the external shock using our internal/external shell model code. By solving for the early evolution of both an adiabatic and a radiative blastwave, we calculate the high energy emission lightcurve in the LAT band and compare it with the observed one for each burst. The late time LAT light curves after T_{90} can be well fit by the model. However, due to continuous energy injection into the blastwave during the prompt emission phase, the early external shock emission cannot account for the observed GeV flux level. The high energy emission during the prompt phase (before T_{90}) is most likely a superposition of a gradually enhancing external shock component and a dominant emission component that is of an internal origin.

Introduction

The Large Area Telescope (LAT[7]) aboard the Fermi Gamma Ray Space Telescope (Fermi) has recently detected nearly 20 GRBs (e.g. [1][2][3][4], see [192] Zhang et al. 2011 for a synthetic study). Among them, several bright GRBs (e.g.

[1]The content of this chapter is drawn from Maxham & Zhang (2011)[115]

GRBs 080916C, 090510, 090902B and 090926A) have well sampled long-term LAT-band lightcurves. In logarithmic space, these GRBs have count rates that rise, peak and begin decaying before the MeV prompt emission is over, i.e. peaking at a time smaller than T_{90} defined in the Gamma-ray Burst Monitor (GBM[120]) detector energy band. The post peak lightcurve typically has a decay slope steeper than -1 (e.g. ranging from -1.3 to -2, [61][192]). The simple temporal behavior (a broken power law lightcurve) of LAT emission led to the suggestion that GRB GeV emission is of an external forward shock origin[88][89], possibly from a highly radiative blastwave [61] or a Klein-Nishina cooling dominated adiabatic blastwave [179].

A simple broken power law lightcurve is expected from the blastwave evolution of an instantaneously injected fireball with fixed explosion energy. Such an approximation is valid if the analyzed time scale is much longer than T_{90}, the duration of the prompt gamma-ray emission itself. However, for the early blastwave evolution, especially during the epoch when the central engine is still active (as is the case for the LAT GRBs discussed in this paper), one would not expect a simple lightcurve evolution, since the energy output from the central engine is continuously injected into the blastwave.

The high quality spectral and temporal data of GRBs co-detected by Fermi LAT and GBM allow us to track the energy output from the central engine as a function of time. Recently we have developed a shell code to model the internal and external shock development for arbitrary central engine activities[114]. By processing the spectral and temporal evolution data of Fermi GRBs using the method described in Zhang et al. (2011)[192], we can model the early development of the external shock based on first hand data.

Data Analysis

We study four bright LAT GRBs (080916C, 090510, 090902B, and 090926A). GBM and LAT data reduction was carried out using the data analysis script introduced in Zhang et al. (2011)[192]. This code uses the public Fermi data and extracts time-resolved spectral information derived from a joint GBM/LAT fit. For the GBM data, the background spectrum is extracted using the CSPEC data, while the source spectrum is extracted using the event (TTE) data. The LAT background is different since only a few photons are detected by LAT for most GRBs, so on-source region data long after the GBM trigger when the photon counts merge into a Poisson noise are used to derive the LAT lightcurve background. The GBM and LAT data are then used to make dynamically time-dependent spectral fits. The code refines the number of time slices as necessary to preserve adequate statistics in each bin, and a spectral fit is chosen among a list of spectral models, such as a single power-law, a power-law with exponential cut-off, a Band function, a black body or a combination of these. Chi square statistics are performed to determine which fits are the best, and Ockham's Razor chooses the simplest spectral model between two statistically reasonable fits[192].

For the 4 bright GRBs in our sample, we adopt the following models (for details, see [192]). For GRB 080916C and 090926A we adopt the Band function model throughout the burst, with the spectral parameters evolving with time. GRB 090902B shows a blackbody thermal component plus a non-thermal single power law component, and the short burst GRB 090510 is best-fit with a cutoff power law plus power law component. Similar to Ghisellini et al. (2009)[61], we found that the long-term LAT light curves decay before the end of T_{90} with a slope steeper than -1.

External Shock Modeling: The Blastwave Evolution

We model a GRB as an explosion of many matter shells with some mass and Lorentz factor[150]. As the first matter shell moves outward into the ambient medium, it slows down when sweeping up this medium [124]. As time goes by, more and more trailing shells pile up onto the leading decelerating shell[151]. The equations governing blastwave evolution are solved analytically. The adiabatic solution was presented as Eq.(14) in Maxham & Zhang (2009)[114]. Since the LAT lightcurves decay with a slope steeper than -1 (typical value for an adiabatic blastwave), e.g. in the range of -1.3 and -2 [192], one possibility is that the blastwave evolution is completely radiative [61]. By adopting a value of $\epsilon = 1$, one can get a purely radiative solution for the blastwave, which reads

$$\gamma = \frac{9(M_0\gamma_0)^2 + 12\pi\rho M_0 R^3(1+\gamma_0) + 8\pi^2\rho^2 R^6(1+\gamma_0)}{9M_0^2 + 12\pi\rho M_0 R^3(1+\gamma_0) + 8\pi^2\rho^2 R^6(1+\gamma_0)}. \tag{9.1}$$

In the deceleration regime, one has $\gamma \propto R^{-3}$, and $F_\nu \propto t^{(2-6p)/7}$ for $\nu > \max(\nu_m, \nu_c)$ (which is relevant for LAT band), which is $F_\nu \propto t^{-1.6}$ for $p = 2.2$ (e.g. [161]). This is consistent with the rapid decay observations.

Energy Injection onto the Blastwave

During the prompt emission phase (i.e. $T < T_{90}$), the central engine continuously injects energy into the blastwave. So the solution should take into account the progressively increasing total energy in the blastwave. We apply the shell code developed and laid forth in Maxham & Zhang (2009)[114] to this problem. The code, which originally generated randomized matter shells with different mass, Lorentz factor and ejection time, is here modified to use input values for these parameters which are taken from the data as follows.

The most important parameter affecting blastwave evolution is the total injection energy. In principle the injected energy during each episode is the kinetic energy of the ejecta after energy dissipation during the prompt emission phase. Lacking a direct measure of this energy, we hereby assume that the emitted γ-ray energy is a good proxy of the kinetic energy, so that $E_k = \xi E_\gamma$. In other words, we assume a constant radiative efficiency throughout the burst. We take $\xi = 1$ as the nominal value (i.e. 50% radiative efficiency, which may be achieved for efficient magnetic energy dissipation[201]. In order to fit the data, we also allow $\xi > 1$ for the GRBs, which corresponds to a less efficient dissipation mechanism (e.g. in internal shocks[137][87][114].

To evaluate γ-ray energy E_γ as a function of time, we divide the lightcurve into multiple time bins for each burst. For each time bin (with uneven duration denoted as ΔT_i for i-th bin), we record its average flux F_i in the GBM band, along with other useful information such as spectral parameters and the maximum photon energy.

The total gamma-ray energy released in this time bin (i-th) is therefore

$$E_{\gamma,i} = \frac{4\pi d_L^2 F_i \Delta T_i}{1+z}. \tag{9.2}$$

where z is the redshift (see Table 1 for values of each burst), d_L is the luminosity distance of the source, and the concordance cosmology with $\Omega_\Lambda = 0.7$ and $\Omega_m = 0.3$ is adopted in the calculation.

Adopting $E_{k,i} = \xi E_{\gamma,i}$, we then progressively increase the total energy in the blastwave $E_k = \Sigma E_{k,i}$ by adding $E_{k,i}$ in each step. For each time step, we calculate the lightcurve giving the available E_k. This results in a series of lightcurve solutions. The final lightcurve is then derived by jumping to progressively higher level solutions due to additional energy injections in each time step (see also [114]). This

would result in a series of "glitches" in the lightcurves, each representing injection of energy from i-th shell into the blastwave.

Besides the energy, we also derive the (lower limit) Lorentz factor γ_i of each shell. This parameter is important, especially for early shells, since it determines the deceleration time of a certain shell. This is particularly relevant for the first shell. The Lorentz factors of later shells are also relevant for two reasons. First, they can be used to calculate the effective Lorentz factor of a "merged" shell after adding energy to an existing shell. This is needed to calculate the deceleration time of the blastwave solutions. Second, since the observed time for a late energy injection is defined by Maxham & Zhang (2009)[114]

$$t_{\oplus,col} = t_{ej} + \frac{(t_{col} - t_{ej})}{2\gamma^2} \, , \tag{9.3}$$

where t_{ej} and t_{col} are the times of ejection and collision measured in the rest frame of the central engine. The effect of γ becomes progressively less important, since at large t_{ej}'s, the second term in Eqn.(9.3) becomes negligible so that the observed collision time is essentially defined by the ejection time. In any case, we derive the constraints on γ for each time bin using the pair opacity argument as described below.

To derive a constraint on the Lorentz factor, we have collected the spectral parameters and the observed maximum photon energy $E_{\oplus,\rm max,i}$ for each time bin. One can then derive the maximum photon energy in the cosmological local frame, i.e. $E_{\rm max,i} = E_{\oplus,\rm max,i}(1+z)$. Requiring the pair production optical depth to be less than unity for $E = E_{\rm max,i}$, we can write a general constraint in the parameter space of R and γ (where R is the distance of the emission region from the central

engine[69][200]), i.e.

$$R(\gamma) > \sqrt{\frac{C(\beta)\sigma_T d_z^2}{-1-\beta f_0}\left(\frac{E_{\rm max}}{511{\rm keV}^2}\right)^{-1-\beta}\left(\frac{\gamma}{1+z}\right)^{2+2\beta}}, \tag{9.4}$$

where σ_T is the Thompson cross section, β represents the slope of the power law component for GRBs 090902B and 090510 and the Band function high energy spectral parameter for GRBs 080916C and 090926A, and f_0 (in units of $\rm ergs \cdot cm^{-2} \cdot s^{-1}$) can be written as $f_0 = A \cdot \Delta T \left[\frac{E_p(\alpha-\beta)}{2+\alpha}\right]^{\alpha-\beta} \exp(\beta-\alpha)(100 \quad {\rm keV})^{-\alpha}$ for the Band function model, and $f_0 = K \cdot \Delta T (100 \quad {\rm keV})^{-\beta}$ for the simple power law model, where A and K are normalization factors (both normalized to 100 keV). The approximation $\rm C(\beta) \simeq (7/6)(-\beta)^{5/3}/(1-\beta)$ [172] is adopted to perform the calculation. In order to further constrain γ, one needs to make an assumption about R. Without other independent constraints, we apply the conventional assumption of internal shocks, so that $R(\gamma) = \gamma^2 c\frac{\delta t}{1+z}$, where δt is the observed minimum variability time scale. Combining Eq.(9.4), the lower limit for γ is derived for each time bin of each burst (see also [109][1][2]). In our calculation, we generally adopt γ_i as the derived lower limit. This is because the derived Lorentz factors of other GRBs using the afterglow deceleration constraint[108] or photosphere constraint[139] are all below or consistent with these lower limits derived from the opacity constraints[1][2][3][4].

Model Results

Feeding this data into our shell model code, letting each shell be ejected with energy $E_{k,i}$ and Lorentz factor γ_i at time equal to that of the beginning of the bin time, we can calculate the early blastwave evolution and LAT band (integrated over > 100 MeV) lightcurve for the four GRBs.

To match the observed steep decay (with slope ~ -1.5), we adopt a radiative fireball solution or an adiabatic fireball solution with steep electron energy index. Even though each solution (for a fixed kinetic energy) has a steep decay slope, the overall lightcurve shows a shallower decay due to piling up of successive shells ejected later, with glitches introduced by jumping among the solutions. As an example, the radiative model lightcurve of GRB 080916C as compared with observation is presented in Fig.1. The top panel shows the long term evolution, while the bottom panel is the zoomed-in early afterglow lightcurve. The dotted lines denote the blastwave solutions with progressively increasing total energy. The lowest one corresponds to the first time bin, the second lowest corresponds to adding the energy of the second time bin, etc.

Since the lightcurve is chopped into discrete time bins, the blastwave energy is added in discrete steps. This introduces some artificial glitches in the lightcurve. Such an approximation is more realistic for GRBs with distinct emission episodes. For GRB 080916C, the lightcurve is more appropriately approximated as a continuous wind with variable luminosity. The artificial glitches should appear to be more smeared. For this reason, we have smoothed the glitches to make more natural transitions between solutions. The model afterglow parameters (the fraction of electron energy ϵ_e, the fraction of magnetic energy ϵ_B, and the number density n) are presented in Table 1. These are in general consistent with the parameter constraints derived by Kumar & Barniol Duran (2009, 2010[88][89]).

In general, the model lightcurve of GRB 080916C cannot fit the early LAT data. Making the model suitable to fit the late-time steep decay, the early model lightcurve level is too low to account for the observed data. Alternatively, one can make the early model lightcurve match the observed flux level. Then inevitably the late time afterglow level exceeds the observed level significantly due to the continu-

ous energy injection. We believe that if the LAT band emission after T_{90} originates from the external shock, then the LAT emission during the prompt emission phase *cannot* be solely interpreted by the external shock model. The external shock contribution is relatively small, especially during early epochs when energy in the blastwave is small. As a result, the GeV emission during the prompt phase must be of an internal origin. This is consistent with the fact that the entire GBM/LAT emission during the prompt phase can be well fit by a single Band-function spectral model in all the time bins[1][192].

We have also modeled GRBs 090510, 090902B and 090926A. The model parameters (for both radiative and adiabatic solutions) are listed in Table 1, and the results for radiative solution are shown in Fig.43. In all cases, the slope and flux level of the data are matched in the latter part of the curve only. During the prompt emission phase, the data points rise above the flux prediction of the external shock model, suggesting that GeV emission is a superposition of external and internal components during the prompt emission phase ($T < T_{90}$). This conclusion is valid for both the adiabatic and radiative solutions. The difference between the two is that the adiabatic model invokes a shallower p but a larger ξ (and hence a larger energy budget) to fit the same data.

Conclusion and Discussion

Using the first-hand Fermi data, we have tracked the energy output from the central engine and modeled the early blastwave evolution of four bright LAT GRBs. The predicted > 100 MeV lightcurve is found unable to account for the observed LAT emission during the prompt emission phase. The main reason is that during the phase when the central engine is still active, the forward shock is continuously refreshed by late energy injection, so that the afterglow decays much slower than

Table 4 Parameters used for the four sample bursts. [1][176] [2][148] [3][32] [4][111]

080916C	adiabatic	radiative
p	2.5	2.1
ξ	5	10
ϵ_e	0.3	0.3
ϵ_B	0.01	0.01
n	1	1
z	4.35[1]	

090510	adiabatic	radiative
p	2.4	2.1
ξ	2	3
ϵ_e	0.5	0.5
ϵ_B	0.01	0.01
n	0.1	0.1
z	0.903[2]	

090902B	adiabatic	radiative
p	2.4	2.1
ξ	1	1
ϵ_e	0.2	0.15
ϵ_B	0.001	0.01
n	0.001	0.01
z	1.822[3]	

090926A	adiabatic	radiative
p	2.4	2.2
ξ	3	3
ϵ_e	0.3	0.3
ϵ_B	0.01	0.01
n	0.1	0.1
z	2.1062[4]	

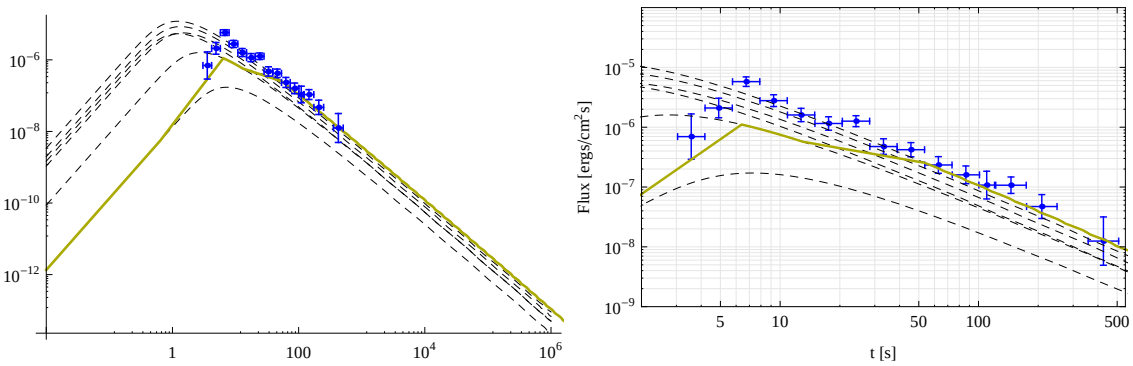

Figure 42 The predicted external shock > 100 MeV lightcurve of GRB 080916C for a radiative blastwave solution (yellow line) as compared with the data (blue points). Successive lightcurves that correspond to different total blastwave kinetic energy are shown as dashed lines. The top panel shows the global lightcurve, while the bottom panel shows a zoom view where the flux deficit at early times can be clearly seen.

the case predicted by an instantaneously ejected constant energy fireball. This suggests that at least during the prompt emission phase, the LAT band emission is not of external forward shock origin. This is in contrast to the suggestion of Ghisellini et al. (2009)[61] and Kumar & Barniol Duran (2009)[88], who did not consider the energy accumulation during the prompt emission phase and interpreted the entire GeV emission as of the external shock origin of an instantaneously ejected fireball. Feng & Dai (2010)[45] considered this energy accumulation process, but made the assumption that the central engine ejects shells with progressively increasing Lorentz factors. This model can reproduce a steep rising lightcurve before the afterglow peak time, but would still have difficulty accounting for the observed simple power law decay after the peak, since the energy injection process discussed in this paper still plays an important role before the end of GBM-band prompt emission.

Our conclusion is based on the assumption that GRB radiative efficiency is es-

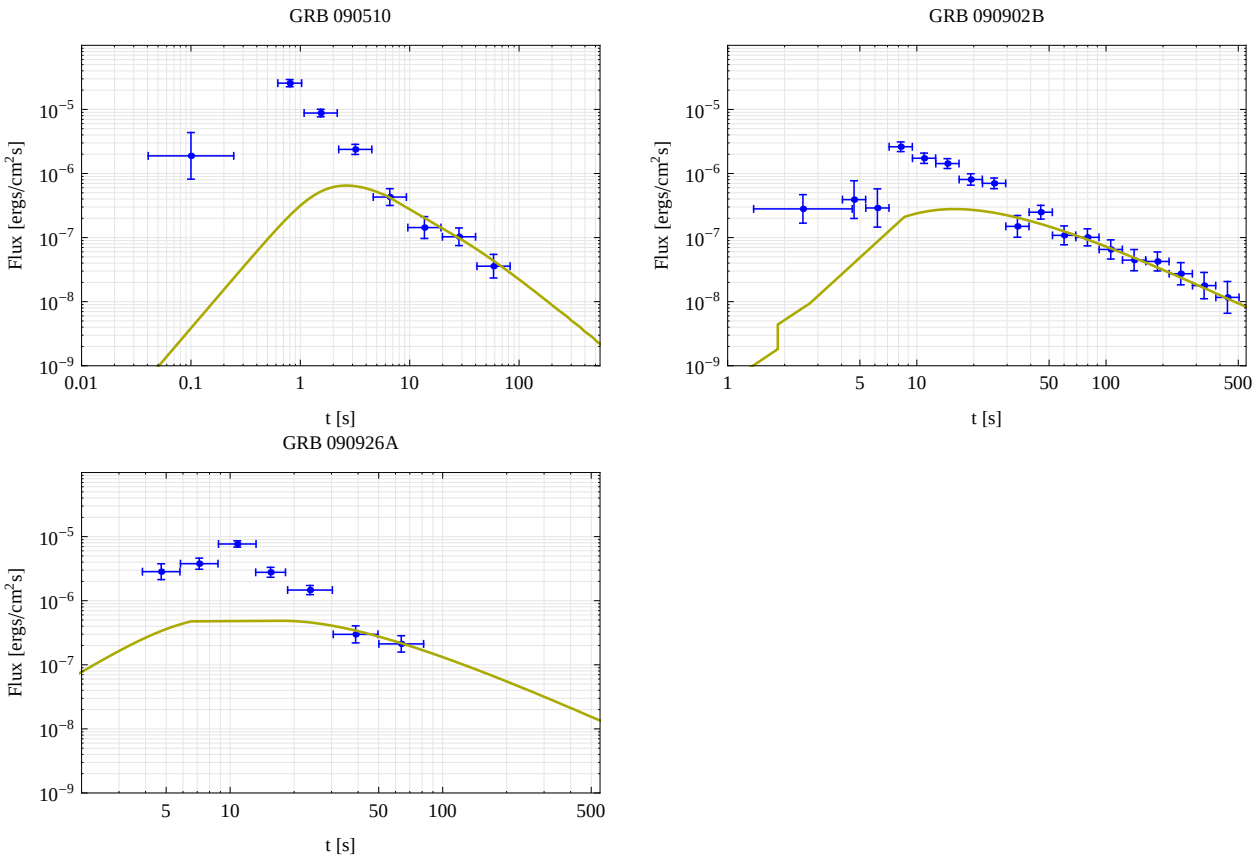

Figure 43 Model predictions of > 100 MeV lightcurve (for a radiative blastwave solution) vs. observed data for GRBs 090510, 090902B, and 090926A. The conventions are similar to Fig.1, but without successive solutions specifically plotted.

sentially a constant throughout the burst. In order to interpret the entire afterglow as due to the external forward shock origin, one needs to "artificially" assume that the GRB efficiency increases with time, so that the late time central engine activity, even though producing bright γ-ray emission, adds little kinetic energy into the blastwave. Another possibility would be to assume that the initial energy of the blastwave does not produce MeV gamma-rays, and this dark component contributes to the majority of the afterglow energy. We believe that both such assumptions are unnatural and contrived.

Our conclusion is consistent with some independent arguments. From data analysis, Zhang et al. (2011)[192] showed that during the prompt emission phase the GeV emission has rapid variability and traces the MeV emission well[2]. For GRB 080916C, the entire GBM/LAT emission can be modeled by a single Band function component in all the time bins (see also [1]). For GRB 090902B, even though GeV emission belongs to a distinct spectral component, its flux seems to track the flux of the MeV component nicely, suggesting a connection in the physical origin (see Pe'er et al. 2011 for modeling). A more definite argument in favor of an internal origin of GeV emission in GRB 080916C is that the GeV lightcurve peak coincides the second peak in the GBM lightcurve, suggesting that GeV emission is the spectral extension of MeV emission to higher energies[192]. Also individual case studies of GRB 090902B [139][110]and GRB 090510[70] all suggest that the external shock model cannot interpret the prompt GeV data. In general, our modeling suggests that it is possible to use the external shock model to interpret GeV emission after the prompt emission phase, but not during the prompt emission phase (see also [89]).

[2]Gao et al. (2009)[54] also used the variability argument to argue against the external shock origin of the prompt GeV emission.

Since the observed GeV lightcurve is consistent with a simple power law decay after the peak time, one requires a coincidence in the current picture so that the external shock emission lightcurve appears as a natural extension of the early GeV lightcurve that is of an internal origin. We note, however, that the external shock energy parameter (ξ) and other parameters (e.g. ϵ_e, ϵ_B) adopted in our calculations are all within the reasonable range, suggesting that the calculated external shock GeV emission can be indeed at the expected level. Parameter space explorations suggest that there is a good range of parameters that can reasonably reproduce the late lightcurve, without needing to fine-tune the parameters. Furthermore, according to our data analysis, the derived GeV lightcurves are not strict power laws. Some possible features (e.g. wiggles in GRB 080916C and GRB 090902B and a flattening feature in GRB 090510 and GRB 090926A) that may be related to the merging of the external shock component are observed. The coincidence problem is therefore not as severe as it appears.

On the other hand, the model that interprets the prompt GeV emission as due to an external shock origin also demands a coincidence in the spectral domain, so that the internal and the external shock components would conspire to mimic a single Band function in GRB 080916C[88]. Since the Band function perseveres in the time-resolved spectra of several time bins[1][192], that model demands coincidence in all the time bins. This coincidence problem may be more demanding than the model discussed in this paper.

Our conclusion also has implications for understanding GRB prompt emission physics, in particular, the composition of the GRB outflow. The internal origin of the GeV emission in GRB 080916C makes it essentially impossible to interpret the entire Band spectrum with the photosphere model (e.g. [11][96]). The lack of photosphere emission then demands a Poynting-flux-dominated outflow at least for

this burst[200][44]. This argument, along with other evidence uncovered in other GRBs (e.g. [131]), calls for new models of GRB prompt emission in the Poynting flux dominated regime (e.g. [201]).

REFERENCES

[1] Abdo, A. A. et al. 2009a, Science, 323, 1688

[2] Abdo, A. A., et al. 2009b, ApJ, 706, L138

[3] Abdo, A. A., et al. 2010, ApJ, submitted

[4] Ackermann, M., et al. 2010, ApJ, 716, 1178

[5] Amati, L. et al. 2002, A&A, 390, 81

[6] Atwood, L., et al. 2002, A & A, 390, 81

[7] Atwood, L., et al. 2009, ApJ, 697, 1071

[8] Band, D. et al. 1993, ApJ, 413, 281

[9] Band, D., L. & Preece, R., 2005, ApJ, 627, 319

[10] Barthelmy, S.D., et al. 2005, Nature, 438, 994

[11] Beloborodov, A.M. 2011, ApJ, submitted (arXiv:1011.6005)

[12] Blandford, R. & McKee, C. 1976, Phys. Fluids, 19, 1130

[13] Berger, E. et al. 2005, Nature 438, 988

[14] Berger. E. 2009, ApJ, 690, 231

[15] Berger. E. 2010, ApJ, 722, 1946

[16] Bhat, P.N. et al. 1992, Nature, 359, 217

[17] Bissaldi, E. 2009, GCN 9933

[18] Bloom, J. et al. 1998, IAUC, 6899

[19] Bloom, J. et al. 2001, ApJ, 554, 678

[20] Bonnell, J.T. & Klebesadel R. 1996, AIP Conf. Proc. 384, 977

[21] Borgonovo, L. et al. 2007, A & A 465, 3

[22] Briggs et al. 1999, ApJ, 524, 82

[23] Burrows, D.N., et al. 2005a, Space Sci. Rev., 120, 165

[24] Burrows, D.N., et al. 2005b, Science, 309, 1833

[25] Burrows, D.N., et al. 2005c, astro-ph/0511039v2

[26] Cannizzo, J.K., Gehrels, N. & Vishniac, E.T. 2004, ApJ, 601, 380

[27] Cecchi, C. & the GLAST LAT Collaboration, 2008,JPhCS, 120, 062017

[28] Chiang, J. & Dermer, C.D. 1999, ApJ, 512, 699

[29] Chincarini, G., et al. 2007, ApJ, 671, 1903

[30] Colgate, S.A. 1968, Can J. Phys., 46, S476

[31] Costa, E. et al. 1997, Nature, 387, 783

[32] Cucchiara, A., Fox, D. B., Tanvir, N., & Berger, E. 2009, GCN, 9873

[33] Cucchiara, A., et al. 2011, ApJ, submitted

[34] Cusumano, G., et al. 2006, Nature, 440, 164

[35] Dai, Z.G. & Lu, T. 1998, Phys.Rev.Lett., 81, 4301

[36] Dai, Z.G., Wang, X.Y., Wu, X.F. & Zhang, B. 2006, Science, 311, 1127

[37] De Pasquale, M. et al. 2009, MNRAS, 392, 153

[38] Evans, P. et al. 2007, A&A, 469, 379

[39] Evans, P. et al. 2009, MNRAS, 397, 1177

[40] Evans, W. et al. 1981, Ap&SS, 75, 35

[41] Falcone, A.D., et al. 2006, ApJ, 641, 1010

[42] Falcone, A.D., et al. 2007, ApJ, 671, 1921

[43] Fan, Y.Z. & Wei, D.M. 2005, MNRAS, 354, L42

[44] Fan, Y.-Z. 2010, MNRAS, 403, 483

[45] Feng, S.Y. & Dai, Z.G. 2010, ApJ, submitted (arXiv:1011.3103)

[46] Fenimore, E.E., Madras, C.D.& Nayakshin, S. 1996, ApJ, 473, 998

[47] Fishman, G.J. et al. 1992, NASCP 3137, 26

[48] Fishman, APOD, June 28, 2000

[49] Frail, D. et al. 1997, Nature, 289, 261

[50] Frontera, F. et al. 1997, ICRC 3, 25

[51] Fruchter, A. S., et al. 2006, Nature, 441, 463

[52] Gal-Yam, A. et al. 2006 Nature, 444, 1053

[53] Gao,H., Zhang, B-B. & Zhang, B. 2011, ApJ submitted, (arXiv:1103.0074)

[54] Gao, W.-H., Mao, J., Xu, D., Fan, Y.-Z. 2009, ApJ, 706, L33

[55] Gehels, N., Ramirez-Ruiz, E. & Fox, D.B. 2009, ARA&A, 47, 567

[56] Gehrels, N., et al. 2004, ApJ, 611, 1005

[57] Gehrels, N. et al. 2005, Nature, 437, 851

[58] Gehels, N. et al. 2006, Nature, 444, 1044

[59] Genet, F., Daigne, F. & Mochkovitch, R. 2007, MNRAS, 381, 732

[60] Ghirlanda, G. 2010, Proceedings IAU Symposium, 275, 2010

[61] Ghisellini, G., Ghirlanda, G., Nava, L. & Celotti, A. 2010, MNRAS,403, 926

[62] Ghisellini, G., Ghirlanda, G., Nava, L. & Firmani, C. 2007, ApJ, 658, L75

[63] Granot, J. & Kumar, P. 2006, MNRAS, 366, L13

[64] Granot, J. et al., 2002, ApJ, 570, L61

[65] Greiner, J. et al. 2003, GCNC 2020

[66] Greiner, J., et al. 2009, ApJ, 693, 1610

[67] Gronwall, C. & Vetere, L. 2009, GCN 9938

[68] Guetta, G., Spada, M. & Waxman, E. 2001, ApJ, 557, 399

[69] Gupta, N., & Zhang, B. 2007, MNRAS, 380, 78

[70] He, H.-N. et al. 2011, ApJ, submitted (arXiv:1009.1432)

[71] Huang, Y.F., Gou, L.J., Dai, Z.G. & Lu, T. 2000, ApJ, 543, 90

[72] Hurkett, C., et al. 2005, GCNC 3381

[73] Ioka, K., Kobayashi, S. & Zhang, B. 2005, ApJ, 631, 429

[74] Kawai, N. et al. 1999, A&AS, 138, 563

[75] Kawai, N. et al. 2006, Nature, 440, 184

[76] Kelly, P., Kirshner, R. & Pahre, M. 2007, ApJ, 687, 1201

[77] King, A., et al. 2005, ApJ, 630, L113

[78] Klebesadel, R., Evans, W. & Laros, J. 1981, Ap&SS, 75, 5

[79] Klebesadel, R., Strong, I. & Olson, R., 1973 ApJ 182, L85

[80] Knight, F., Matteson, J. & Peterson, L., 1981 Ap&SS 75, 21

[81] Kobayashi, S., Piran, T. & Sari, R. 1997, ApJ, 490, 92

[82] Kobayashi, S., Piran, T. & Sari, R. 1999, ApJ, 513, 669

[83] Kocevski, D., Butler, N. & Bloom, J. 2007, ApJ, 667, 1024

[84] Kouvelioutou, C. et al., 1993, ApJ, 413, L101

[85] Krimm, H.A. et al. 2007, ApJ, 665, 554

[86] Krimm, H.A. et al. 2009, ApJ, 704, 1405

[87] Kumar, P. 1999, ApJ, 523, L113

[88] Kumar, P. & Barniol Duran, R. 2009, MNRAS, 400, L75

[89] Kumar, P. & Barniol Duran, R. 2010, MNRAS, 409, 226

[90] Kumar, P. & Granot, J. 2003, ApJ, 591, 1075

[91] Kumar, P. & Panaitescu, A. 2000, ApJ, 541, L51

[92] Kumar, P. & Piran, T. 2000a, ApJ, 532, 286

[93] Kumar, P. & Piran, T. 2000b, ApJ, 535, 152

[94] Kumar, P. et al. 2008, MNRAS, 388, 1729

[95] Krühler, T. et al. 2009, (arXiv:0903.1184v1)

[96] Lazzati, D. & Begelman, M.C. 2010, ApJ, 725, 1137

[97] Lazzati, D. & Perna, R. 2007 MNRAS 375, L46

[98] Lazzati, D., Perna, R. & Begelman, M.C. 2008 MNRAS 388, L15

[99] Lee, W. H., Ramirez-Ruiz, E., Lopez-Camara, D. 2009, ApJ, 699, L93

[100] Leibler, C.N & Berger, E., 2010, ApJ, 725, 1202

[101] Li, Z. & Waxman, E. 2008, ApJ, 674, L65

[102] Liang, E.W., Dai, Z.G., & Wu, X.F. 2004, ApJ, 606, L29

[103] Liang, E.W., Lv, H.J., Hou, S.J., Zhang, B.B. & Zhang, B. 2009, ApJ, submitted (arXiv:0902.3504)

[104] Liang, E.W., Racusin, J.L., Zhang, B., Zhang, B.B. & Burrows, D.N. 2008, ApJ, 675, 528

[105] Liang, E.W. & Zhang, B. 2005, ApJ, 633, 611

[106] Liang, E.W., Zhang, B.B. & Zhang, B. 2007, ApJ, 670, 565

[107] Liang, E.W. et al. 2006, ApJ, 646, 351

[108] Liang, E.W. et al. 2010, ApJ, 725, 2209

[109] Lithwick, Y. & Sari, R. 2001 ApJ, 555, 540

[110] Liu, R.-Y. & Wang, X.-Y. 2011, ApJ, submitted (arXiv:1009.1289)

[111] Malesani, D., et al. 2009, GCN, 9942, 1

[112] Mandrou, J.P. et al., 1994, ApJS, 92, 343

[113] Margutti, R. et al. 2010, 406, 2149

[114] Maxham, A., & Zhang, B. 2009, ApJ, 707, 1623

[115] Maxham, A., Zhang, B.-B. & Zhang, B. 2011, MNRAS, accepted

[116] Mazets, E.P. & Golenetskii, S.V. 1981, Ap&SS, 75, 47

[117] Mazzali, P. et al., 2006, Nature, 442, 1018

[118] Melandri, A. et al. 2006, A&A, 451, 27

[119] Meegan, C.A. et al., 1992, Nature, 355, 143

[120] Meegan, C., et al. 2009, ApJ, 702, 791

[121] Mészáros, P., Laguna, P. & Rees, M.J. 1993, ApJ, 415, 181

[122] Mészáros, P. 2010, *The High Energy Universe*, Cambridge University Press

[123] Mészáros, P. 2006, Rept.Prog.Phys., 69, 2259

[124] Mészáros, P. & Rees, M. J. 1993, ApJ, 405, 278

[125] Mészáros, P. & Rees, M. J. 1997, ApJ, 476, 232

[126] Metzger, M., et al. 1997, Nature, 387,878

[127] Mirabal, N., et al. 2006, ApJ, 643, 99

[128] Murakami, T. et al. 1989, PASJ, 41, 405

[129] Nakar, E. & Piran, T., 2005, MNRAS, 360, L73

[130] Nakar, E., Piran, T. & Granot, J. 2002, ApJ, 579, 699

[131] Narayan, R. & Kumar, P. 2009, MNRAS, 394, L117

[132] Nousek, J.A., et al. 2006, ApJ, 642, 389

[133] Oates, S.R. et al. 2009, MNRAS, 395, 490

[134] O'Brien, P.T., et al. 2006, ApJ, 645, 1315

[135] Panaitescu, A. 2008, MNRAS 383, 1143

[136] Panaitescu, A. & Kumar, P. 2002, ApJ, 571, 779

[137] Panaitescu, A., Spada, M. & Mészáros, P. 1999, ApJ 522, L105

[138] Panaitescu, A. et al. 2006, MNRAS 369, 2059

[139] Pe'er, A. et al. 2011, ApJ, submitted (arXiv:1007.2228)

[140] Perna, R., Armitage, P., & Zhang, B. 2006, ApJ, 636, L29

[141] Piran, T. 1997 in *Unsolved Problems in Astrophysics*, Bahcall, J. & Ostriker, J., Princeton University Press

[142] Piran, T. 2004, Rev.Mod.Phys., 636, L29

[143] Preece, R.D., Goldstein, A. & Briggs, M. S. 2010, HEAD, 11, 0203

[144] Proga, D. & Zhang, B. 2006, MNRAS, 370, L61

[145] Qin, Y.-P., et al. 2000, PASJ, 52, 759

[146] Racusin, J. et al. 2008, Nature, 455, 183

[147] Ramana Murthy, P.V. & Wolfendale, A.W., 1986, *Gamma-Ray Astronomy*, Cambridge University Press

[148] Rau, A., McBreen, S., & Kruehler, T. 2009, GRB Coordinates Network, 9353, 1

[149] Rees, M.J. & Mészáros, P. 1992, MNRAS, 258, 41P

[150] Rees, M.J. & Mészáros, P. 1994, ApJ, 430, L93

[151] Rees, M. J. & Mészáros, P. 1998, ApJ, 496, L1

[152] Rhoads, J. 1997, ApJ 487, L1

[153] Rhoads, J. 1999. ApJ 525, 737

[154] Romano, P., et al. 2006, A&A, 450, 59

[155] Roming, P.W.A., et al. 2005, SSRv, 120, 95

[156] Roming, P.W.A., et al. 2009, ApJ, 630, 163

[157] Ruderman, M. 1975, *Ann. N.Y. Acad. Sci.* 262, 164

[158] Salvaterra, R. et al. 2009, Nature, 461, 1258

[159] Sari, R. & Piran, T. 1995, ApJ, 455, L143

[160] Sari, R. & Piran, T. 1999, ApJ, 517, L109

[161] Sari, R., Piran, T. & Narayan, R. 1998 ApJ, 497, L17

[162] Schaefer, B.E. 2007, ApJ, 660, 16

[163] Schmidt, M. 1999, ApJ, 523, L117

[164] Schmidt, W. 1978, Nature, 271, 525

[165] Sedov, L. 1969, Similarity and Dimensional Methods in Mechanics, Academic, New York, Chap. IV

[166] Shao, L. & Dai, Z.G. 2007 ApJ 660, 1319

[167] Soderberg, A.M. 2010, Nature, 463, 513

[168] Spada, M., Panaitescu, A. & Mészáros, P. 2000 ApJ 537, 824

[169] Stanek, K. et al. ApJ, 591, L17

[170] Stratta, G. et al. 2009, A&A, 503, 783

[171] Strong I. & Klebesadel R. 1976, *Sci. Am.* 235, 66

[172] Svensson, R. 1987, MNRAS, 227, 403

[173] Swenson, C. & Maxham, A. 2010, ApJ, 718, 14

[174] Teegarden, B.J. & Sturner, S.J. 1999, HEAD, 31,717

[175] Uhm, Z.L. & Beloborodov, A.M. 2007, ApJ 665, L93

[176] van der Horst, A. & Goldstein, A. 2008 GCNC, 8278, 1

[177] van Paradijs, J. et al. 1997, Nature, 286, 686

[178] Virgili, F. et al. 2011, ApJ, 727, 109

[179] Wang, X. Y. et al. 2010, ApJ, 712, 1232

[180] Waxman, E. 1997 ApJ 498, L33

[181] Wei, D.M. 2007 MNRAS 374, 525

[182] Wijers, R. A. M. J. & Galama, T. J. 1999, ApJ, 523, 177

[183] Wijers, R. et al. 1997, MNRAS, 288, L51

[184] Woosley, S.E., Langer, N., & Weaver, T.A. 1993, ApJ, 411, 823

[185] Wu, X.F. et al. 2005, astro-ph/0512555

[186] Yamazaki, R. 2009, ApJ, 690, L118

[187] Yonetoku, D. et al. 2004, ApJ, 609, 935

[188] Yost, S. A., Harrison, F. A., Sari, R., Frail, D. 2003, ApJ, 597, 459

[189] Yu, Y.W. & Dai, Z.G. 2009, ApJ, 692, 133

[190] Yuan, F. et al. 2010, ApJ, 711, 870

[191] Zhang, B.B., Liang, E.-W. & Zhang, B. 2007, ApJ, 666, 1002

[192] Zhang, B.B. et al. 2011, ApJ, 730, 141

[193] Zhang, B. 2007, Chinese J. Astron. Astrophys., 7, 1

[194] Zhang, B., Fan, Y.Z. & Dyks, J. 2006, ApJ, 642, 354

[195] Zhang, W. & MacFadyen, A. 2009, ApJ, 698, 1261

[196] Zhang & Mészáros 2001, ApJ, 552, L35

[197] Zhang, B. & Mészáros, P. 2002a, ApJ, 566, 712

[198] Zhang & Mészáros 2002b, ApJ, 581, 1236

[199] Zhang, B. & Mészáros, P. 2004, IJMPA, 19, 2385

[200] Zhang, B. & Pe'er, A. 2009, ApJ, 700, L65

[201] Zhang, B. & Yan, H. 2009, ApJ, 726, 90

[202] Zhang, B. et al. 2007a, ApJ, 655, 989

[203] Zhang, B. et al. 2007b, ApJ, 655, L25

[204] Zhang, B. et al. 2009, ApJ, 703, 1696

[205] Zou, Y-C. & Piran, T. 2009, MNRAS, 402, 1854

VITA

Graduate College
University of Nevada, Las Vegas

Amanda Maxham

Degrees:

Bachelors of Science, Physics, Astronomy-Physics 2001
University of Wisconsin, Madison

Masters of Science, Astronomy 2003
University of Illinois, Urbana-Champaign

Publications:

Maxham, Amanda; Zhang, B.B.; Zhang, B.. Is LAT GeV emission of External Shock Origin? 2011, MNRAS, accepted.

Zhang, B.B.; Zhang, B.; Liang, E.W.; Fan, Y.Z.; Wu, X.F.; Pe'er, A.; **Maxham, Amanda**; Gao, H.; Dong, Y.M. A Comprehensive Analysis of Fermi Gamma-Ray Burst Data. I. Spectral Components and Their Possible Physical Origins of LAT/GBM GRBs. 2011, ApJ, 730, 141.

Swenson, C.A.; **Maxham, Amanda**; Roming, P.W.A.; Schady, P.; Vetere, L.; Zhang, B.B.; Zhang, B.; Holland, S.T.; Kennea, J.A.; Kuin, N.P.M.; Oates, S.R.; Page, K.L.; De Pasquale, M. GRB 090926A and Bright Late-time Fermi Large Area Telescope Gamma-ray Burst Afterglows. 2010 ApJ, 718, L14.

Maxham, Amanda; Zhang, B. Modeling Gamma-Ray Burst X-Ray Flares Within the Internal Shock Model. 2009, ApJ, 707, 1623

Maxham, A.; Zhang, B.; Kobayashi, S. Modeling Gamma-Ray Burst Prompt Emission and X-Ray Flares within the Internal Shock Model. 2007, Proc.GRBs2007

Chu, Y.H.; Dodd, C.; Gillani, K.; Gruendl, R.; Guerrero, M.; **Maxham, A.**; O'Dwyer, I.; Webbink, R. Hard X-ray Emission from White Dwarfs. 2002 BAAS, 34, 1301

Doering, R.; Meixner, M.; Fong, D.; Zalucha, A.; **Maxham, A.**; Speck, A. Near-IR and BIMA CO Observations of the Red Rectangle. 2002, BAAS 34, 1252

Dissertation Title:
Modeling Gamma-Ray Bursts

Dissertation Committee:

Committee Chairperson: Dr. Bing Zhang, Ph.D.
Committee Memeber: Dr. Stephen Lepp, Ph.D.
Committee Memeber: Dr. Tao Pang, Ph.D.
Committee Memeber: Dr. Daniel Proga, Ph.D.

Graduate Faculty Representative: Dr. Matthew Lachniet, Ph.D.